# Design of Medical Devices Involving Multi-disciplinary Processes and Based on Fundamental Physical Principles

A DISSERTATION
SUBMITTED TO THE FACULTY OF
UNIVERSITY OF MINNESOTA
BY

Kevin Robert Krautbauer

IN PARTIAL FULFILLMENT OF THE REQUIREMENTS
FOR THE DEGREE OF
DOCTOR OF PHILOSOPHY

Ephraim M. Sparrow

April 2016

**Acknowledgements**

This dissertation could never have come to fruition without the tireless support of my advisor, Dr. Ephraim Sparrow, and his associate Dr. John Gorman. They have my deepest thanks. I would also like to thank two of my fellow graduate students, Dan Bryant and Harrison Coons, for their assistance with running ANSYS simulations.

## Dedication

This thesis is dedicated to my loving wife who has supported me throughout this entire process.

## Abstract

This dissertation focuses on the optimal design of medical devices through the use of numerical simulation and the utilization of first principles of the participating phenomena. Through three broadly ranging case studies, the dissertation explores a wide variety of physical phenomena found within medical devices and in other applications. Pressure drop and sound generation are the primary focii of the leading case study which constitutes the first-ever analysis of the fluid mechanics of a therapeutic device for the treatment of cystic fibrosis. The treatment utilizes a time varying pressure that acts on the abdomen of the patient in order to break up masses of mucus. The second study is the first known effort to design peristaltic pumps using the principles of fluid-structure interaction. The time-dependent mechanics of peristaltic pumping were utilized to determine the deformations and pressures in the flexible-walled plastic tubing. The change of volume of the tubing serves to propel a liquid contained within the tube. Finally, the third study investigates the fluid mechanics and heat transfer mechanisms found in an enhanced-surface fluid warming device.

The key analysis and design tools used throughout the aforementioned case studies of this dissertation are physical model formulation adapted to computational fluid dynamics (CFD), the theory of turbulence-based sound generation, Ogden's hyperelastic model of polymeric materials, and the theory of heat transfer. The fluid flow phenomena dealt with in this work include three-dimensional, unsteady, laminar and turbulent flows. Heat transfer concepts utilized include conduction within both fluids and solids, advection within interacting parallel flow regions, and the theory of heat transfer enhancement.

Each chapter contains multiple results pertaining to the device in question. These results serve to expand the reader's knowledge of the underlying physical processes which control the function and effectiveness of the medical device.

## Table of Contents

## List of Tables

## List of Figures

# Chapter One

## INTRODUCTION

The research described in this thesis was motivated by the first-principles design of biomedical devices. Although there is a rich literature devoted to the effects of device-delivered therapies, there is a paucity of papers that deal with the devices themselves. This situation may be attributed to two causes: (a) protection of intellectual property and (b) limitation of the design process to intuition-based knowledge. Design approaches based of the first-principles laws of nature are rarely encountered.

In this thesis, three unique biomedical devices will be considered. These devices bridge over four disciplines: fluid flow, heat transfer, structures, and sound generation. The multi-disciplinary nature of the present research is in tune with the realities of current-day engineering practice. This reality is at odds with the current theme of university-level education, where specialization is being fostered. As a consequence, most important engineering breakthroughs are made by teams of persons of different disciplinary backgrounds.

A separate literature survey will be performed for each of the three devices. To maximize the relevance of the outcomes of these searches, each will be embedded in the chapter where the particular device is treated.

The thesis is structured into five chapters: the present one, Chapters Two, Three, and Four, each devoted to a specific device, and Chapter Five which is a retrospective overview of the accomplishments of the entire work.

Chapter Two was motivated by the need for therapeutic devices to treat the life-confining impacts of cystic fibrosis. Cystic fibrosis is a genetic condition in which the lungs and

digestive system become clogged with thick sticky mucus. Common outcomes are persistent lung infections and limitations on the ability to breathe. The cells that produce mucus, sweat, and digestive juices are highly affected. In persons with cystic fibrosis, a defective gene causes a thick, buildup of mucus in the lungs, pancreas and other organs. In the lungs, the mucus clogs the airways and traps bacteria leading to infections, extensive lung damage and eventually, respiratory failure. In the pancreas, the mucus prevents the release of digestive enzymes that allow the body to break down food and absorb vital nutrients.

The therapy of interest is the use of physical agitation to loosen mucus and propel it toward larger vessels and passages from which it can be more readily extracted, for example, by coughing. Although clearance of the airways is a primary means of relief for cystic fibrosis, it is also effective in less profound dysfunctions such as asthma. The total therapeutic device consists of a unique source of periodically pulsed air pressure, and an inflatable vest which girdles the abdomen of the patient and receives and discharges the pulsating airflow. The source should be able to be tuned both with respect to the amplitude and frequency of the pressure pulsations.

The airflow is multidimensional, unsteady, and turbulent. Results provided by the fluid mechanic study include the rates of fluid flow between the pressure source and the inflatable vest, the rates of air supplied to and extracted from the device, the fluid velocity magnitudes and directions that result from the geometry of the source, and the magnitude of the turbulence generated by the fluid motion and the rotating component of the pressure source. Inasmuch as cystic fibrosis therapeuty is administered very frequently, patient comfort is of great important.  In that regard, it is noteworthy that high pressure, high velocity, and high turbulence air can give rise to elevated sound pressures. This realization motivated the determination of sound pressure levels.

Chapter Three is focused on the design of wall-driven peristaltic pumps based on first principles with minimal simplifying assumptions. In general, a peristaltic pump consists of

a flexible-walled tube and a structural member which periodically squeezes and releases the tube wall. The peristaltic principle is typically used therapeutically to pump clean/sterile fluids. It provides the highly significant advantage of not permitting cross contamination of the pumped medium by avoiding contact between the pump components and the fluid. Specific biomedical therapeutic applications include pumping IV fluids through an infusion device and circulating blood by means of heart-lung machines during a bypass surgery. Within the human body, peristaltic pumping plays a major role in the renal and digestive systems.

The specific design modality used here involves structural analysis of a hyperelastic tube-wall medium. Primary attention must be given to the nature of the structural properties of the participating medium. Here, hyperelastic properties were deemed appropriate for the compressible tubular material that is commonly used for mechanically driven peristaltic pumping. The theory of hyperelastic stress and strain was used to underpin the analysis.

The applied force needed to sustain the prescribed rate of compression is one of the key results of the work. Of equal importance is the change of the volume of the bore of the tube during the compression from which the rate of fluid flow provided by the peristaltic pumping action was obtained. Also determined were the distributions of stresses and mechanical deflections at a succession of times during the compression cycle. Finally, the results of the structural analysis will be compared to the results found through a conventional, industry-standard analysis in order to highlight the potential discrepancies caused by simplifying assumptions.

Critical trauma situations provide the motivation for the work of Chapter Four. In such situations, it is necessary to provide blood at a body-compatible temperature and at a high flow rate as the appropriate therapeutic action. This chapter is concerned with the thermal and fluid flow design issues of a device suitable for this purpose.

The device in question is, in essence, a geometrically unique double-pipe heat exchanger. The geometrical uniqueness results from the nature of the pipe wall that separates the pipe flow and the annulus flow. By means of a continuous helical twist, the wall serves to create a swirl flow component superimposed on an axial flow both within the pipe proper and in the annular gap external to the pipe. Numerical simulation was used as the design tool. Results were obtained for both parallel and counter flow, and for both a constant fluid property model and a model which takes account of the temperature-dependence of the fluid properties.

Two thermal-hydraulic models were formulated and implemented. In one, the heat exchanger was analyzed as a single end-to-end entity. In the other, a spatially periodic model was created to enable attainment of rapidly applicable initial design results. Counter-flow operation yielded higher rates of heat transfer, but to an extent that depends on whether the fluid properties are temperature-dependent or are constant. The rate of heat transfer was found to be much more responsive to the pipe Reynolds number than to the annulus Reynolds number. Another accounted-for independent variable is the number of helical turns per unit length. The heat transfer results also included modular-based thermal resistances per unit length and overall heat transfer rates parameterized by flow configuration (counter or parallel flow), property constancy or variability, pitch of the helix, and the pipe and annulus Reynolds numbers. Local heat fluxes and temperature variations were conveyed by graytone-scaled portraits of the helical pipe wall.

The fluid flow results included pressure drop in both the pipe and the annulus, patterns of fluid flow conveyed by vector diagrams, and wall shear stress. The expected lesser pressure drop for parallel flow versus counter flow was validated for the pipe flow,
but the annulus flow showed a reversal in the relationship. Vector-displayed flow patterns were utilized to provide strong evidenced of the strong swirl imparted by the helical twist.

Numerical simulation was extensively employed during the course of the thesis research. The fluid mechanic situations considered here involve turbulent flow as well as swirl. Also

involved are convective heat transfer and thermodynamics, structural analysis, and sound generation. In the present-day utilization of numerical simulation for engineering applications, it is accepted practice to use turbulence models. There are many such models in the published literature, and it is incumbent on an investigator to establish the suitability of any chosen model for a selected problem. Normally, suitability is determined by laboratory experimentation. However, in the present instance, experimentation was precluded during the entire duration of this thesis because the mechanical engineering building was in a state of upheaval.

To cope with this situation, considerable effort was expended to verify the validity of the chosen turbulence model – the Shear Stress Transport (SST) model. The SST model brings together the venerable and commonly used $\kappa$-$\varepsilon$ model and the relatively newer $\kappa$-$\omega$ model. The former has been demonstrated to give rise to accurate results away from bounding surfaces whereas the latter has been shown to be highly effective in the near neighborhood of the bounding surfaces.

The Laboratory for Engineering Practice has had lengthy experience with the use of the SST model and has experimentally verified its competence for turbulent flow and heat transfer without swirl [1-3], turbulent flows in bends (elbows) were modeled by numerical simulation while making use of several turbulence models. It was found that the results based on the SST model were most congruent with experimental data for bends. In this regard, it is relevant to note that bend flows produce a substantial swirl. Similarly, in [4], a number of turbulence models were evaluated with respect to experimental data for a situation in which swirl dominated. Once again, comparisons showed that results predicted by the use of the SST turbulence model were in best agreement with the experimental data.

It is widely acknowledged that the most severe test of numerical simulation results is achieved by comparisons with local experimental data rather than by comparisons with global data. In that regard, local experimental data were sought for comparison with the author's own especially-performed numerical simulation predictions for the physical

situation of the experiments. In [5], turbulent flow experiments with controlled wall-driven swirl were performed, and data were collected for cross-sectional velocity profiles for both the streamwise and the tangential velocities.

The author has modeled the experimental situation of [5] with high fidelity, and a comparison of the numerically determined velocity profiles with those from the experiments is made in Fig 1.1. The predictions shown in the figure are based on the SST turbulence model. Inspection of the figure shows excellent agreement between the numerical predictions and the experimental data.

Three other turbulence models were also employed in the simulations. They are k-ε, Renormalized Group (RNG) k-ε, and k-ω. Results corresponding to these other turbulence models are respectfully presented in Figs 1.2, 1.3, and 1.4. Comparisons of the results conveyed in Figs 1.1-1.4 provide convincing evidence of the superior modeling capabilities of the SST turbulence model.

In light of the information conveyed in the foregoing paragraphs, there is a very strong case for the use of the SST turbulence for the problems dealt with in this thesis.

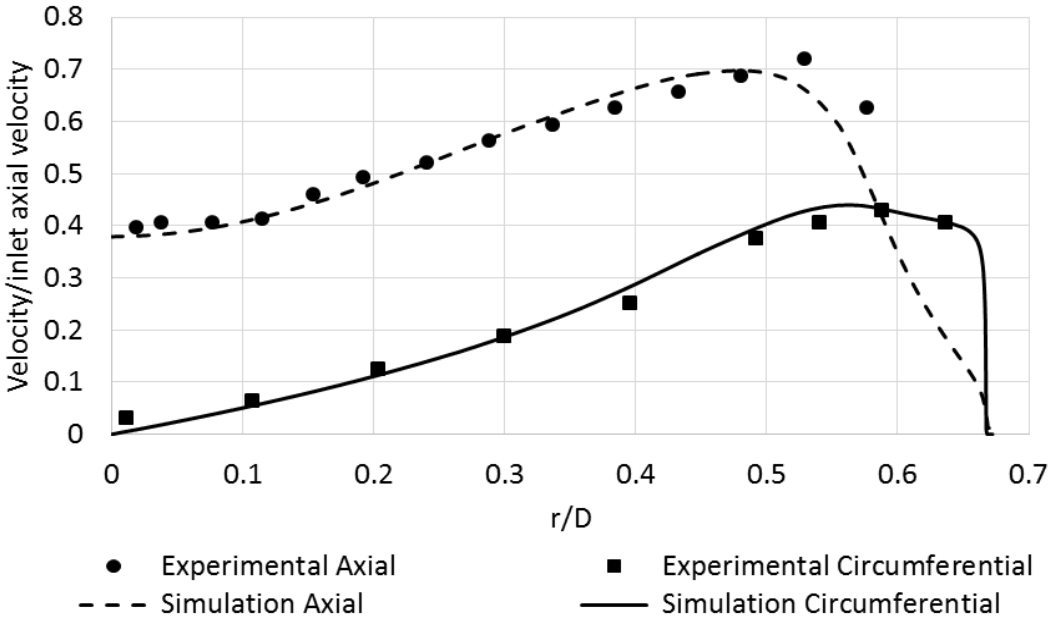


Fig. 1.1 Comparison of author-predicted numerical simulation velocity profiles with experimental data of [5]. The SST turbulence model was used in the simulation

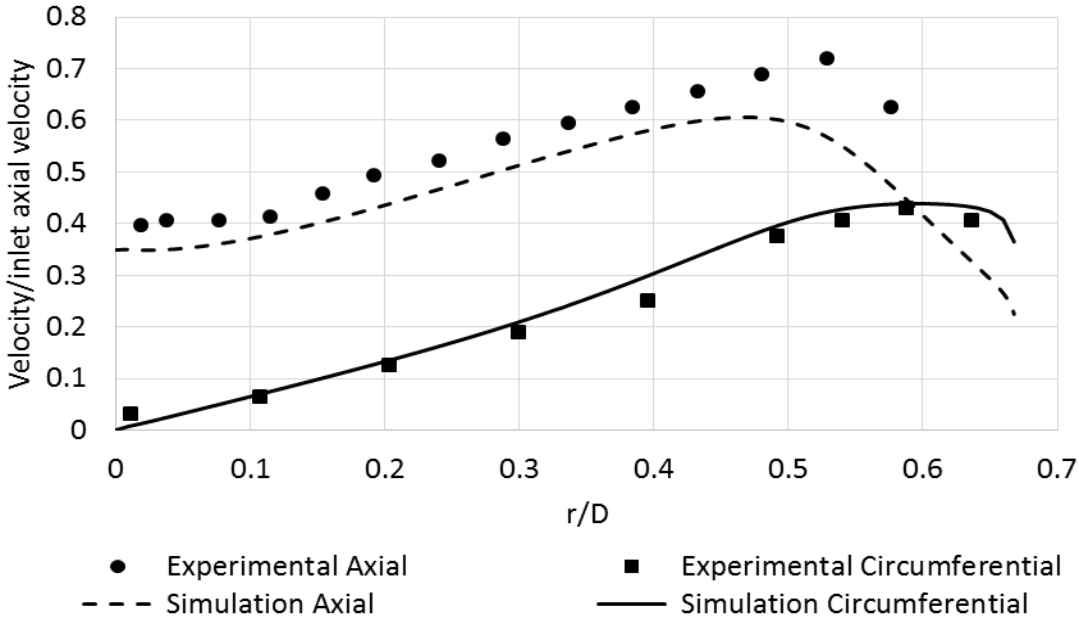


Fig. 1.2 Comparison of author-predicted numerical simulation velocity profiles with experimental data of [5]. The *k*-$\varepsilon$ turbulence model was used in the simulation

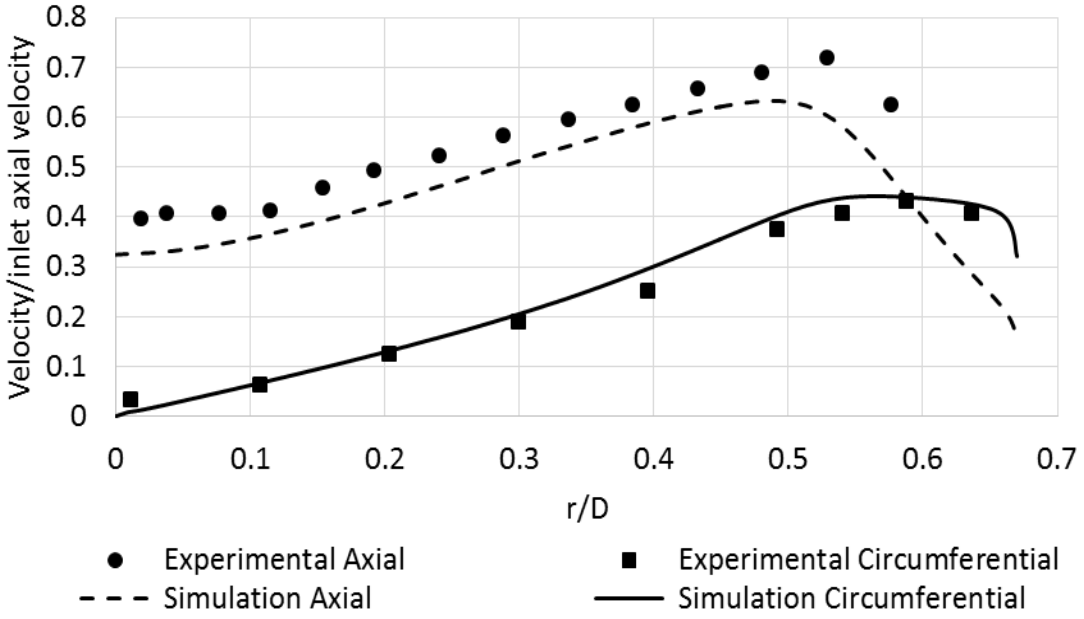


Fig. 1.3 Comparison of author-predicted numerical simulation velocity profiles with experimental data of [5]. The RNG *k*-*ε* turbulence model was used in the simulation

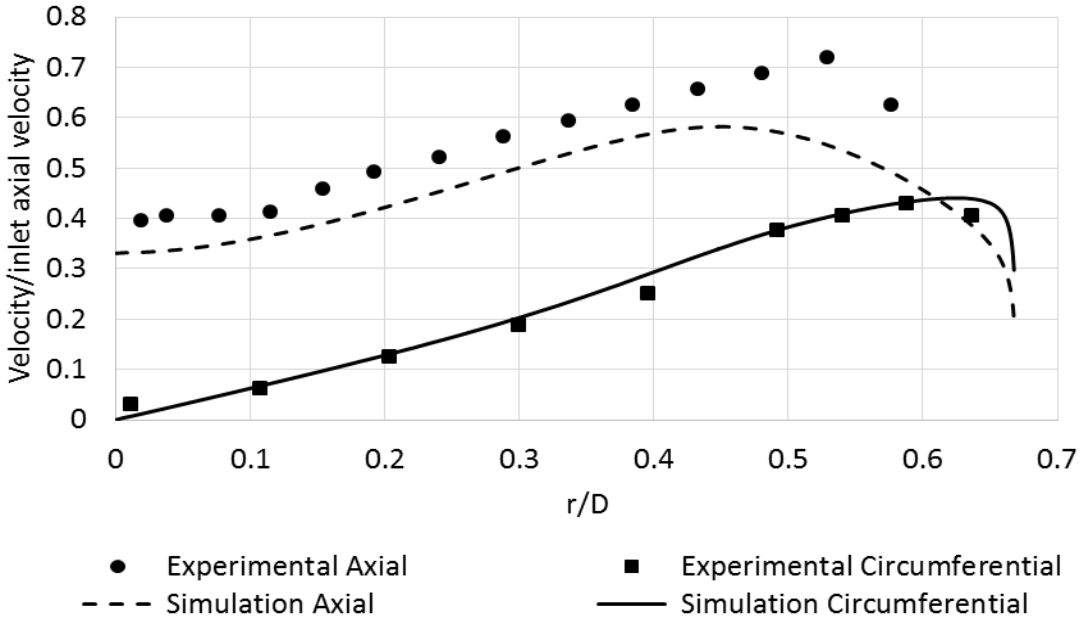


Fig. 1.4 Comparison of author-predicted numerical simulation velocity profiles with experimental data of [5]. The *k*-*ω* turbulence model was used in the simulation

# Chapter Two

# ADVANCED DESIGN MODALITY FOR A BIOMEDICAL THERAPEUTIC DEVICE: LUNG-CLEARANCE FLUID MECHANICS AND SOUND GENERATION

## 2.1 BACKGROUND

Cystic fibrosis is a genetic condition in which the lungs and digestive system become clogged with thick sticky mucus. Common outcomes are persistent lung infections and limitations on the ability to breathe. The cells that produce mucus, sweat, and digestive juices are majorly affected. In persons with cystic fibrosis, a defective gene causes a thick, buildup of mucus in the lungs, pancreas and other organs. In the lungs, the mucus clogs the airways and traps bacteria leading to infections, extensive lung damage and eventually, respiratory failure. In the pancreas, the mucus prevents the release of digestive enzymes that allow the body to break down food and absorb vital nutrients.

The success of therapeutic actions frequently depends on the degree of excellence of the device used to deliver the therapy. In this light, it is remarkable that in the totality of biomedical literature, the design of biomedical devices occupies a modest place. In view of the complex tasks that such devices are required to perform, it is appropriate that advanced tools be used for their design. This realization is the motivation for the research reported here. The focus of the work is the design of a lung clearance device which encompasses two main components, one of which is a controlled source of pressure of oscillating magnitude and frequency, and the other of which is a vest which receives the oscillating pressure and, in turn, imposes that pressure on the human diaphragm. The induced motion of the diaphragm loosens collected mucus and forces it out of the airway. The design of the pressure source is the current focus, and the design tools are computational fluid dynamics and sound generation theory.

There are a number of approaches for coping with cystic fibrosis, although there is no presently known cure. The two main coping approaches may be categorized as pharmaceutical and physiotherapeutical. The latter, which is the focus of the present investigation, makes use of physical agitation to loosen mucus and propel it toward larger vessels from which it can be more readily extracted, for example, by coughing. The physiotherapeutic approach can be implemented either in an *ad hoc* manner or by means of a biomedical device. Such devices are often based on fluid mechanics. There are, in fact, several such devices commercially available.

A substantial literature which deals with physiotherapeutic methodologies for dealing which cystic fibrosis exists [6-25]. For the most part, the literature is qualitative and discursive and is devoid. Only in [6-8] was it recognized that there is a need to involve fluid mechanics in a rational design of an airflow-based therapeutic device. The employed models were based on electric circuit theory, with the only fluid mechanics being the well-known Poiseuille formula for fully developed, steady laminar flow in a round pipe. Neither the open passages in the lungs nor the airways proper are suitable facsimiles of the round-pipe, Poiseuille-flow geometry. Furthermore, the lengths of the flow passages are not long enough to enable fully developed fluid flow. The most serious departures from the Poiseuille model are the intrinsic transient and three-dimensional natures of the airflow-based therapy which violate the steady-state and one-dimensional limitations of the Poiseuille flow.

To obtain a design which rests firmly on the underlying laws of fluid mechanics requires an analysis approach which is capable of handling the complexities inherent in unsteady, three-dimensional pulsating fluid flow in intricate geometries. The approach utilized here is focused on fluid mechanical issues. It consists of devising a realistic physical model which will be translated into a numerical simulation model and then implemented by suitable computer resources. The focus of this work is to demonstrate for the first time that fluid mechanic theory and numerical simulation models can be used advantageously for

the design of device-based physiotherapeutic treatment of cystic fibrosis and sister maladies.

The category of biomedical devices of interest here is pictured photographically in Fig. 2.1. As seen there, the physiotherapeutic device consists of two distinct components. The component at the left, designated here as the airflow module, is an air-moving device incorporating a means of providing an oscillatory, pulsating flow. In contrast, the component at the right is a vest-like garment which is connected to the airflow module by means of two flexible conduits. Due to the fluctuating nature of the airflow, each conduit serves alternatively as an air delivery and an air extraction means. The vest receives a periodically fluctuating pressure superimposed on a steady above-atmosphere value. The fluctuating pressure loosens the mucus and drives it toward larger vessels with enable efficient extraction.

There are several means by the airflow module produces a periodically fluctuating flow. For example, one modality may be a periodically changing plenum chamber volume. Another is the use of reciprocating pistons. Still another is a valve whose minimum area changes with time. It is clear that these modalities as well as others that are presently in use depend fundamentally on fluid flow processes. In the present approach, the participating fluid flow processes are modeled with high fidelity by means of numerical simulation so that accurate predictions can be made about the nature of the delivered airflow. The focus of the present investigation is the airflow module.

Fig. 2.1 Typical physiotherapeutical device for treatment of cystic fibrosis and related breathing dysfunctions

## 2.2 PHYSICAL SITUATION

The airflow module to be investigated here is based on the use of timewise variations of the opening area of a valve to provide the means of obtaining a controlled oscillating flow. The valve in question will be designated as a *rotating-disk valve*. An exploded view of the primary components of a generic version of such a valve is illustrated schematically in Fig. 2.2.

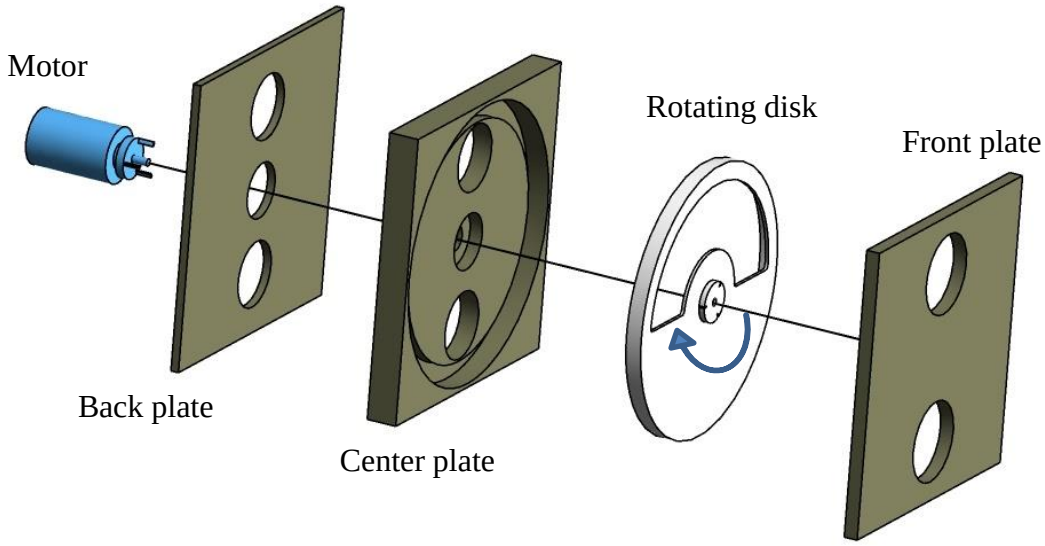


Fig. 2.2 Exploded view of a rotating-disk valve

As seen in the figure, the valve is constructed of three stationary parallel plates and a rotating disk. The rotating disk is recessed into the center plate. Of particular note is the 180-degree open slot in the rotating disk. That slot enables air to pass from the forward face to the rearward face of the assemblage (or vice versa) when the circular apertures in the stationary plates are aligned with each other and with the open slot. The second apertures in each of the stationary plates are devoid of airflow when the first apertures are actively transporting airflow. As the rotating disk revolves, air is able to pass through it by its alignment with either the upper or lower apertures in the stationary plates. The shaft is rigidly connected to an electric motor situated behind the disk assembly.

Air is supplied at a constant volumetric flowrate to the back face of the assemblage by a steadily operating blower. The air emerging from the front face is collected in a plenum chamber (not shown). In the downstream face of the plenum chamber, there are two apertures, each connected to a conduit which conveys the air emerging from the plenum to the therapeutic garment.

A side view of the assembled components is presented in Fig. 2.3. For reasons of clarity, the center plate is not shown in order to highlight the presence of the rotating disk. The apertures in the respective components are shown as dashed lines. It is readily seen from the figure that air passing into the assemblage from the back plate is not ducted definitively into the aperture in the rotating disk. As a consequence, the air that has passed through the back face may leak into the gap between the plate and the disk. A similar leakage may occur as the air passes through the disk. These escapes routes for air enable the blower to operate continuously even when air is not delivered to the therapeutic garment.

Another informing illustration is presented in Fig. 2.4 which shows a fully assembled side view (Part (a)) and a front face view (Part (b)). In the (a) part, the gaps are not shown because they are sealed at their outer edges. Part (b) shows that the front face apertures are provided with seats to enable the attachment of hoses to convey the air to the inlet of a plenum chamber.

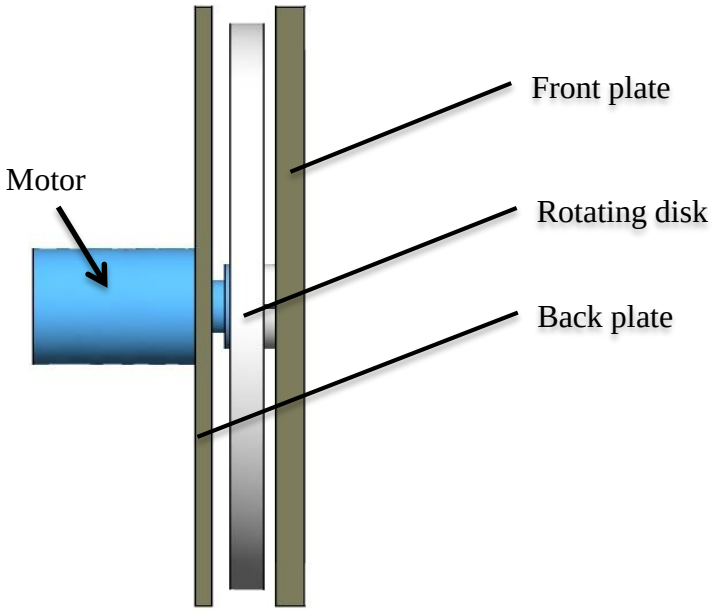


Fig. 2.3 Side view of the assemblage with the center plate removed for clarity

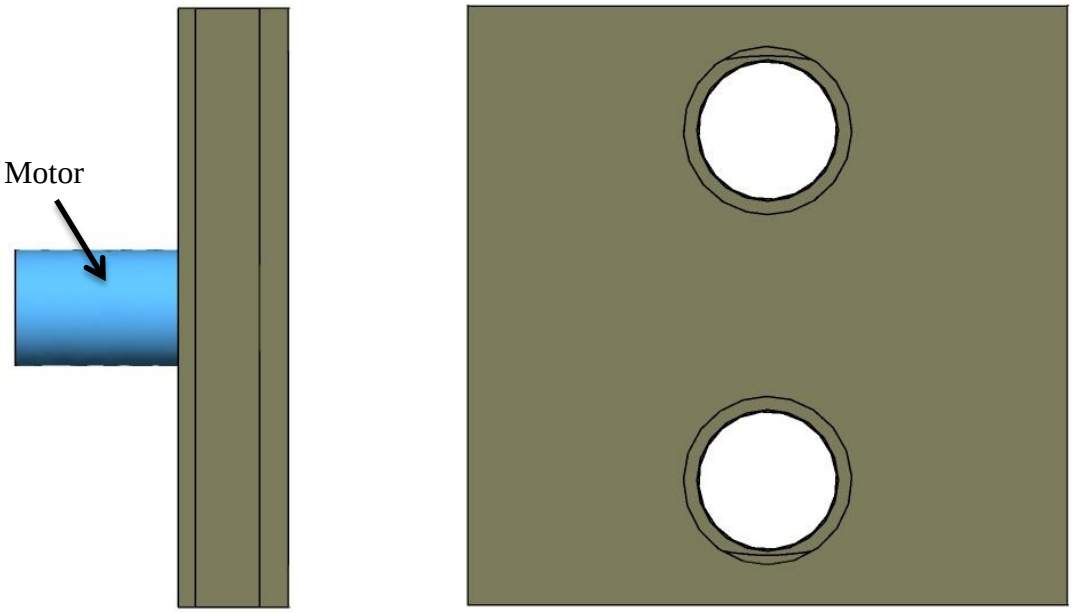


(a) (b)

Fig. 2.4 Further details of the airflow module. (a) side view, (b) front-face view

One more view is presented in Fig. 2.5 to clarify the interactions of the rotating disk with the other components. It can be seen from the figure that there is a thin annular gap between

the outer radius of the rotating disk and the inner radius of the recess. As pictured in the figure, the open recess in the rotating disk is aligned with the upper aperture in the center plate. In contrast, the lower aperture in the plate is blocked by the solid portion of the rotating disk. That aperture is shown as a shadow in the figure. The rotating shaft is rigidly connected to the rotating disk but does not interact with any of the stationary plates.

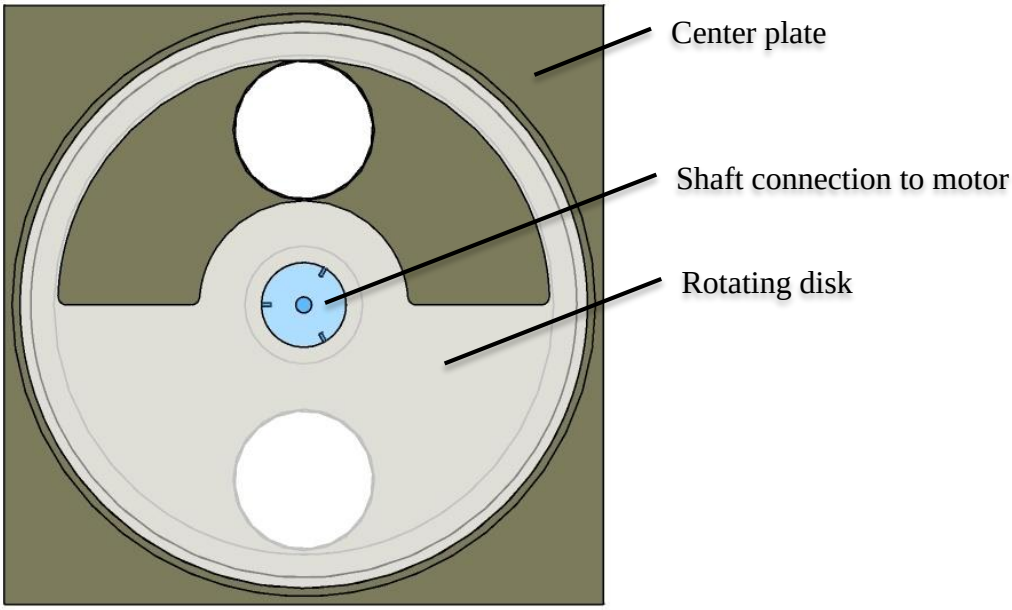


Fig. 2.5 Rotating disk housed in a recess in the center plate. The front plate has been removed for clarity

A final figure, Fig. 2.6, has been prepared, to demonstrate with the upmost clarity, an actual operating mode of the device. The figure, a longitudinal section, shows how the components mate with each other when the device is operating. As configured, the figure displays the alignment that enables airflow to pass continuously through the upper apertures, while the lower apertures are blocked. Although the blower-driven flow passes from left to right through the upper apertures, it is possible in transient operation for air to exit the therapeutic garment from left to right. By the same token, even though the lower apertures are blocked, it is still possible for a transient outflow from the therapeutic garment to occur. Quantitative information on these transient flows will be displayed in the presentation of results.

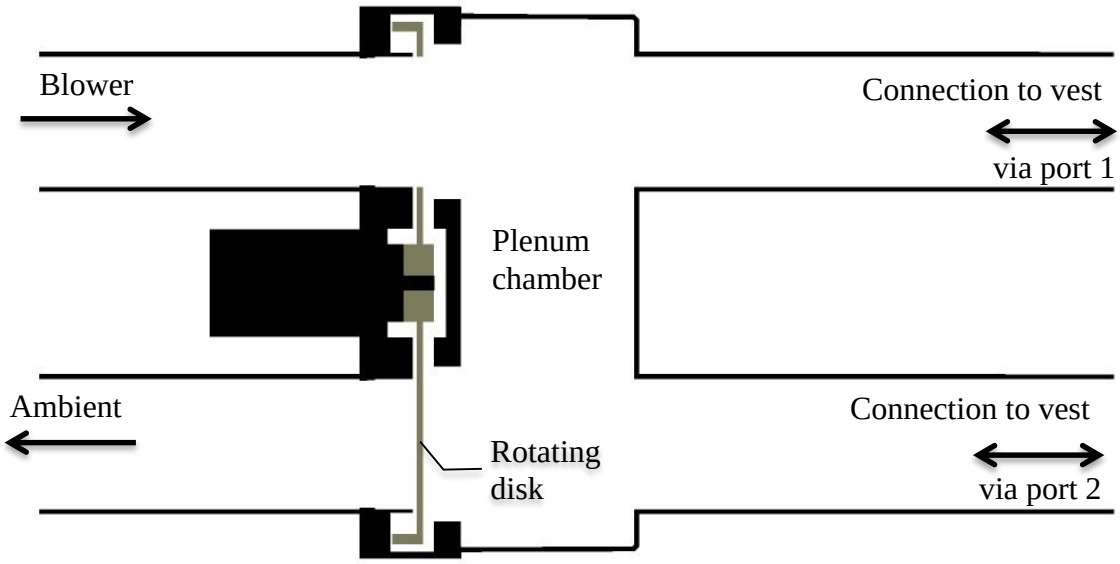


Fig. 2.6 Device configuration for an operating mode in which the upper apertures are open and the lower apertures are blocked

## 2.3 FLUID MECHANIC NUMERICAL SIMULATION

### 2.3.1 Governing Equations

Due to the complex fluid-flow situation, a model capable of accommodating both laminar and turbulent flow that is both three-dimensional and unsteady is required. To accommodate the complex nature of the fluid flow, the SST model was adopted [26]. This model has already been proven by means of experimental validation [1-3] to be suitable for the solution task. The SST model brings together the venerable and commonly used $\kappa$-$\varepsilon$ model and the relatively newer $\kappa$-$\omega$ model. The former has been demonstrated to give rise to accurate results away from bounding surfaces whereas the latter has been shown to be highly effective in the near neighborhood of the bounding surfaces. The quantity $\kappa$ is the turbulence kinetic energy, $\omega$ is the specific rate of turbulence dissipation, and $\varepsilon$ is rate of dissipation.

The relevant physical principles that govern the fluid flow are momentum conservation (Reynolds Averaged Navier-Stokes (RANS) equations) and mass conservation. These equations are written here for incompressible, constant property, unsteady, three-dimensional turbulent flow, with the properties being those of air at 25ºC.

The RANS equations, as written in Cartesian tensor form, are

$$\rho\frac{\partial u_j}{\partial t}+\rho\left(u_i\frac{\partial u_j}{\partial x_i}\right)=-\frac{\partial p}{\partial x_j}+\frac{\partial}{\partial x_i}\left((\mu+\mu_{turb})\frac{\partial u_j}{\partial x_i}\right)+S_{rotation}\quad i=1,2,3\quad j=1,2,3 \tag{2.1}$$

and the mass conservation equation is

$$\frac{\partial u_i}{\partial x_i}=0 \tag{2.2}$$

The quantity $\mu_{turb}$ is designated as the turbulent viscosity. The determination of $\mu_{turb}$ is achieved by means of the Shear Stress Transport (SST) turbulence model.

The governing equations for the SST turbulence model are

$$\frac{\partial(\rho\kappa)}{\partial t}+\frac{\partial(\rho u_i\kappa)}{\partial x_i}=P_\kappa-\beta_1\rho\kappa\omega+\frac{\partial}{\partial x_i}\left[\left(\mu+\frac{\mu_{turb}}{\sigma_\kappa}\right)\frac{\partial\kappa}{\partial x_i}\right] \tag{2.3}$$

$$\frac{\partial(\rho\omega)}{\partial t}+\frac{\partial(\rho u_i\omega)}{\partial x_i}=A\rho S^2-\beta_2\rho\omega^2+\frac{\partial}{\partial x_i}\left[\left(\mu+\frac{\mu_{turb}}{\sigma_\omega}\right)\frac{\partial\omega}{\partial x_i}\right]+2\rho(1-F_1)\frac{1}{\sigma_{\omega 2}\omega}\frac{\partial\kappa}{\partial x_i}\frac{\partial\omega}{\partial x_i} \tag{2.4}$$

The solution of Eqs. (2.3) and (2.4) yields values of $\kappa$ and $\omega$, which give the turbulent viscosity $\mu_{turb}$ from

$$\mu_{turb}=\frac{\alpha\rho\kappa}{\max(\alpha\omega,SF_2)} \tag{2.5}$$

The other term in Eq. (2.1) that is worthy of discussion is the source term $S_{rotation}$. This term arises due to the presence of a rotating solution domain which makes use of a rotating frame of reference at a specified angular velocity $\psi$. This source terms includes both the

Coriolis force and centrifugal momentum terms. The additional momentum terms, when expanded, are

$$S_{rotation} = -\rho \boldsymbol{\psi} \times (\boldsymbol{\psi} \times \boldsymbol{r}) - 2\rho \boldsymbol{\psi} \times \boldsymbol{u_\theta} \tag{2.6}$$

where the first term is the centrifugal term, and the second represents the Coriolis forces. In the equation, $\boldsymbol{r}$ is the position vector, and $\boldsymbol{u_\theta}$ is the rotating frame velocity.

The node count for the combined rotating and stationary solution domain was 4,900,000, which led to an average y+ value of 6.9 across the solution domain. Since the results were time varying, it was necessary to choose a sufficiently small time step to accurately capture the fluid mechanic results. The chosen time step which gave a timewise converged solution was 0.0005 seconds. Results will be presented subsequent to the attainment of a timewise periodically-developed state (variations in results from one cycle to another cycle less than 5%). All of the forthcoming results are presented for instantaneous moments in time.

### 2.3.2 Boundary Conditions

For the present design, pressurized air is delivered to the rotating-disk valve device from a blower located upstream as shown in Fig. 2.6. At the inlet to the solution domain, a constant volumetric flow rate was specified (40 $ft^3$/min or 1.13 $m^3$/min) with a turbulent intensity of 5%. The exit from the device to ambient (Fig. 2.6) was modeled as an opening with entrainment and zero gradient for turbulence. The rotating disk and corresponding rotating solution domain had a specification of five revolutions per second. In order to take account of the time-dependent conditions occurring within the therapeutic vest, a representative but realistic time-varying pressure boundary condition, with zero gradient for turbulence, was selected as shown in Fig. 2.7. This pressure variation was based on normal operation for a vest with a maximum volume of 0.014 $m^3$ when the disk valve was rotating at five revolutions per second.

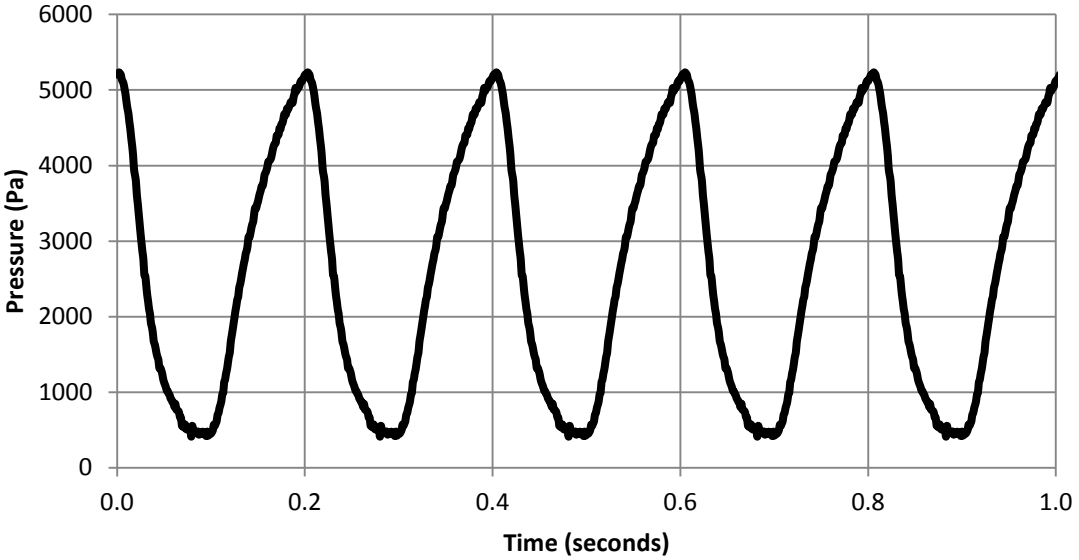


Fig. 2.7 Representative pressure boundary condition corresponding to the vest's response (expansion and contraction) over time for a disk valve rotating at five revolutions per second

## 2.4 SOUND POWER ANALYSIS

The goal of this sound-focused analysis is to determine the distribution of the sound power level (SWL) generated throughout the interior of the device. This quantity is not to be confused with the sound pressure level (SPL), a quantity which is experienced at specific locations in the external surroundings of the device. In order to determine sound power level, the model set forth in Proudman [27] is employed here. The magnitude of the SWL is related to the local sound intensity $I_A$ in units of W/m$^2$ and to a reference sound intensity $I_o$ whose value for air is $10^{-12}$ W/m$^2$.

The equation connecting the SWL and these intensities is

$$SWL = 10 \cdot \log_{10} \frac{I_A}{I_o} \tag{2.7}$$

In turn, $I_A$ can be found from

$$I_A = \frac{P_A^2}{\rho a_o} \tag{2.8}$$

where $P_A$ is the acoustic power due to a unit volume of isotropic disturbance, $\rho$ is the air density (1.185 kg/m$^3$), and $a_o$ is the speed of sound in air (343 m/s) [25].
Further, $P_A$ can be related to the turbulence properties of the flow by

$$P_A = \alpha \rho \epsilon \left(\frac{\sqrt{2\kappa}}{a_o}\right)^5 \tag{2.9}$$

where $\alpha$ is a numerical constant (~38 s from [27]), $\epsilon$ is the turbulence dissipation in the fluid, and $\kappa$ is the turbulent kinetic energy. These turbulence properties are provided by the CFD software. Therefore, the successive use of Eqs. (2.7-2.9) provides the sound power level distribution.

## 2.5 RESULTS AND DISCUSSION

The presentation and discussion of results will be subdivided into two main sections: fluid-mechanic results and sound-power results.

### 2.5.1 Mass Flowrates

The first focus of the fluid-mechanic results are mass flow rates at the individual inflow and outflow ports of the device. This information is conveyed in Fig. 2.8, where the port-specific mass flow rates are plotted as a function of time over a span of three cycles. The figure shows information after the completion of the startup transient. It can be seen from the figure that temporal periodicity prevails. The figure conveys five curves, respectively for the inflow port, the ambient outflow port, the two ports by which the device interacts with the therapeutic vest, and the sum of the mass flows in the latter pair of ports. To fulfill a mass balance, attention is to be focused on three of the curves: inflow, outflow, and sum of ports 1 and 2. At any moment of time, the sum of the flows represented by the aforementioned trio of curves is zero. Another feature that can be verified from the figure is that the cycle average of the mass flows represented by the sum of ports 1 and 2 must be zero.

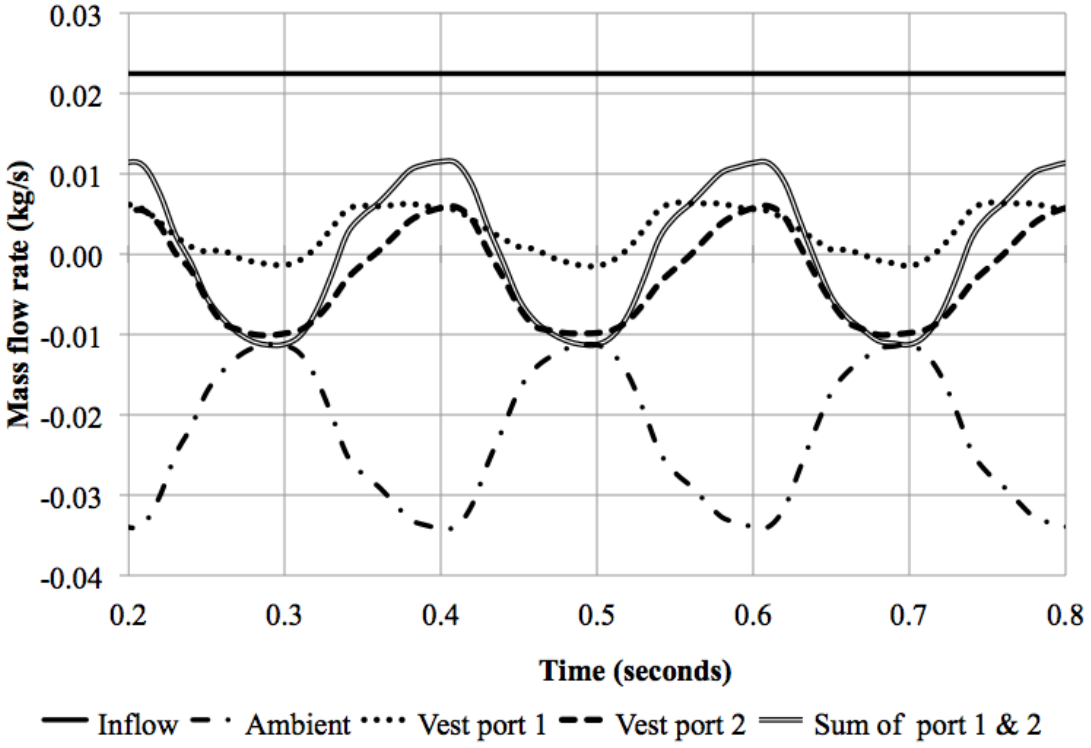


Fig. 2.8 Timewise variations of the mass flow rates at the inlet and exit ports of the device

The results that follow are parameterized by the angular position of the rotating disk. To provide an unambiguous connection between the specification of an angular position and the opening slot of the disk, Fig. 2.9 has been prepared. The figures consist of nine subsections, each of which corresponds to an angular position. The angles are 0, 45, 90, … 360 $^{o}$. As can be seen from the figure, the angular positions 45, 90, 135, 180 $^{o}$ correspond to mass passing through the upper apertures, whereas positions 225, 270, 315, and 360/0 $^{o}$ activate the lower apertures.

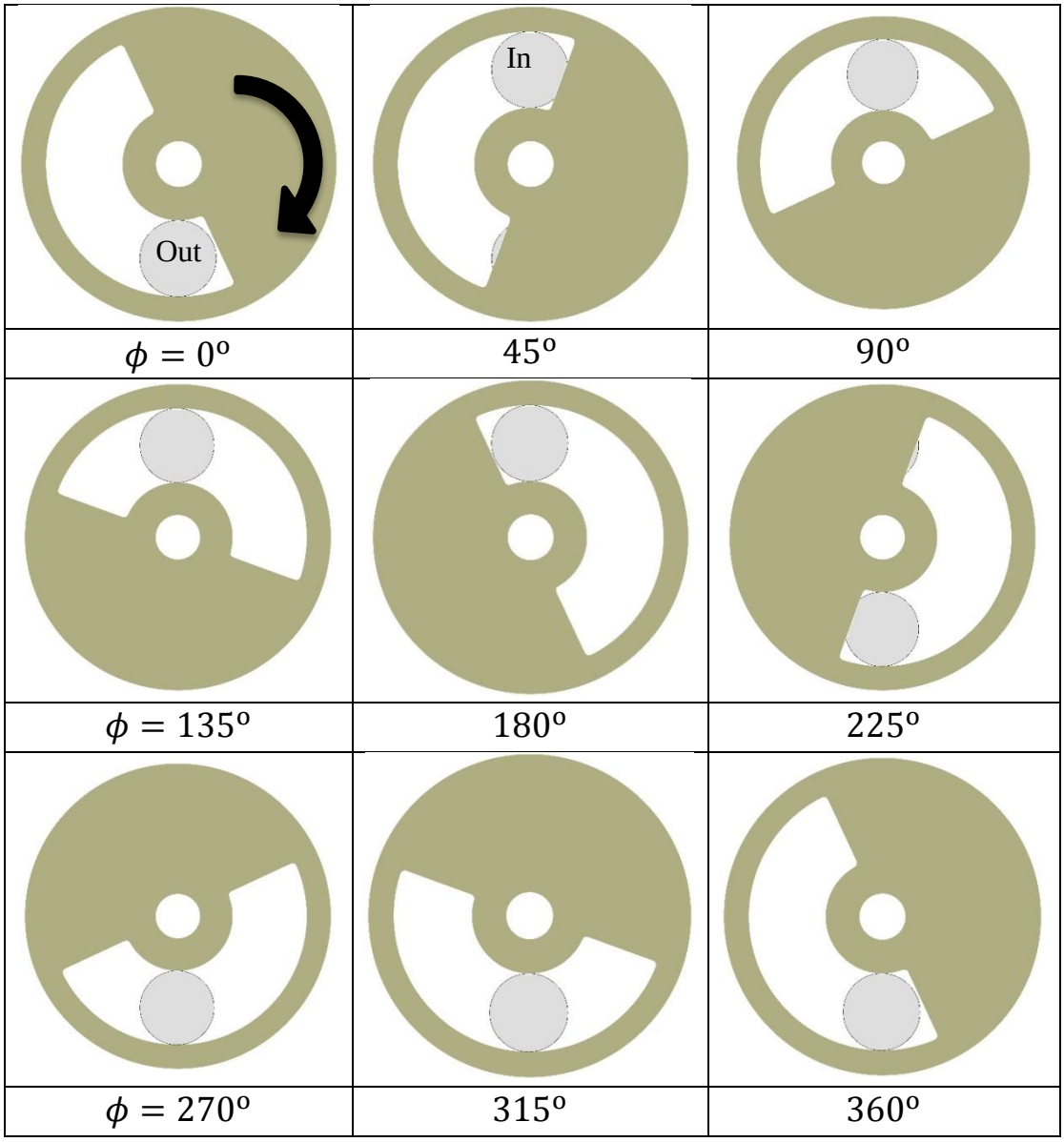


Fig. 2.9 Definition of angular positions with respect to the open or closed orientation of the apertures in the device

With the foregoing definitions of the angular positions, the mass flow rates already displayed in Fig. 2.8 can now be presented as a function of angle. This presentation is conveyed in Fig. 2.10. The figure had dual abscissa scales, with the upper scale showing the angular positions during one cycle and the lower scale showing the corresponding times

during a single cycle. This figure enables a more careful evaluation of the various processes that occur at specific angular orientations of the rotating disk. If the mass flow rate at the ports 1 and 2 are positive, mass is entering the system from the vest. This condition occurs both at the start and end of the cycle. With regard to the exiting mass flow rate from the device to the ambient, the greatest magnitudes of the outflow occur, once again, at the beginning and ending of the cycle.

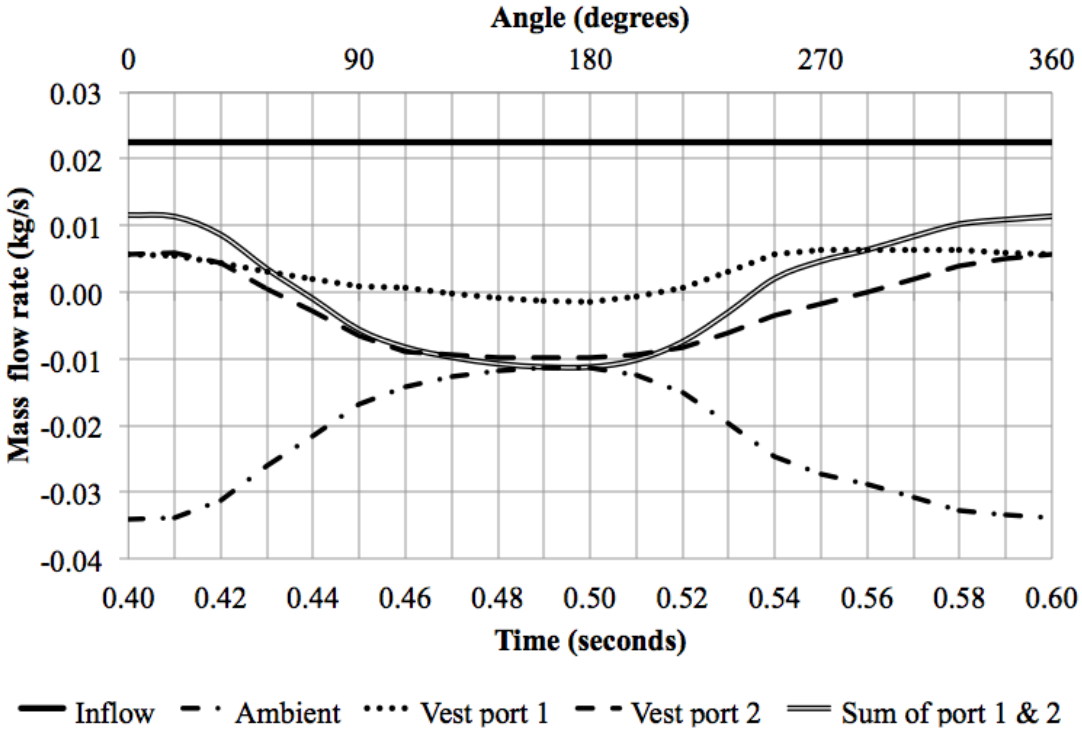


Fig. 2.10 Variations of the mass flow rates at the inlet and exit ports of the device as a function of angular position of the rotating disk

### 2.5.2 Patterns of Fluid Flow via Vector Diagrams

The next focus of the presentation of the fluid-mechanic results are the patterns of flow within the device as a function of the angular position of the rotating disk. All told, eight angular positions are considered for the presentation. Vector diagrams are used to illuminate the flow patterns. For each angular position, two vector diagrams are displayed respectively in parts (a) and part (b). The (a) part of each figure displays unnormalized

vectors whose lengths are directly proportional to the magnitude of the velocity. In contrast, the (b) part shows normalized vectors all of whose lengths are the same. The information conveyed by the normalized vectors is the direction of the local velocity but not the magnitude. It is believed that this information about the flow patterns in the device will be beneficial to the design of the vest.

Figure 2.11 conveys results for the $\phi = 0^o$ situation. For this case, air is passing from the therapeutic vest to the device through both of the interconnecting conduits. The outcome of this condition is that the outflow of air to the ambient exceeds the inflow of air from the blower to the device as witnessed by the longer and darker vectors in the outflow channel. Also seen is that the upper conduit which interconnects the device to the vest is carrying more fluid than is the lower conduit. Within the plenum there are numerous recirculation zones but the circulating velocities are small as seen in the (a) part of the figure.

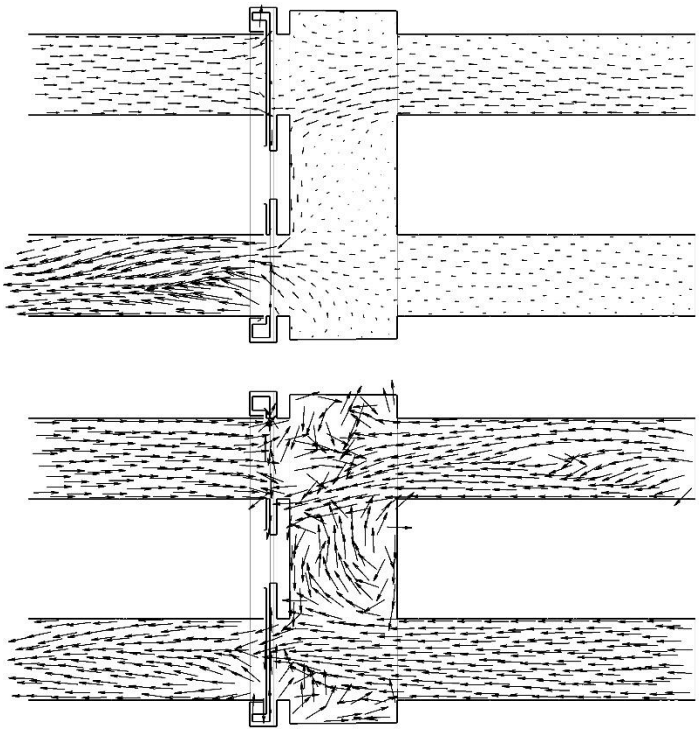

Fig. 2.11 Patterns of fluid flow in the device for the angular orientation $\phi = 0^o/360^o$

Attention will now be turned to Fig. 2.12 which displays flow pattern results for the angular orientation $\phi$ = 45º. Comparison of Fig. 2.12 with the foregoing Fig. 2.11 shows that the directions of flow are unchanged for these two cases. The main differences are the diminished magnitudes of the flow in the plenum chamber and that passing from the vest into the device.

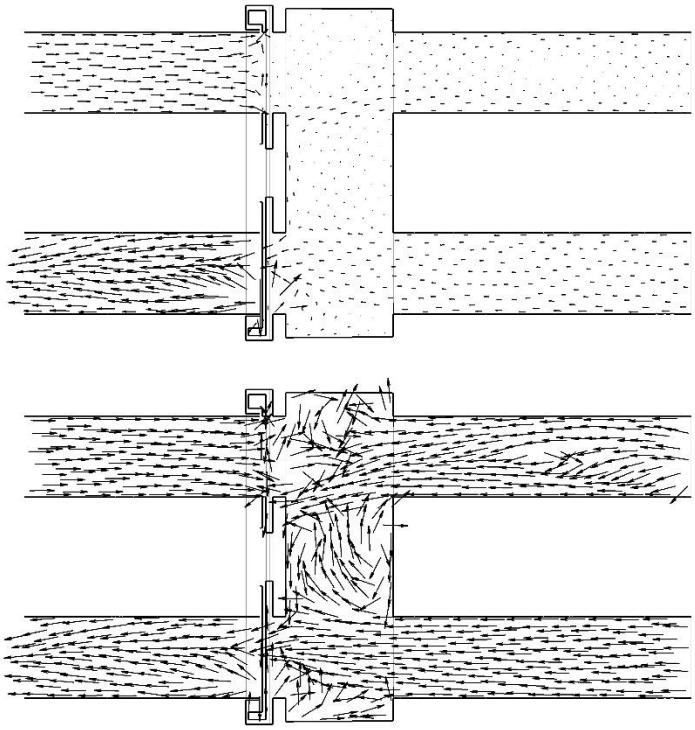

Fig. 2.12 Patterns of fluid flow in the device for the angular orientation $\phi = 45^{o}$

The flow patterns for the $\phi = 90^{o}$ are exhibited in Fig. 2.13. Examination of the (b) part of the figure reveals that the direction of flow in the interconnecting conduits has shifted from the earlier direction (from the vest to the device) to the current direction from the device into the vest. However, the magnitude of this flow, seen in the (a) part is exceedingly small.

For the angular position $\phi = 135^{o}$, shown in Fig. 2.14, the flow direction in the conduits connecting the device to the vest is maintained as it was for $\phi = 90^{o}$, generally from the device to the vest. The magnitude of the flow in the lower conduit is somewhat greater than

that of the upper conduit. However, the outflow from the device to the ambient via the exit conduit is not as orderly as for the previously discussed cases. The reason for the current departure from unidirectional flow is the blockage caused by the orientation of the rotating disk. In the plenum, lower velocities generally prevail, however somewhat larger velocities are seen in the lower portion.

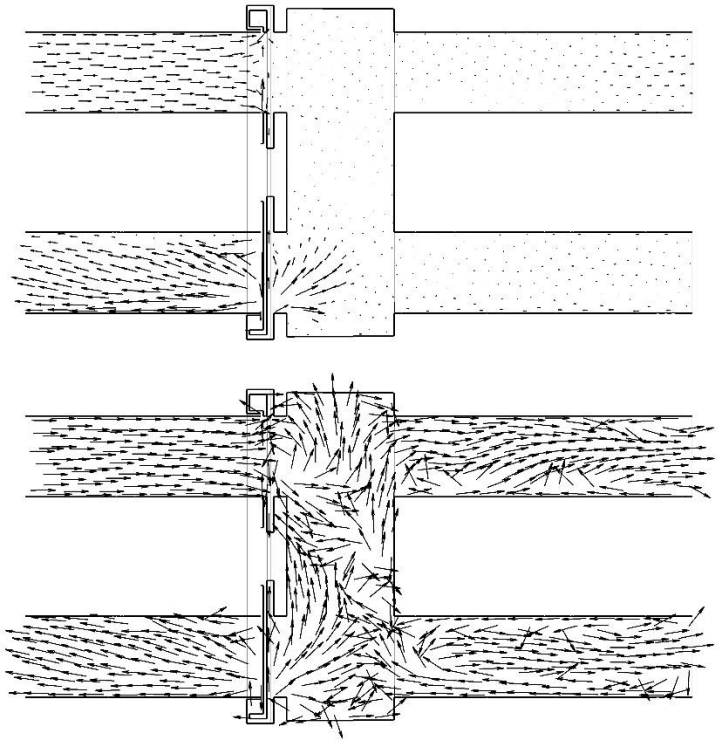

Fig. 2.13 Patterns of fluid flow in the device for the angular orientation $\phi = 90^{o}$

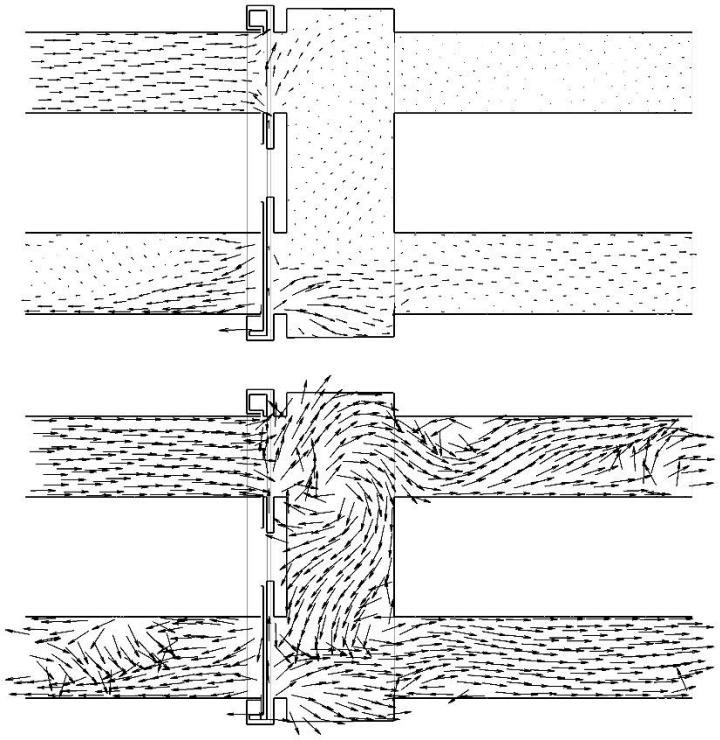

Fig. 2.14 Patterns of fluid flow in the device for the angular orientation $\phi = 135^{o}$

For the $\phi = 180^{o}$orientation shown in Fig. 2.15, the upper and lower interconnecting conduits display distinctly different flow patterns. The lower of the two conduits is seen to be delivering flow to the vest at a magnitude that is readily discerned in part (a) of the figure. In contrast, the upper conduit displays a chaotic flow pattern whose magnitude is minimal. The conduit that carries fluid from the device to the ambient is also experiencing a chaotic flow pattern.

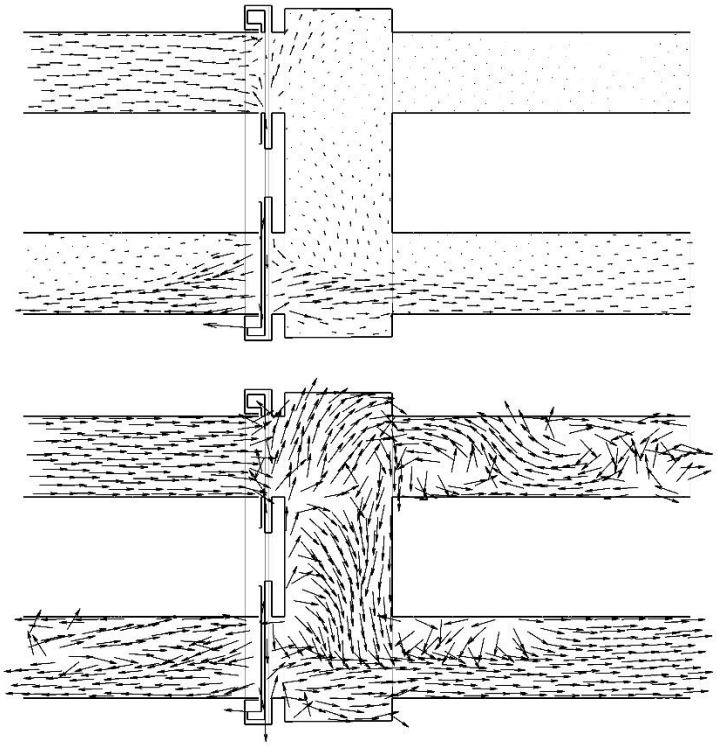

Fig. 2.15 Patterns of fluid flow in the device for the angular orientation $\phi = 180^{o}$

The next angular position to be discussed is $\phi = 225^{o}$ in Fig. 2.16. Gone are the chaotic flow behaviors in the upper device-vest conduit and in the exit flow conduit. Now, there is an unambiguous flow from the vest to the device through the upper conduit and a reverse flow in the lower conduit. Among these two flows, that in the upper conduit is of slightly greater magnitude. The conduit from the device to the ambient carries a unidirectional outflow.

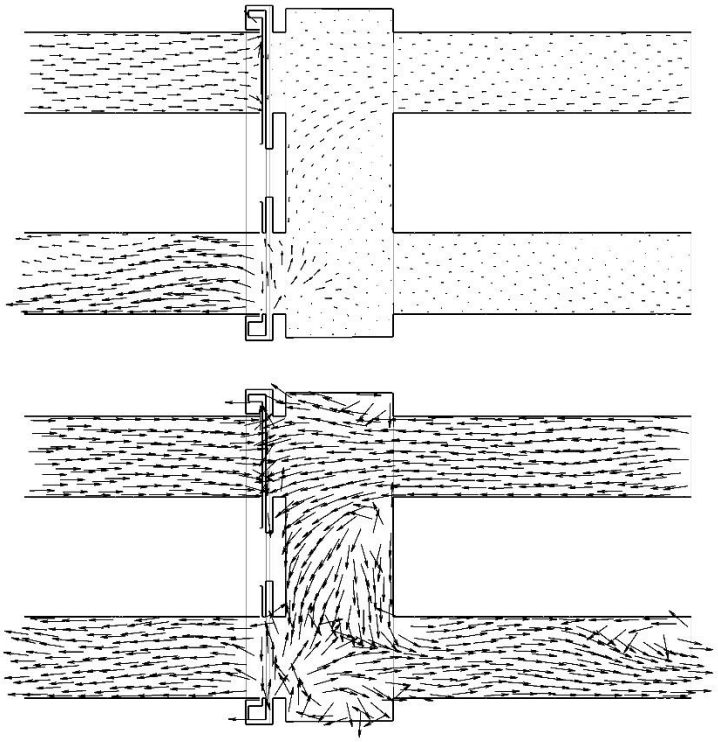

Fig. 2.16 Patterns of fluid flow in the device for the angular orientation $\phi = 225^{o}$

In Fig. 2.17, the angular position $\phi = 270^{o}$ shows a flow direction from the vest to the device through the upper conduit. However, the virtually vanishing flow in the lower conduit is highly chaotic. The magnitude of the outflow of air from the device as a whole is now larger than the magnitude of the inflow.

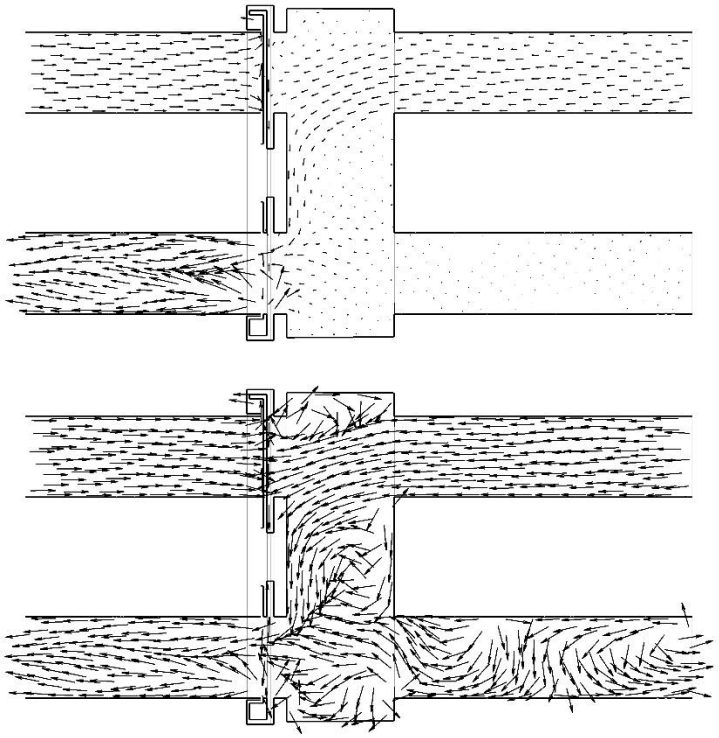

Fig. 2.17 Patterns of fluid flow in the device for the angular orientation $\phi = 270^{o}$

The patterns of fluid flow for the $\phi = 315^{o}$ as shown in Fig. 2.18 bears a strong resemblance to those for the $\phi = 0^{o}/360^{o}$ case. Both of the interconnecting conduits are delivering flow from the vest to the device, with a slightly stronger flow in the upper conduit. The inflow and outflow conduits carry nearly one-dimensional flows with the magnitude of the outflow being somewhat greater than that of the inflow.

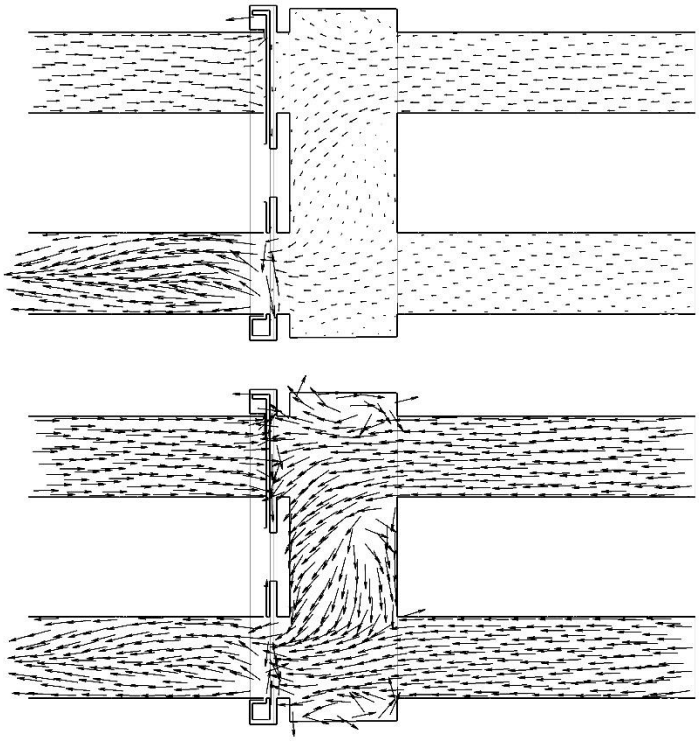

Fig. 2.18 Patterns of fluid flow in the device for the angular orientation $\phi = 315^{o}$

### 2.5.3 Velocity Distributions

The next category of results is velocity distributions. This information has at least two significant uses. One of these is the quantitative data that is relevant to the rates at which air is either delivered to or extracted from the vest. The other has to do with the production of sound pressure. The device in question serves best when it does not create undesirable side effects such as sound.

Velocity information will be displayed with the apparatus geometry as the background with superposed velocity magnitudes shown by graytones. The figure for a specific angular position of the rotating disk is keyed to a graytone scale which is particular to the velocities that are encountered at that angular position. Figure 2.19 displays velocity results for angular positions of 0, 45, and 90$^{o}$. The signs corresponding to the graytone-

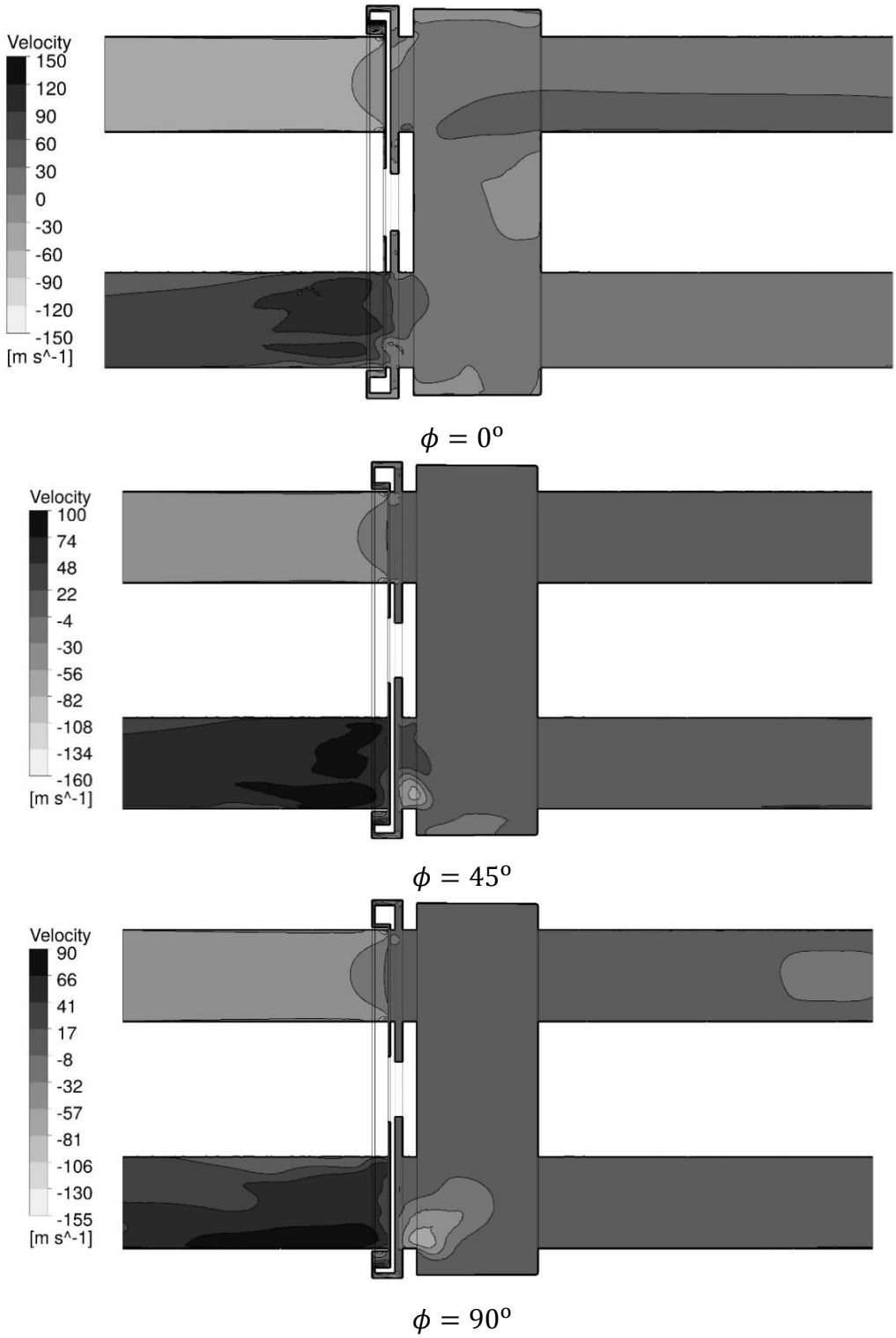


Fig. 2.19 Velocity distributions for angular positions of the rotating disk equal to $\phi$ = 0, 45 and 90º

scale are, respectively, negative when the flow is from left to right and positive when the flow is right to left. Inspection of the $0^o$ velocity results in the figure show large zones of relatively uniform velocity. The only regions where there are gradients of color are the outflow conduit through which air passes from the device to the ambient and the upper interconnecting conduit between the device and the vest. For the rotating disk positions of 45 and $90^o$, the disposition of the graytones is generally similar to what has been observed for the $0^o$ position. However, a topographic-like contour feature makes an appearance near the exit aperture in the $45^o$ image and enlarges in the $90^o$ image. Also worthy of note is the range of magnitudes of the velocities encountered in Fig. 2.19. These magnitudes may range from -150 to 150 m/s.

The next figure, Fig. 2.20, conveys results for disk angular positons of 135, 180, and $225^o$. For the first of these angles, the velocity graph is not majorly different from those displayed in Fig. 2.19. For the $180^o$ angular position, greater graytone variations are seen, indicating a less uniform velocity distribution. Greater uniformity appears to return for the velocity results for the $225^o$ angular position.

Figure 2.21 conveys velocity results for the angular positions of 270, 315, and $360^o$. For the first of these positions, velocity variations are in evidence in the upper device--vest conduit, in the plenum chamber, and in the conduit that conveys the air to the ambient. In the case of the $315^o$ angular position, the two device--vest conduits experience relatively uniform velocities while the plenum velocity distribution is more or less the same as that for the $270^o$ orientation. Interestingly, for the first time, there are velocity variations in the conduit that delivers air to the device. The outflow conduit continues to experience the most complex velocity distribution. The results of Fig. 21 for the $360^o$ orientation are identical to those already displayed in Fig. 19 for the $0^o$ orientation.

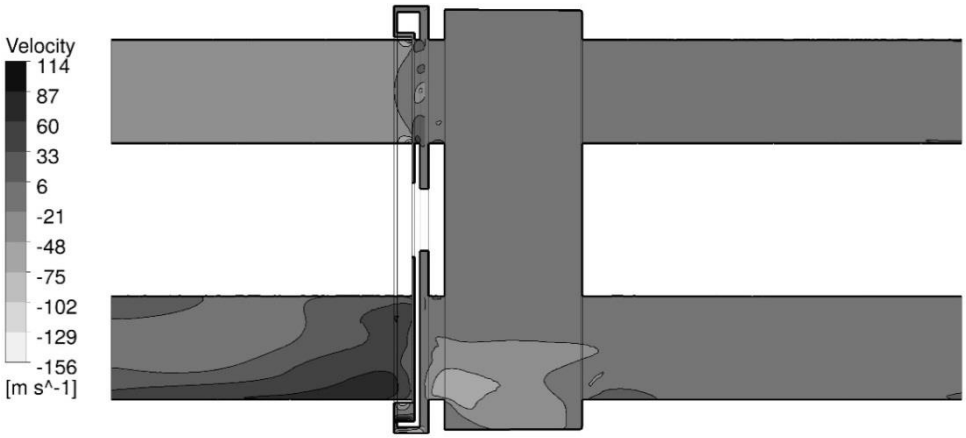


$\phi = 135^{o}$

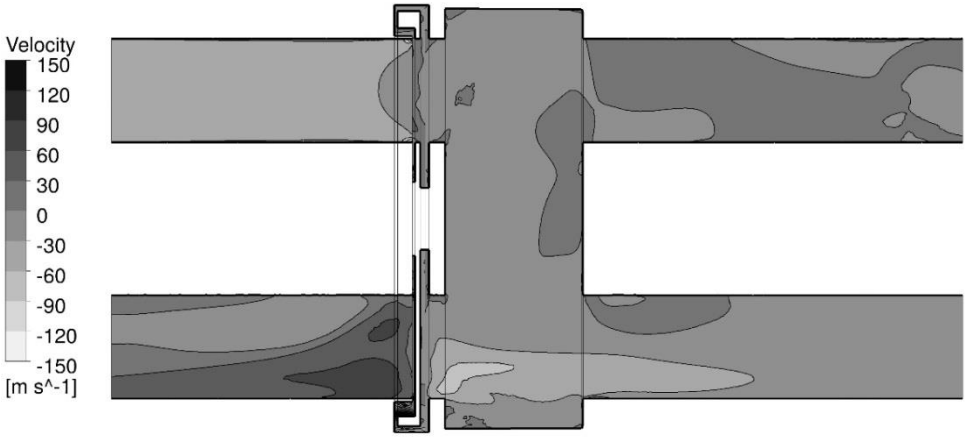


$\phi = 180^{o}$

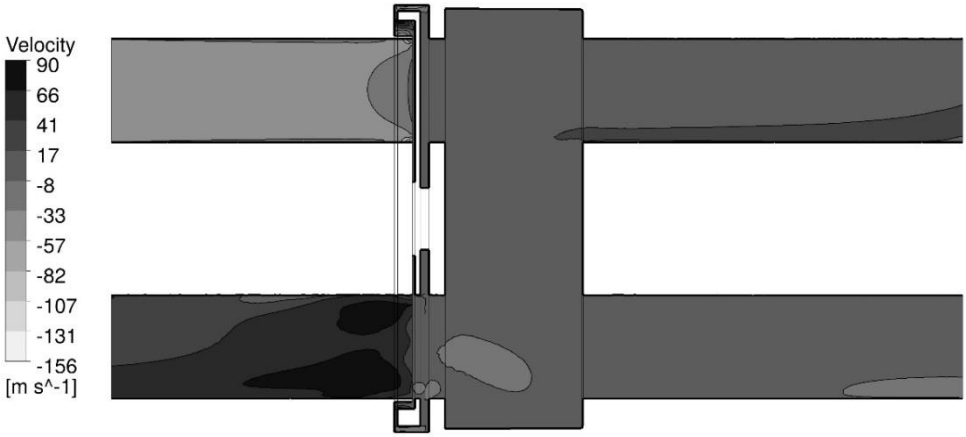


$\phi = 225^{o}$

Fig. 2.20 Velocity distributions for angular positions of the rotating disk equal to $\phi$ = 135, 180, and 225$^{o}$

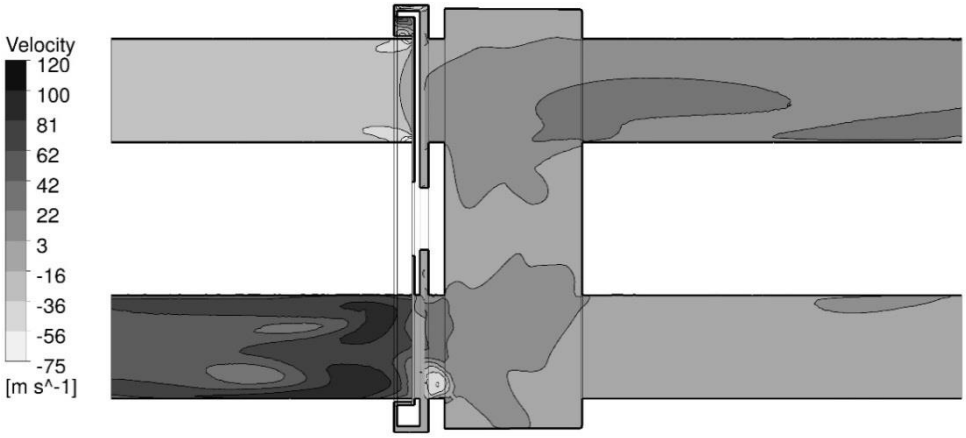


$\phi = 270^{o}$

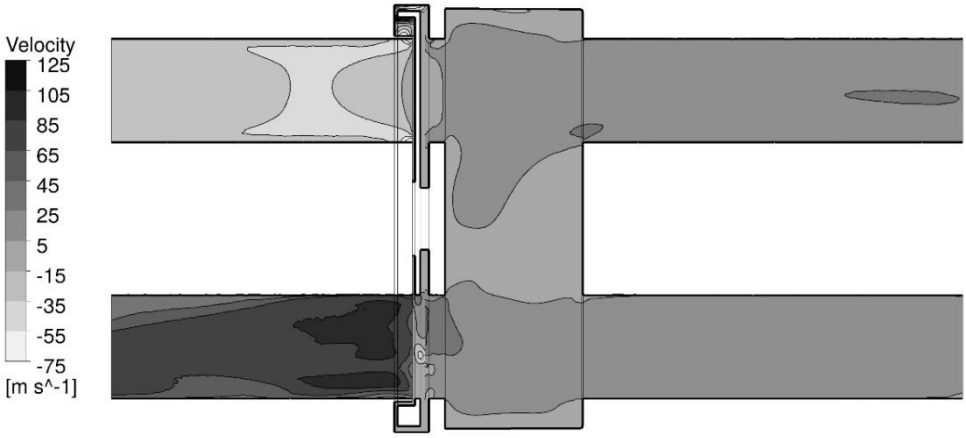


$\phi = 315^{o}$

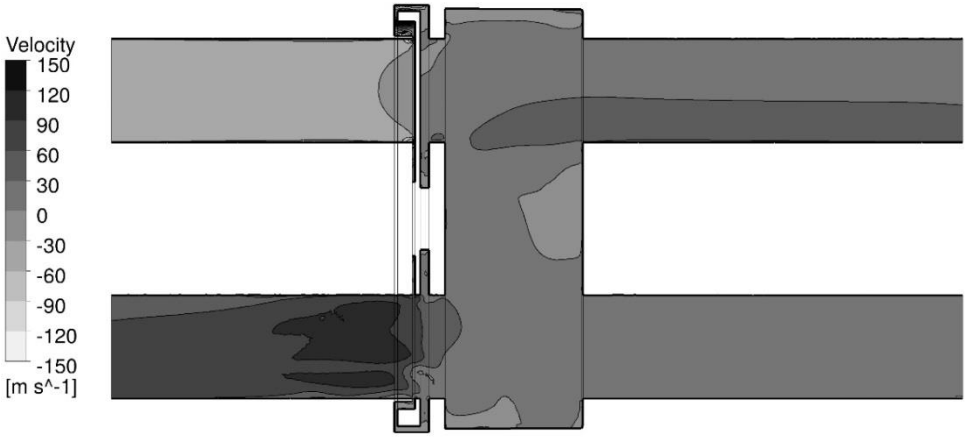


$\phi = 360^{o}$

Fig. 2.21 Velocity distributions for angular positions of the rotating disk equal to $\phi$ = 270, 315, and 360$^{o}$

### 2.5.4 Turbulence Magnitudes

Turbulence is a major factor in determining the nature of fluid flow and also in the generation of sound. These uses have motivated the presentation of turbulence results here. There are a number of parameters that can be used to convey turbulence magnitudes. In choosing a parameter, it is appropriate to select one whose physical meaning is readily understood. In that regard, a viscosity ratio defined as

$$\textit{Viscosity ratio} = \mu_{turb}/\mu \tag{2.10}$$

In this definition, $\mu_{turb}$ is the viscosity due to turbulence, and $\mu$ is the true viscosity of the fluid. If the flow regime is laminar, $\mu_{turb} = 0$. The ratio defined by Eq. (2.10) can be taken as a measure of the strength of the turbulence. Turbulence results for angular positions of the rotating disk equal to $\phi = 0$, 45, and $90^o$ are conveyed in Fig. 2.22. Inspection of this figure shows values of $\mu_{turb}$ that are as large as about 450 times the true viscosity $\mu$. This is clear testimony that strong turbulence exists somewhere in the device. On the other hand, the graytone scales extend to values as low as zero which, if actually achieved, would signify regions of no turbulence. A careful evaluation of the viscosity ratio values at every point in the device revealed that at all points, $\mu_{turb}/\mu \geq 20$. This finding clearly shows that strong turbulence exists at all points in the device that are away from the walls, a not-unexpected outcome in view of the complexity of the flow. The strongest turbulence is seen to exist in the outflow conduit and in the plenum chamber.

Turbulence results for angular positions of the rotating disk of 135, 180, and $225^o$ are presented in Fig. 2.23. These results differ from those of Fig. 2.22 in that larger values are encountered and the zones of highest turbulence now encompass the outflow conduit and the lower of the device--vest conduits. Figure 2.24 continues the turbulence-values presentation to angles of 270, 315, and $360^o$. These show results a diminishing trend in the magnitude of the turbulence as well as a lessening of the concentration of the high-turbulence zones.

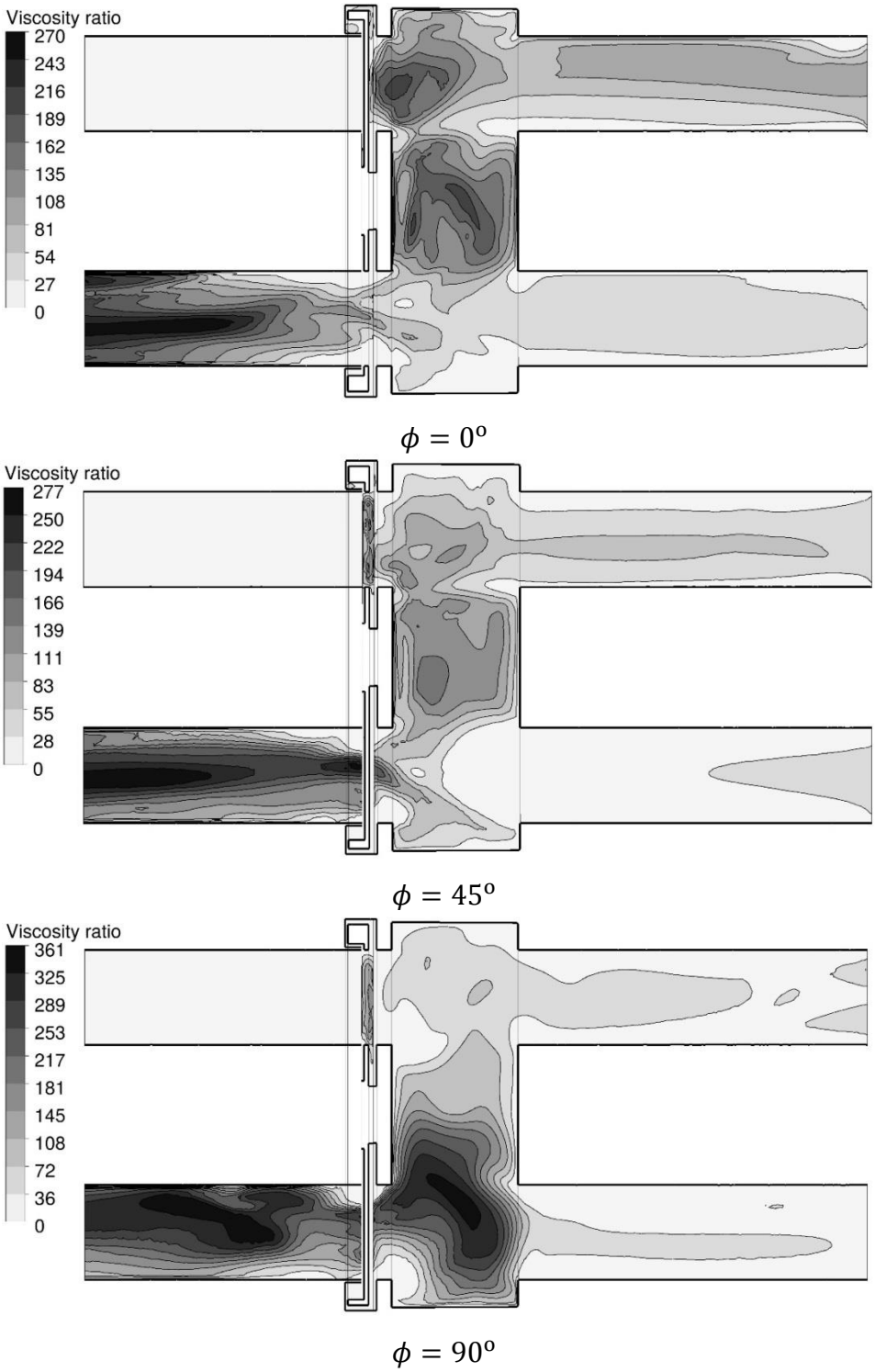


Fig. 2.22 Values of the viscosity ratio $\mu_{turb}/\mu$ for angular positions of the rotating disk equal to $\phi = 0$, 45 and 90º

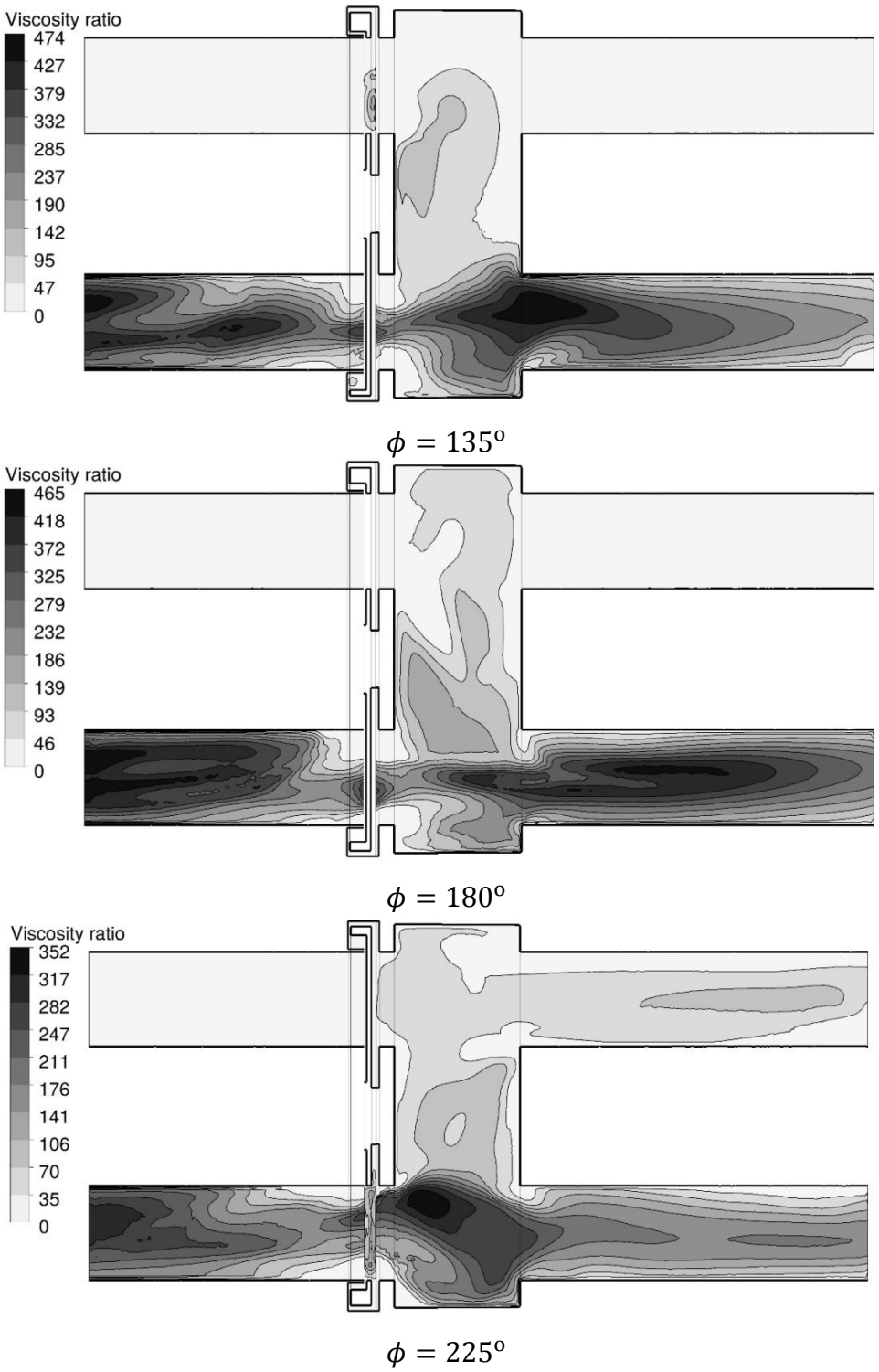


Fig. 2.23 Values of the viscosity ratio $\mu_{turb}/\mu$ for angular positions of the rotating disk equal to $\phi$ = 135, 180 and 225º

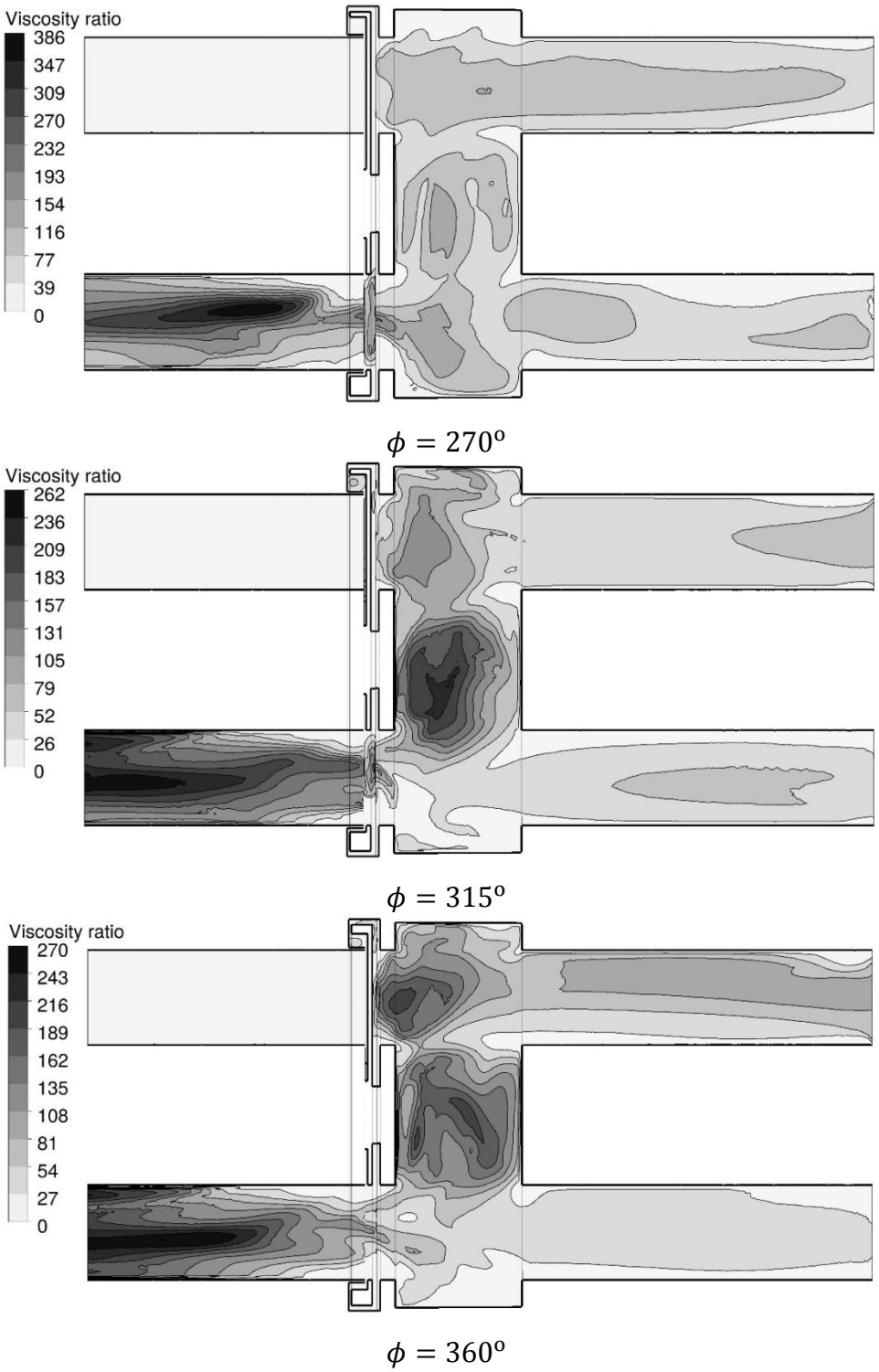


Fig. 2.24 Values of the viscosity ratio $\mu_{turb}/\mu$ for angular positions of the rotating disk equal to $\phi$ = 270, 315, and 360°

### 2.5.5 Sound Power

Sound management is a critical issue for frequently used biomedical therapeutic devices. In view of the relatively high air velocities and turbulence levels displayed earlier, the issue of sound was deemed to be relevant. Here, the focus is on sound power, a quantity which depends on the sound source and not on the location of the sound sensor.

Figure 2.25 displays the distribution of the sound power by overlaying graytone shades on the geometry of the device for angular positions of the rotating disk equal to $\phi = 0$, 45 and $90^o$. For these angular positions, the sound power generation is largely confined to the conduit which conveys air from the device to the ambient, to its feed air, and to the open valve through which air is rushing.

Corresponding results are presented in Fig. 2.26 for the angular positions of 135, 180, and $225^o$. Once again, the fully open valve is the site of largest sound generation but the turbulence in the outflow is another strong source of sound. The air that feeds the outflow conduit is another zone of substantial sound generation. The final figure in this sequence, Fig. 2.27, displays results for the angular positions of 270, 315, and $360^o$. For these cases, the only zones of substantial sound generation are the open valves and the outflow conduit.

A summary graph for sound power results is conveyed by Fig. 2.28. Two sets of sound power results are presented in the figure, both as a function of time. The upper set is the maximum sound power created within the device regardless of location. Not unexpectedly, these value are of substantial magnitude, on the order of 215 db. The lower set is the timewise variation of the volume-averaged sound power whose maximum value is about 25 db. Neither of these values would correspond to the sound pressure experienced by an observed located external to the device.

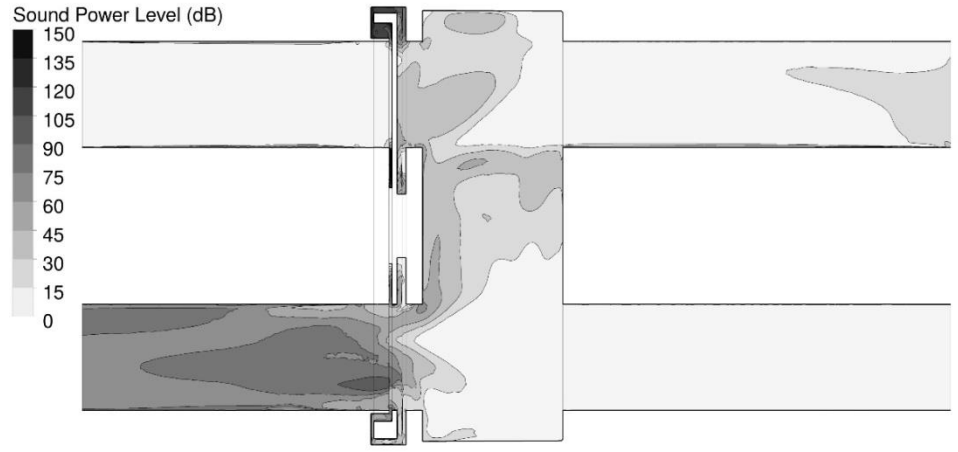


$\phi = 0^o$

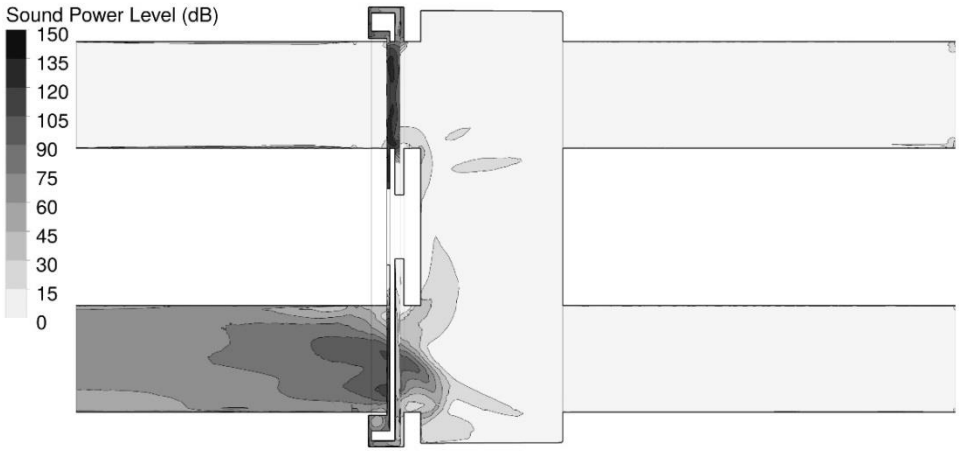


$\phi = 45^o$

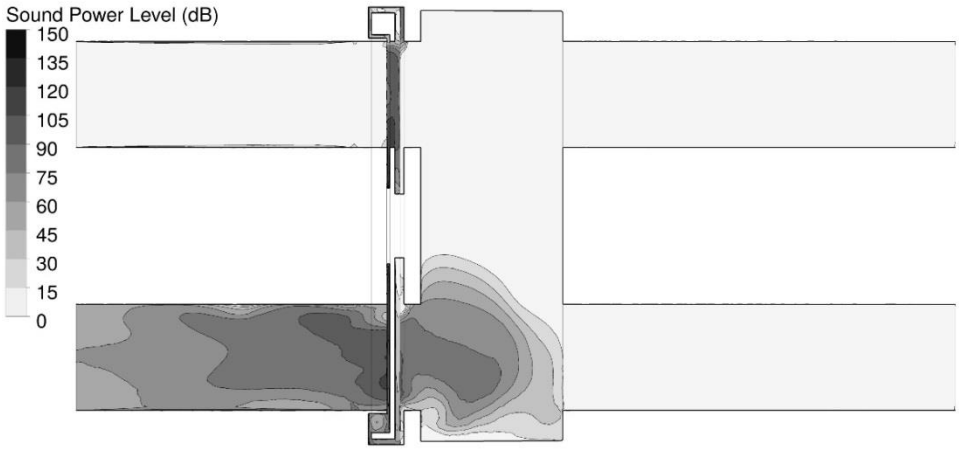


$\phi = 90^o$

Fig. 2.25 Distribution of the sound power for angular positions of the rotating disk equal to $\phi = 0$, 45 and 90º

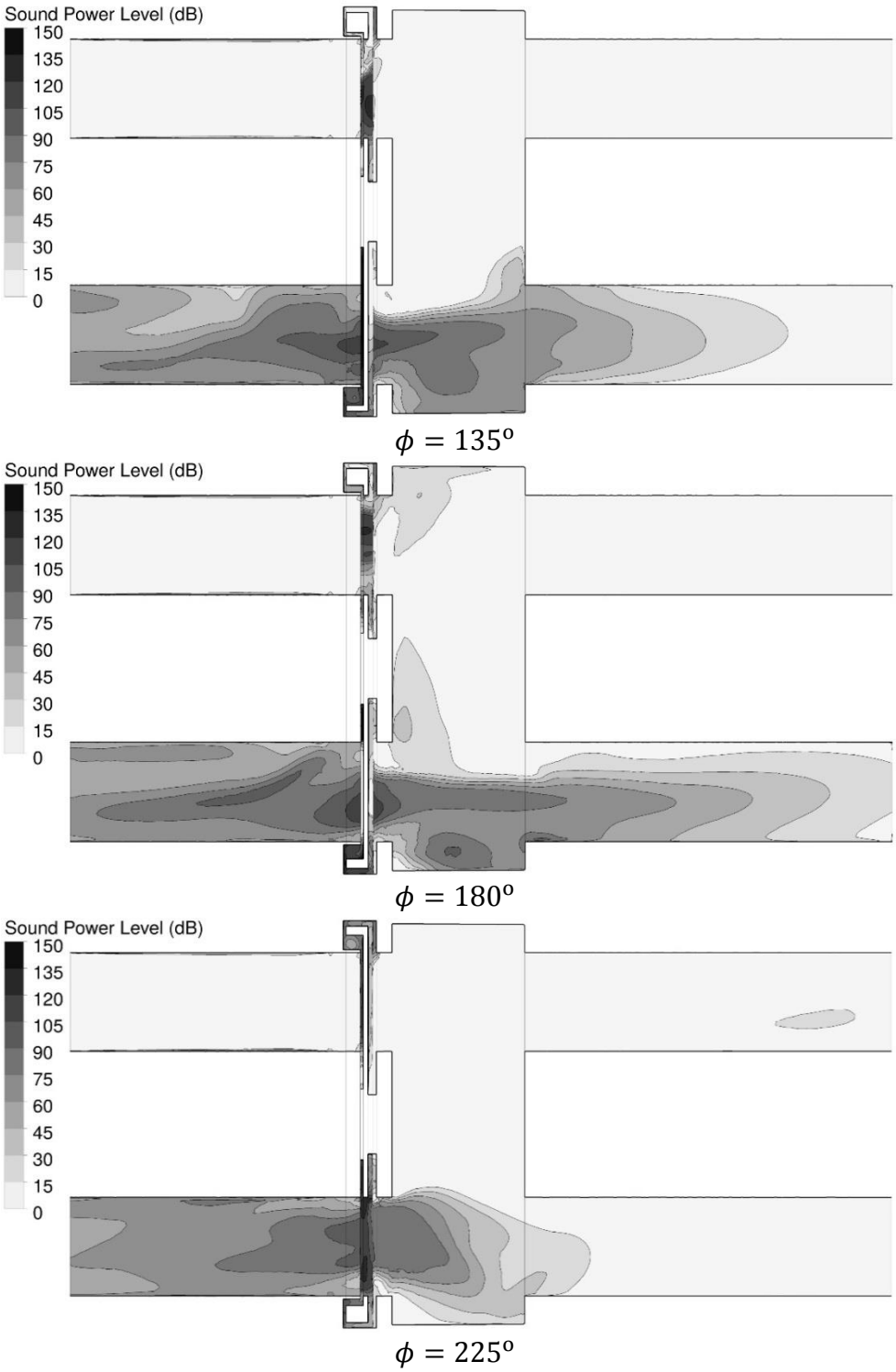


Fig. 2.26 Distribution of the sound power for angular positions of the rotating disk equal to $\phi$ = 135, 180, and 225°

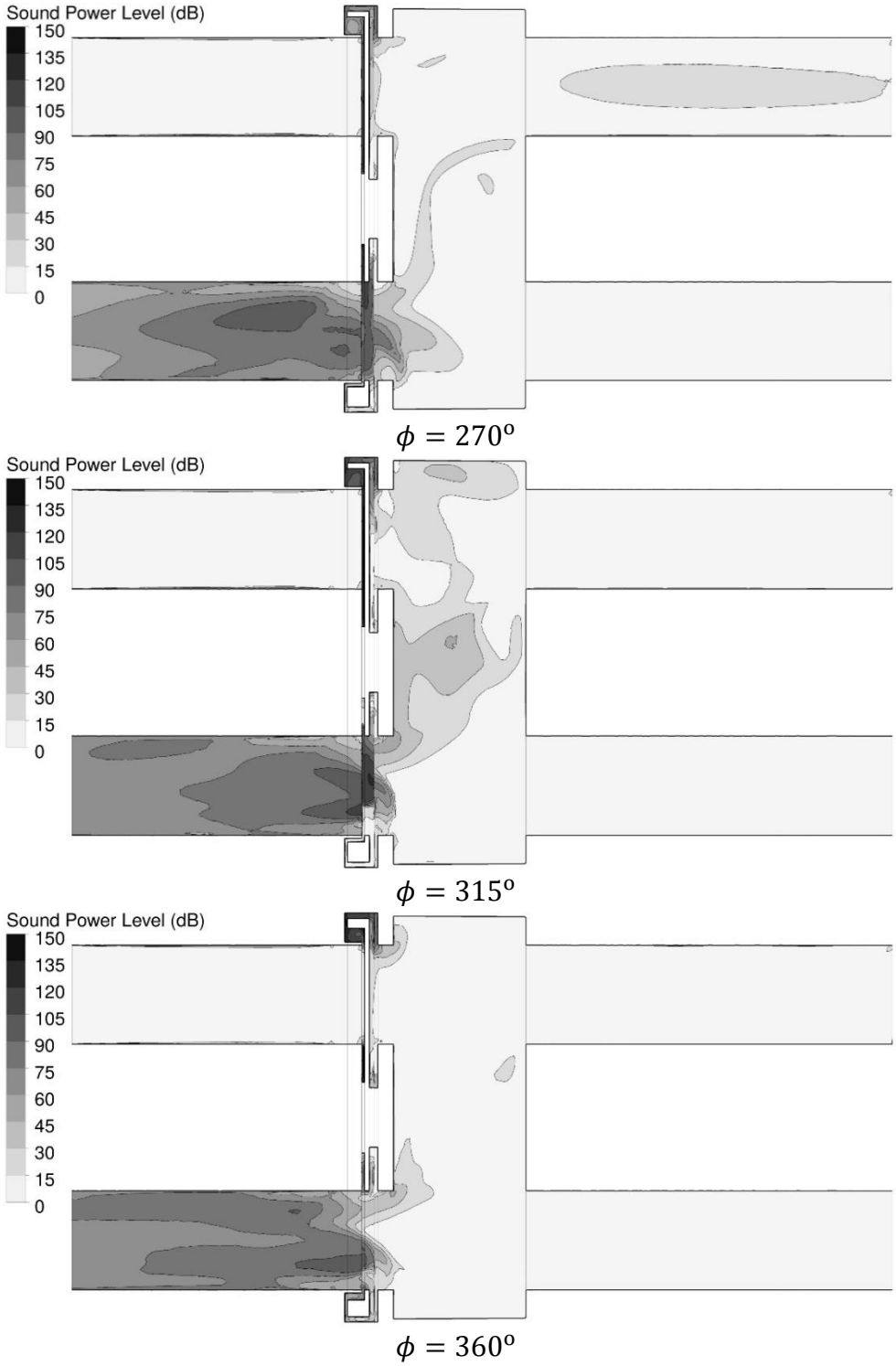


Fig. 2.27 Distribution of the sound power for angular positions of the rotating disk equal to $\phi = 270, 315$, and $360^o$

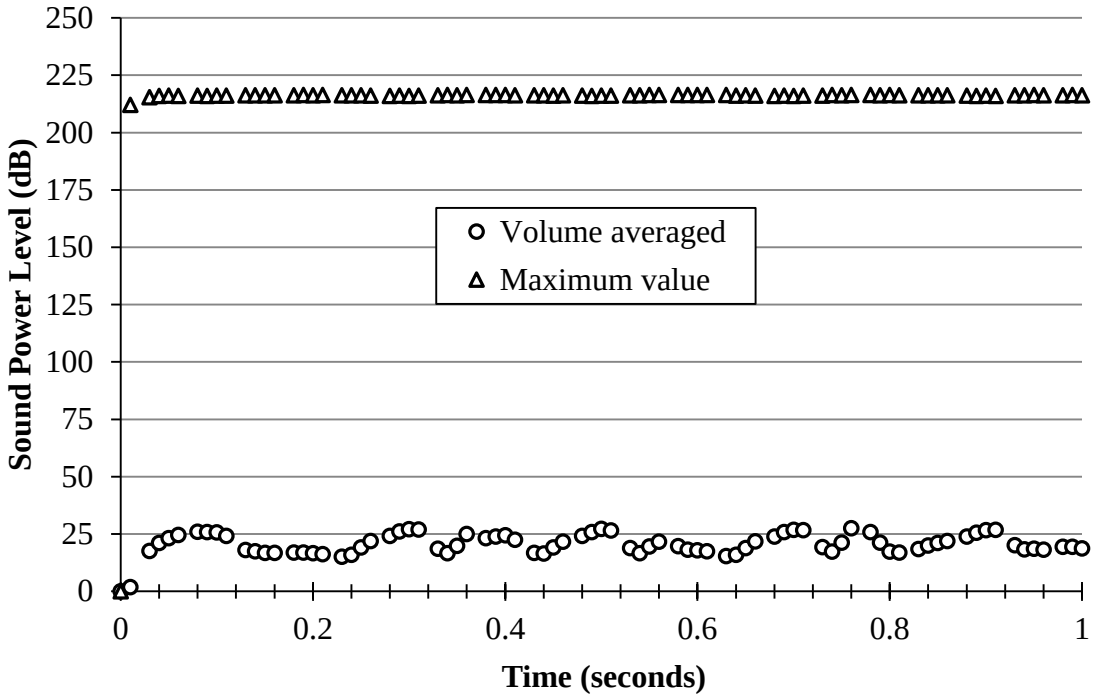


Fig. 2.28 A summary graph for sound power results

## 2.6 CONCLUDING REMARKS

This paper has described a case study which has encompassed both a detailed design approach for a specific biomedical therapy device and a general methodology for advanced design of biomedical therapeutic devices in general. It is believed that biomedical therapeutic devices can be designed to achieve better performance by use of more advanced tools embedded in numerical simulation. The disciplines which can profitably make use of such tools are fluid mechanics, heat transfer, structural analysis, particle transport, sound generation, and interactions of the foregoing. Many of these disciplines participate in the implementation of device-based therapies. Current design approaches are based strongly on intuitive concepts.

The lung-clearance device that was the focus of the specific design task described here strongly involves fluid mechanics and its sound-producing interactions. The key design

tools used here are computational fluid dynamics (CFD) and the theory of sound generated by turbulence. Results provided by the fluid mechanic study included the rates of fluid flow between the device and the inflatable vest, the rates of air supplied to and extracted from the device, the fluid velocity magnitudes and directions that result from the geometry of the device, and the magnitude of the turbulence generated by the fluid motion and the rotating component of the device. Both the velocity magnitudes and the strength of the turbulence contribute to the sound generation.

A marked advantage of the numerical approach is that enables cause and effect to be readily identified. Also, it enables changes and modifications in the geometry of the device to easily correct flaws in the original design.

# Chapter Three

# A MECHANICALLY-DRIVEN PERISTALTIC PUMPING WITH APPLICATION TO THERAPEUTIC DRUG DELIVERY

## 3.1 BACKGROUND

The need for accurate and safe medication delivery and infusion is well documented, and there are many available products that perform the task. These products may pump any variety of drugs, solutions, or even blood into a patient. Due to the wide variety of infusion media and the requirement that any infusion be sterile, standard pumping mechanisms cannot be utilized in practice. The fluid mover that is the focus of this chapter is peristaltic pumping. In its essence, peristaltic pumping is a synergistic interaction of fluid mechanics and structural mechanics [28]. The underlying process of this means of liquid propulsion involves a liquid medium that is contained in a conduit whose walls are flexible [29]. This flexibility property is activated by the imposition of forces which act to reduce the cross section of the conduit [30]. The displacement of fluid-occupied space due to intrusion of the deformed conduit wall provides the impetus for fluid motion.

There are various categories of critical applications for which the sole means of fluid transport is due to peristaltic motions. Within this broadly populated category, there are many applications to biological processes, the most prevalent is the vasomotion of small blood vessels [31-33]. Other major bodily functions which depend on peristaltic pumping include urine transport from the kidneys to the bladder [34,35], movement of ovum in the female fallopian tubes, transport of spermatozoa [36], swallowing food through the esophagus [32,37], the peristaltic reflex of the ileum [38], and chyme motion in the gastrointestinal tract [39]. The aforementioned bodily functions which are fulfilled by peristaltic pumping are driven by muscular wall motions without the presence of mechanical, non-biological intrusions [40]. While the specific mechanisms by which these

processes occur have similarities and differences, the efficiency of fluid propulsion depends on the specifics of the tissue that composes the vessel wall. Furthermore, the flexibility of the tissue depends on age, gender, and somatotype [41]. These mechanisms present interesting areas of future study and will not be discussed in this paper.

In contrast to the foregoing biological applications which are driven by internal bodily processes of contraction, another broad category of peristaltic pumping is based on externally imposed mechanical forces bearing on the external surface of flexible conduits [42]. A small subset involving peristaltic motion derived from chemical reaction was also discovered during the literature review, but will not be the focus of this paper [43]. Common in the mechanical-force category are roller pumps in which cylindrical rods mounted on a revolving frame contact the external surface of the tube in a periodic manner as the frame rotates [44]. Other mechanical means are based on cams and their followers [30].

Mechanical peristaltic pumps are used extensively in the area of drug delivery [45] since the pumping means do not come in contact with the fluid being pumped. Some applications include implantable insulin pumps [46] and the delivery of human milk to premature infants [47]. Limitations posed by other delivery methods, such as the natural barrier properties of the outer layer of skin in topical applications [48], the controlled release and absorption windows of oral ingestion [49], and the risk of dysphagia in oral delivery [50] can be mitigated through the use of a peristaltic pump. Likewise, peristaltic pumps can be utilized on the micro level [51, 52] to create a lab-on-a-chip system [53] or other types of micro-electromechanical systems (MEMS) [54-56]. MEMS devices are increasingly being used to more effectively treat a variety of ailments as noted in [57-59].

For wall-driven fluid motion, the shape of the wall must complement the nature of the mechanical means that create the wall motion and the structural properties of the wall. A number of different means for creating wall-driven flows are utilized in practice, and a very common means, rotation, is exhibited in Fig. 3.1.

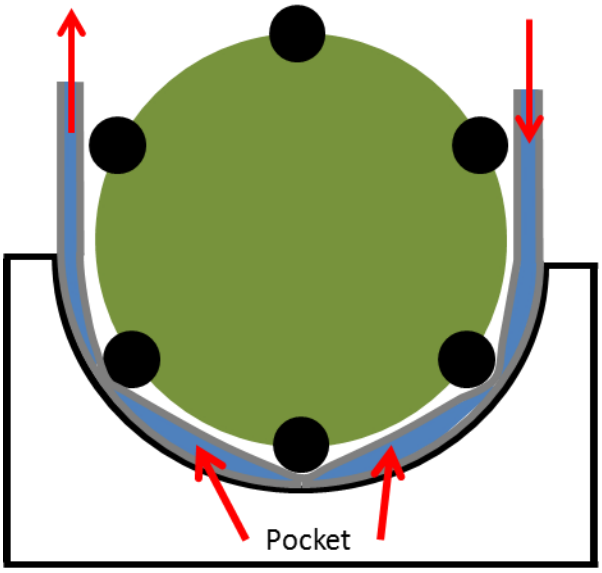


Fig. 3.1 Diagram of a rotating peristaltic pumping mechanism

As can be seen from this figure, a rotating wheel fitted with studs arranged periodically around the circumference creates a spatially periodic indentation in a flexible-walled tube. These indentations trap and move pockets of fluid, resulting in fluid flow.

The pumping mechanism analyzed in this paper is linear peristaltic. An example of an expulsor-type linear peristaltic pump is displayed in Fig. 3.2 (a), (b), and (c). In this case, a fluid pocket is created at the beginning of the cycle by the closure of two valves which fully occlude the tubing. Next, the downstream valve is opened, and the expulsor depresses the fluid pocket which ejects a specific volume of fluid.

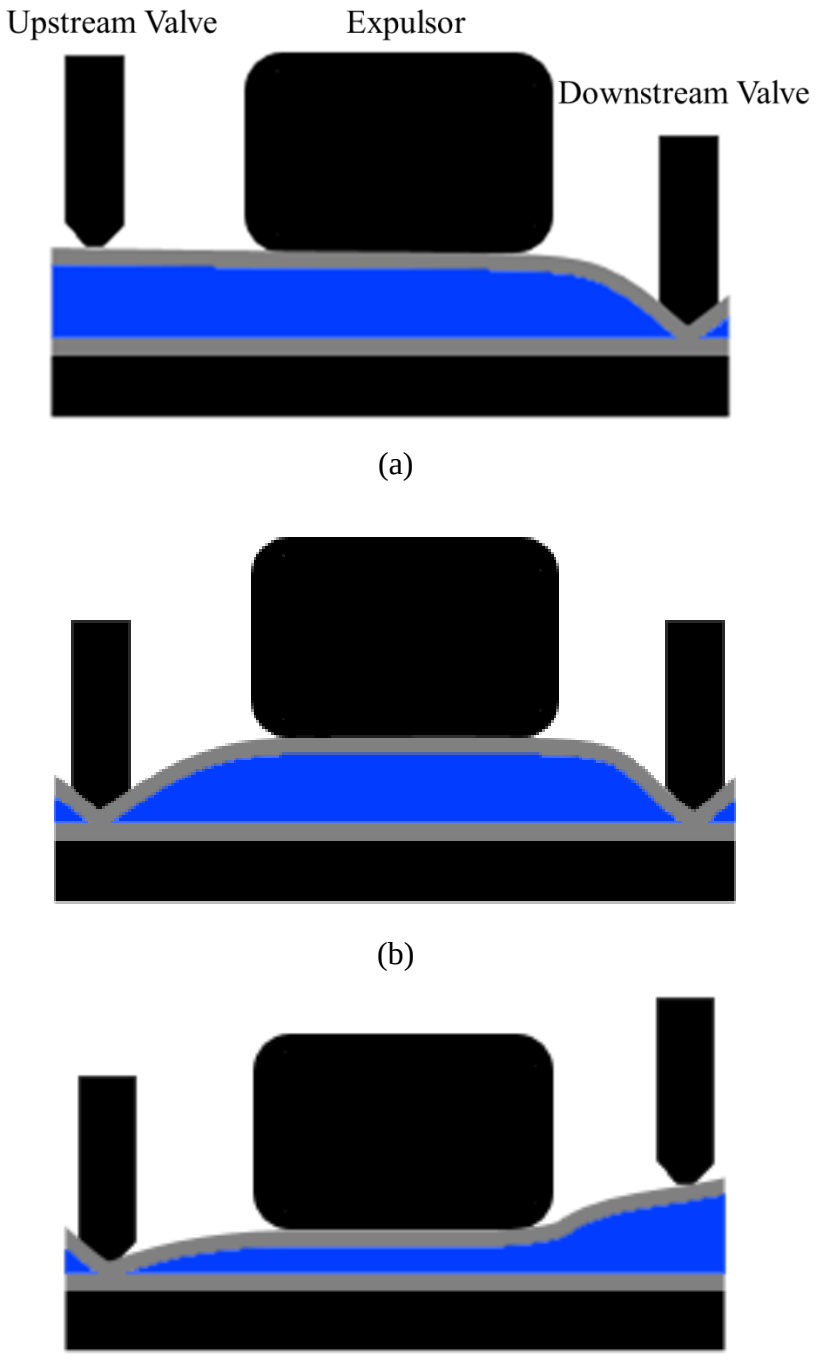


Fig. 3.2 Three stages of an expulsor-type linear peristaltic pumping action: (a) start of expulsion cycle, (b) closing of isolation valves, and (c) expulsion of fluid

The expulsor-type linear peristaltic pump is the mechanism analyzed in this chapter. As mentioned in the foregoing, the precision of this system is of the utmost importance. Previous literature-based analyses have been performed in an attempt to quantify the volume of fluid delivered by each actuation of the expulsor. However, to effectuate these calculations, the deformed cross-sectional shape of the tubing had to be drastically simplified to the highly impractical shape shown in the right part of Fig. 3.3. The results obtained based on this model are likely to depart from real-world outcomes.

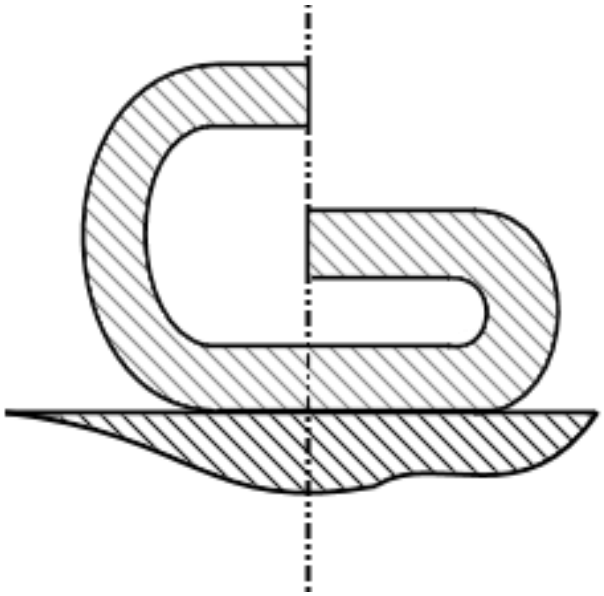

Fig. 3.3 Initial shape (left) and final deformed cross-sectional shape (right) as utilized in conventional expulsor-type linear modeling

While this simplification allowed calculations to be performed, later sections of this chapter will show that this simplification leads to erroneous results. It should be noted that the results of this chapter will primarily illustrate the magnitude of the errors caused by these simplifications and will not capture the full three dimensionality of the fluid delivery problem.

Although the primary focus of this research is to place the design of mechanically-based peristaltic pumps on a firm fundamentals basis, another focus is to demonstrate that

therapeutic biomedical devices involving mechanical features can be designed to a very high standard of efficacy.

## 3.2 PHYSICAL SITUATION

The simulation performed here of the expulsor-type linear peristaltic pumping mechanism is focused on the tube volume directly under the expulsor component. To determine the deformation, a two-dimensional structural model was created as shown schematically in Fig. 3.4. The two-dimensional model was achieved by focusing on a cross section such as that displayed in the figure. This figure shows the tubing in its undeformed initial configuration between two rigid parallel planar surfaces. During the course of the simulation, the surfaces are displaced vertically until the tube reaches its final compressed dimension.

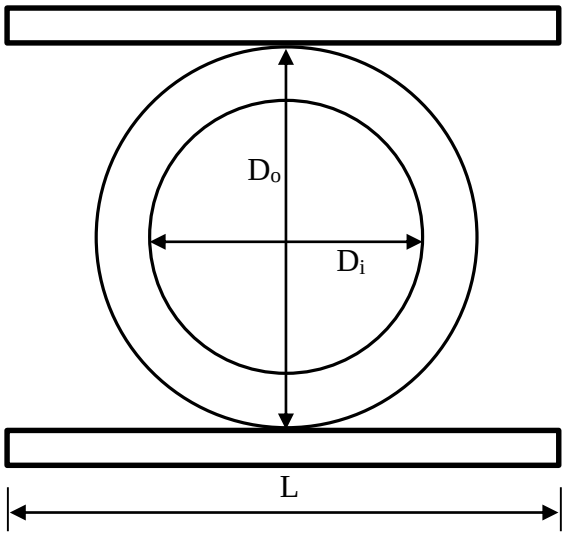


Fig. 3.4 Schematic diagram of the initial configuration of the compressible tubing and the plates used for the compression

## 3.3 STRUCTURAL NUMERICAL SIMULATION

### 3.3.1 Governing Equations

In the model to be employed here, it will be assumed that the resistance to deformation of the tube wall is primarily provided by the structural properties of the tube proper, and that the resistance associated with the fluid is of secondary importance. Such a model corresponds to the limiting case in which the resistance to fluid flow in the tubing is moderate. This model enables the structural analysis to be performed without any reference to the fluid.

The tubing is envisioned as being fabricated from a rubber-like hyperelastic material. As a consequence, the structural analysis has to be carefully tailored. There are a number of models in the literature that were formulated to deal with hyperelastic media. Here, the Ogden model [60] was chosen because it is capable of dealing with strains as large as 700%.

The starting point of that model is the equation for strain energy *W*, which is

$$W = \sum_{i=1}^{n} \frac{2\mu_i}{{\alpha_i}^2} \left(\lambda_1^{\alpha_i} + \lambda_2^{\alpha_i} + \lambda_3^{\alpha_i} - 3\right) + \sum_{i=1}^{n} \frac{1}{d_i} (J_{el} - 1)^{2i} \tag{3.1}$$

where $\lambda_1$, $\lambda_2$, and $\lambda_3$ are the stretch ratios in the three principle directions, $J_{el}$ is the elastic volume ratio (ratio of instantaneous to undeformed volume), and $\mu_i$, $\alpha_i$, and $d_i$ are fitted material constants. Most rubbers strongly resist volume changes, and researches have often approximated the medium as perfectly incompressible ($J_{el} = 1$). For rubber analyzed here, the constants $\mu_i$, $\alpha_i$, and $d_i$ are listed in Table 3.1.

Table 3.1 Material properties for the flexible rubber tube material [61]

| Property | Value |
|---|---|
| Density | 1000 kg/m$^3$ |
| **Ogden 3rd Order Constants** | |
| $\mu_1$ | 6.1803×10$^5$ Pa |
| $\mu_2$ | 1180 Pa |
| $\mu_3$ | -9810 Pa |
| $\alpha_1$ | 1.3 |
| $\alpha_2$ | 5 |
| $\alpha_3$ | -2 |
| $d_1$ | 4.8×10$^{-9}$ Pa$^{-1}$ |
| $d_2$ | 0 |
| $d_3$ | 0 |

From the Ogden material model, the three principal values of the Cauchy stresses can now be determined from

$$\sigma_i = z_i \frac{\partial W}{\partial \lambda_i} \tag{3.2}$$

where

$$z_i = \frac{\lambda_i}{\lambda_1 \lambda_2 \lambda_3} \tag{3.3}$$

Furthermore, the non-principle stresses $\sigma_{ij}$ are

$$\sigma_{ij} = \sum_{k=1}^{3} z_k \frac{\partial W}{\partial \lambda_k} b_i^{(k)} b_j^{(k)} \tag{3.4}$$

With respect to $b_1$, $b_2$, and $b_3$, they are mutually perpendicular unit eigenvectors of the left Cauchy-Green deformation tensor **B** which define the principal stretch directions [60]. The values of $\lambda_1$, $\lambda_2$, and $\lambda_3$ are respectively equal to the square root of the eigenvalues of the left Cauchy-Green tensor **B.**

### 3.3.2 Boundary Conditions

The initial condition corresponded to a stress-free, totally undeformed circular cross section with an annulus wall of uniform thickness. Correspondingly, both the initial displacement and the initial stresses are zero. At times $t > 0$, the upper and lower expulsor plates were set into motion at the rate of 1.85 mm/s. A graph conveyed in Fig. 3.5 illustrates the timewise motion of the expulsor plates. This action was continued until a predetermined maximum displacement of the plates was achieved.

The boundary conditions on the expulsor plates included surface displacements in the vertical direction. At those parts of the tube surface that are in contact with the expulsor plates, the instantaneous position of the surface is equal to that of the plates. In contrast, those parts of the tube surface that are not in contact with the plates are free to move in any direction in the plane of the cross section, but no motion is allowed in the axial direction nor is rotation permitted. With regard to the internal surface of the tube, there is no resistance so that in-plane motion can occur without constraint. Here again, neither axial motion nor rotation is permitted.

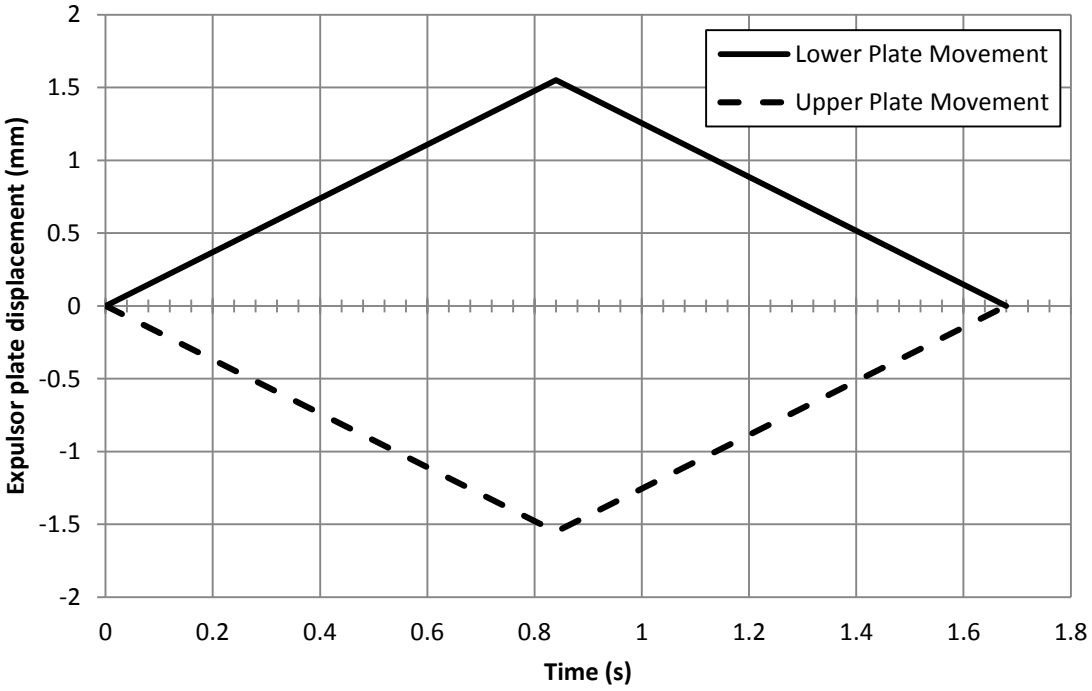

Fig. 3.5 Timewise motion of the expulsor plate and symmetry plate. Zero displacement represents the starting location

The governing equations along with the initial and boundary conditions were solved by means of ANSYS 15.0 finite-element software. This software enabled discretization of the equations, and the discretized expulsor plate and flexible tubing in the undeformed state are displayed in Fig. 3.6. The total number of nodes constituting the two-dimensional discretized space was 231,400.

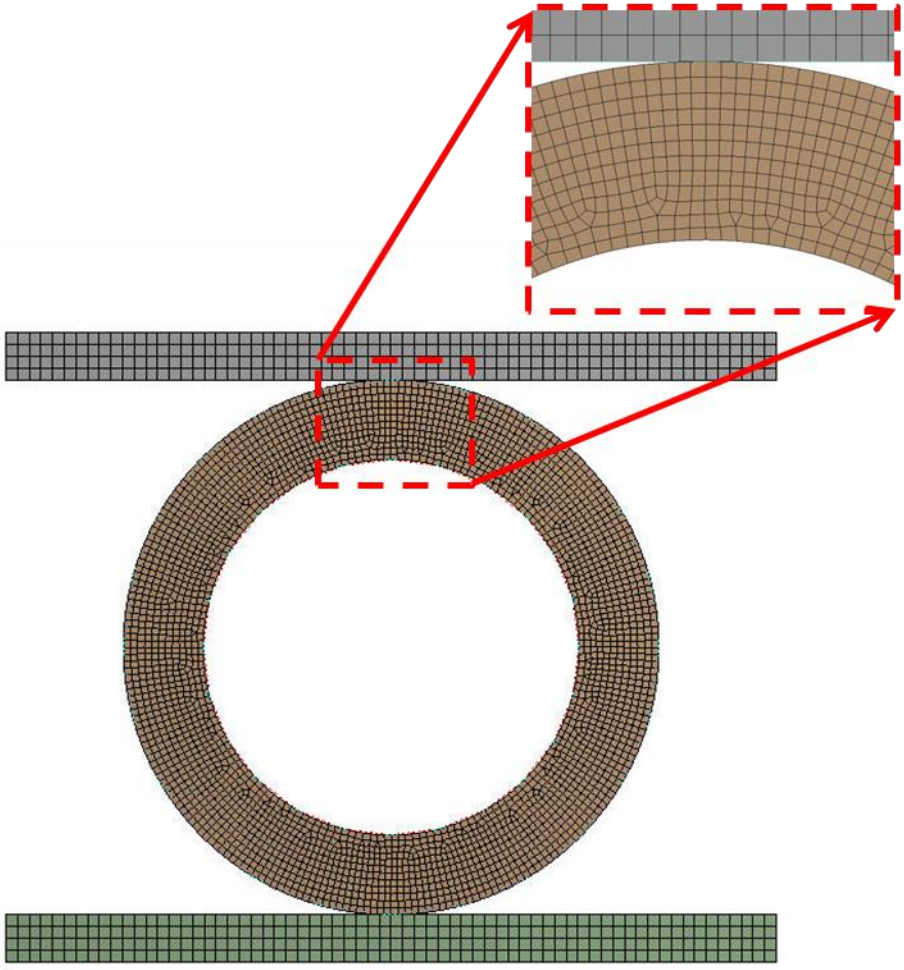

Fig. 3.6 Display of the discretized solution space in the undeformed state

**3.4 RESULTS AND DISCUSSION**

### 3.4.1 Fluid Mechanic Results

The first result to be presented is the rate at which fluid is pumped by the peristaltic action. To obtain this result, it is relevant to keep track of the volume that is enclosed in the bore of the flexible tubing. The change of that volume is equal to the volumetric fluid flow that is produced. The variation of the enclosed volume with time is displayed in Fig. 3.7. On the vertical axis of the figure, the ratio of the instantaneous volume *V(t)* to the initial undeformed volume *V(0)* is plotted. The abscissa is the time starting with the undeformed state at t = 0 s. The heavy continuous line in the figure is taken directly from the numerical simulations. In addition, there are curve fits corresponding to polynomials of degrees 1 through 4. The equations for these curve fits are indicated in the figure along with the $R^2$ values which convey the quality of the fit. It is seen from these equations and the fit indices that the third and fourth degree polynomials are perfect fits. The figure shows that the volume of the bore decreases monotonically with time, as expected.

$$y = 1.8174x^3 - 2.103x^2 - 0.8308x + 1, R^2 = 0.9999$$

$$y = 2.5837x^4 - 1.064x^3 - 1.1237x^2 - 0.9279x + 1, R^2 = 1$$

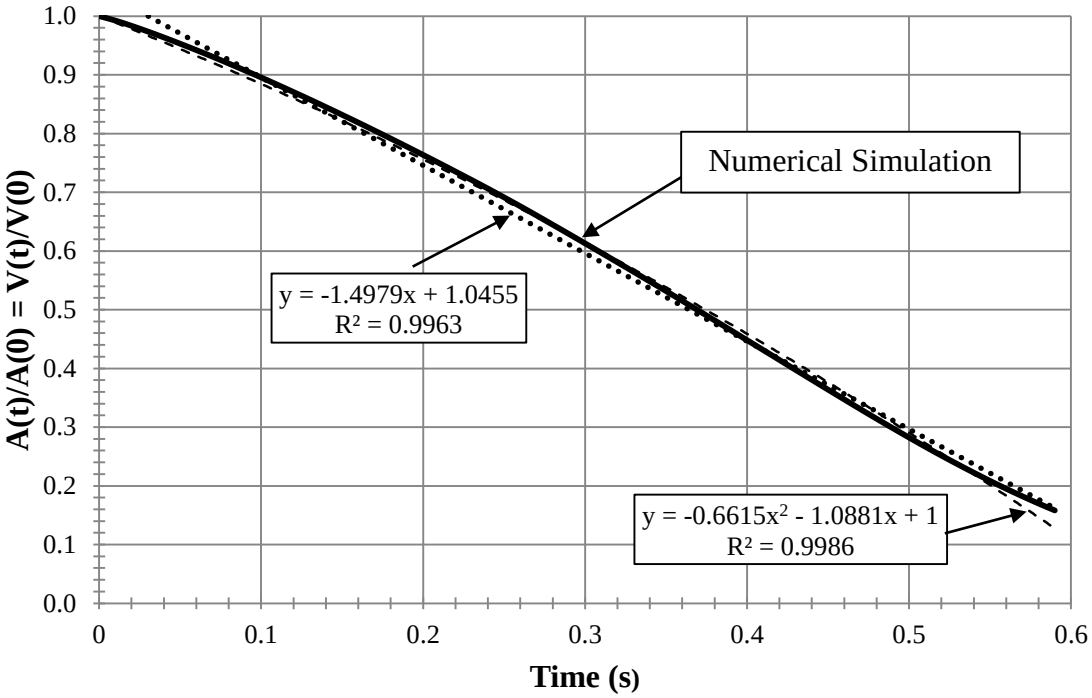


Fig. 3.7 Timewise variation of the volume of the bore in ratio form, where *V(t)* denotes the instantaneous volume and *V(0)* is the initial undeformed volume

The rate at which fluid is expulsed is given by

$$Q = \frac{dV(t)}{dt} \tag{3.5}$$

By means of this equation, the resulting volumetric flow rates have been calculated and are plotted in Fig. 3.8. That figure contains five candidate results. The first of these is a direct numerical differentiation of the simulation results, with the deviation from smoothness being attributable to the numerical differentiation. The other curves respectively correspond to the four polynomial fits that were set forth in Fig. 3.7, with each number attached to a curve denoting the degree of the polynomial.

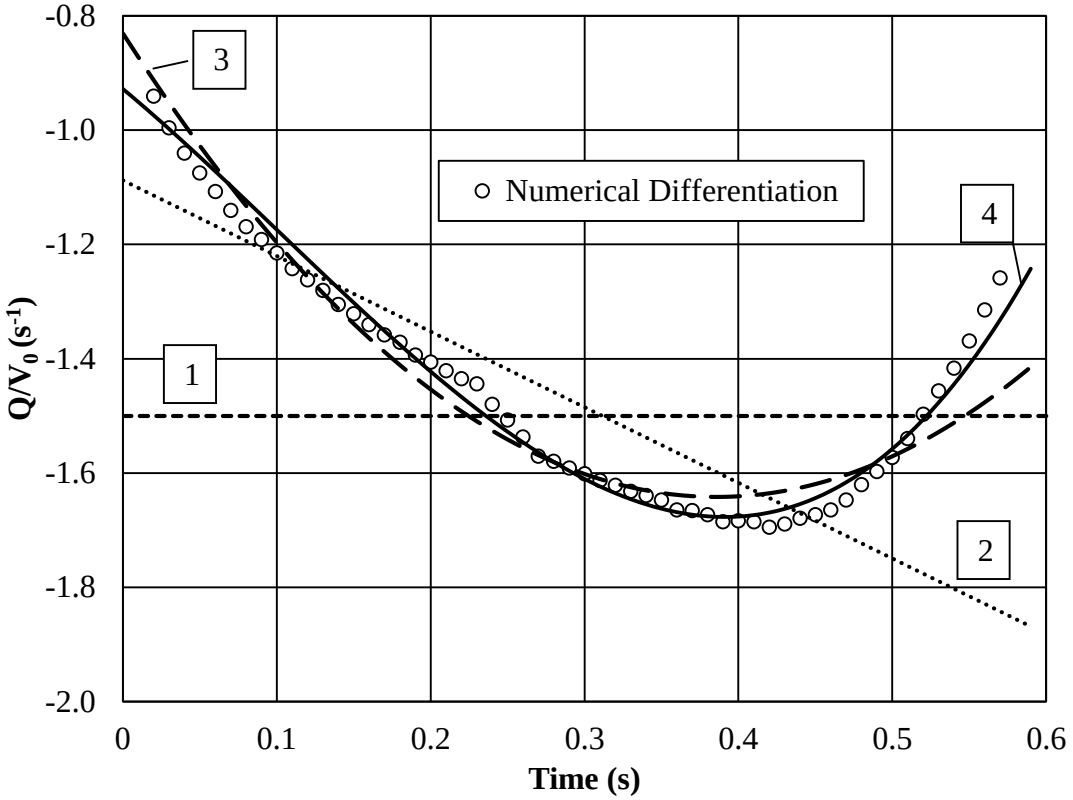


Fig. 3.8 Volumetric fluid flow rates resulting from the peristaltic action. Each number attached to a curve denoting the degree of the polynomial

It can be seen from the figure that the curve representing the fourth degree polynomial is an excellent fit to the numerical simulation results. The algebraic equation from which the volumetric flow results can be readily obtained is

$$\frac{Q}{V(0)} = 10.34t^3 - 3.19t^2 - 2.25t - 0.928 \quad (3.6)$$

In this equation, $Q$ is the volumetric flow rate in $m^3/s$, $V(0)$ is the undeformed volume in $m^3$, and $t$ is the time in seconds.

### 3.4.2 Mechanical (Structural) Results

The next result is the force per unit axial length required to compress the tubing at a constant rate. This information is conveyed in Fig. 3.9 as a function of time. The figure shows, as expected, that the force increases as time passes, indicating a spring-like response.

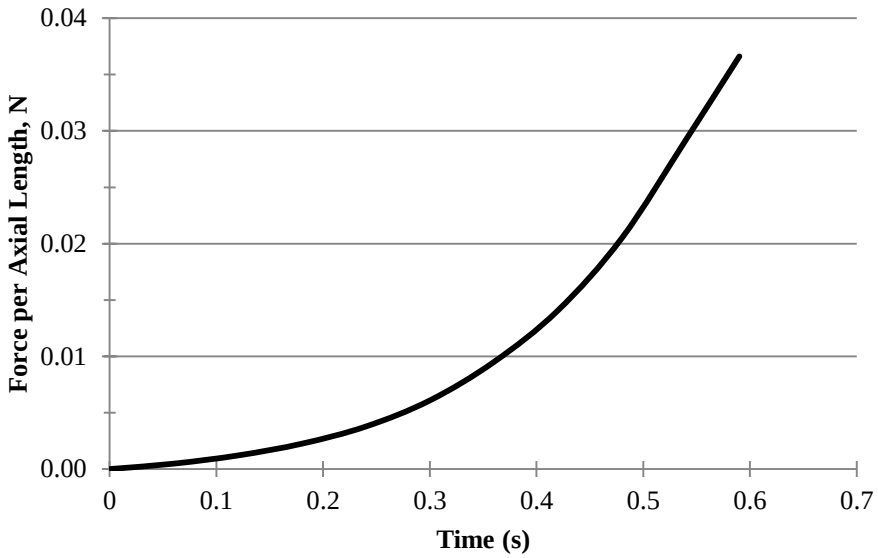


Fig. 3.9 Force per unit axial length required to compress the tubing uniformly with time

A display of the constant rate of decrease of the inter-plate spacing is provided in the left-hand diagram of Fig. 3.10. It is this rate that the force already displayed in Fig. 3.9 has provided. In the right-hand diagram of Fig. 3.10, a notation-laden diagram is shown as a prelude to results to be exhibited in Fig. 3.11. This figure shows the change of thickness of the tube wall at selected locations. In particular, those locations are the midway points of both the top and bottom walls and of the two side walls of the tube. From Fig. 3.11, it can be seen that the compression of the top and bottom walls is greater than that of the side walls during the initial time period. On the other hand, the side walls are less constrained than are the top and bottom walls, and it is this factor that enables the compression of the former to be greater at larger values of time.

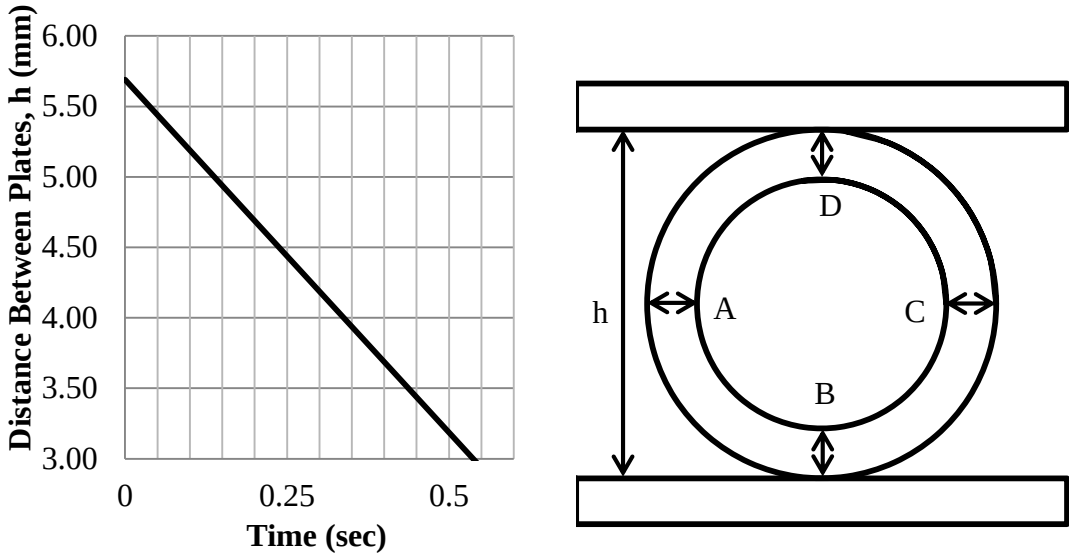


Fig. 3.10 At left: rate of decrease of the inter-plate space *h* and at right: notation

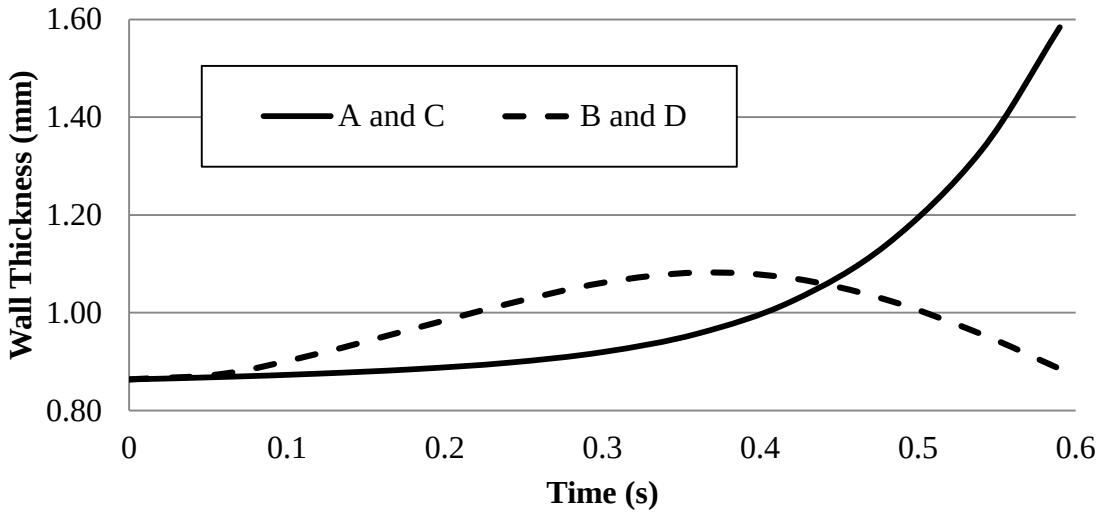


Fig. 3.11 Variations of the wall thickness of the compressed tube at selected circumferential locations

The next group of figures conveys information about the distribution of the effective (von Mises) stresses. This information is presented at time intervals of 0.06 seconds up to the

termination of the compression of the tube. The units of stress are MPa. An overview of the figures ranging from $t$ = 0.06 to 0.59 s shows that the largest stresses are confined to regions immediately adjacent to the bore of the tube and the vertical axis. At the early times, these high-stress regions tend to be confined to the near neighborhood of the vertical axis. As time advances, these regions tend to moderately broaden but continue to flank the vertical axis of the tube. Aside from the aforementioned regions, there are large expanses of low stresses that are located adjacent to the compression plates as well as at the lateral ends of the tube. The passing of time reveals a monotonic increase of the maximum stress starting with a value 0.18 MPa at $t$ = 0.06 s to a value of 8.1 MPa at $t$ = 0.59 s.

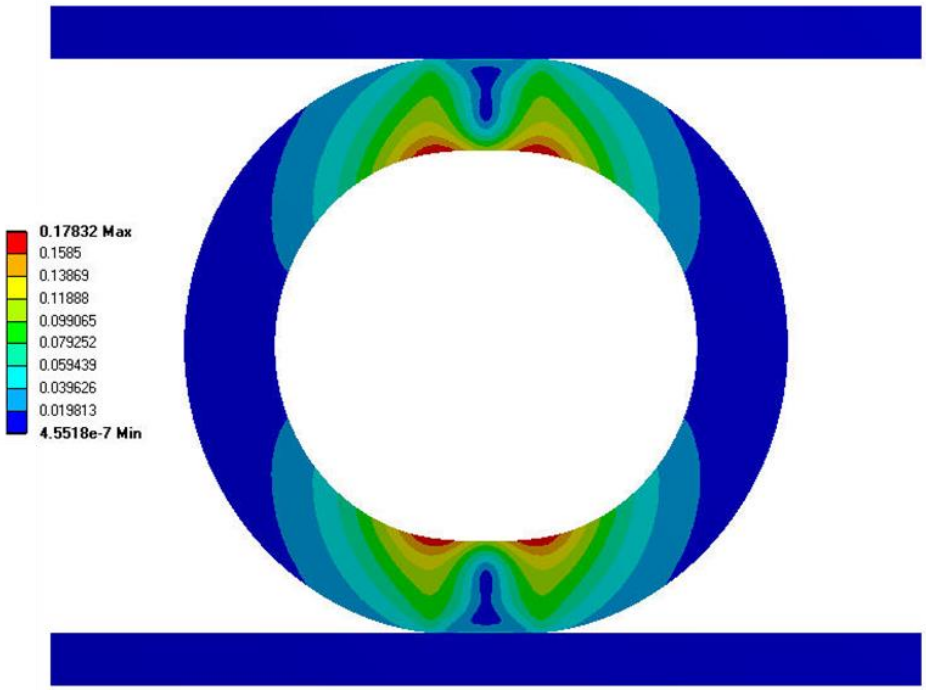


(a) t = 0.06 s

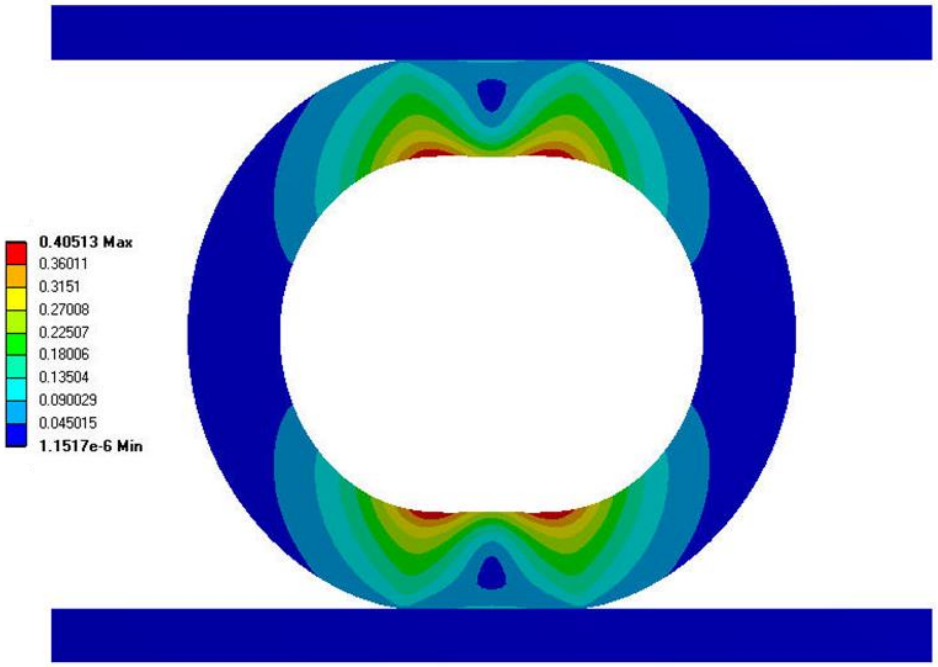


(b) t = 0.12 s

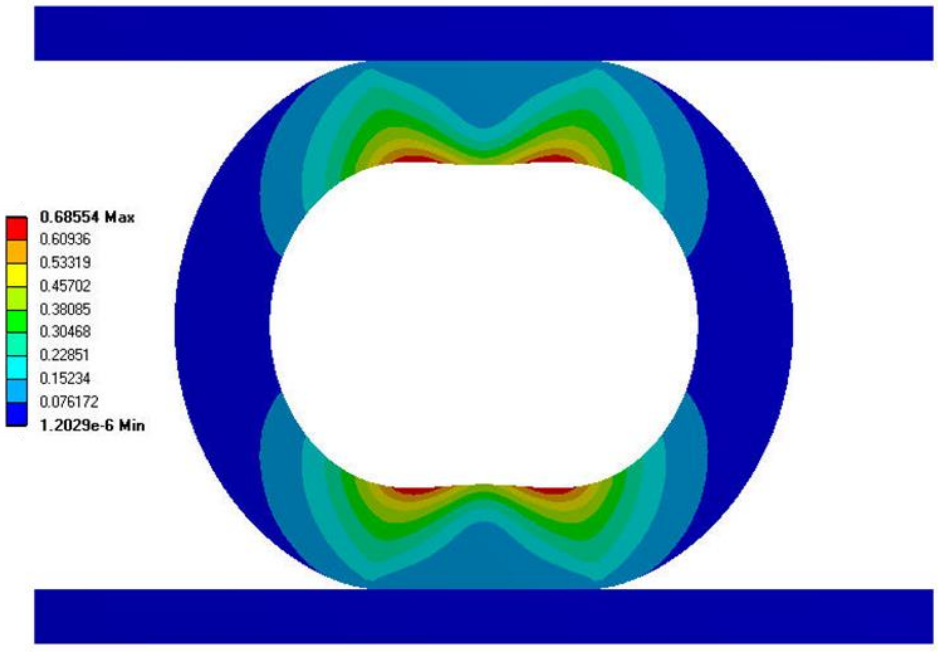


(c) t = 0.18 s

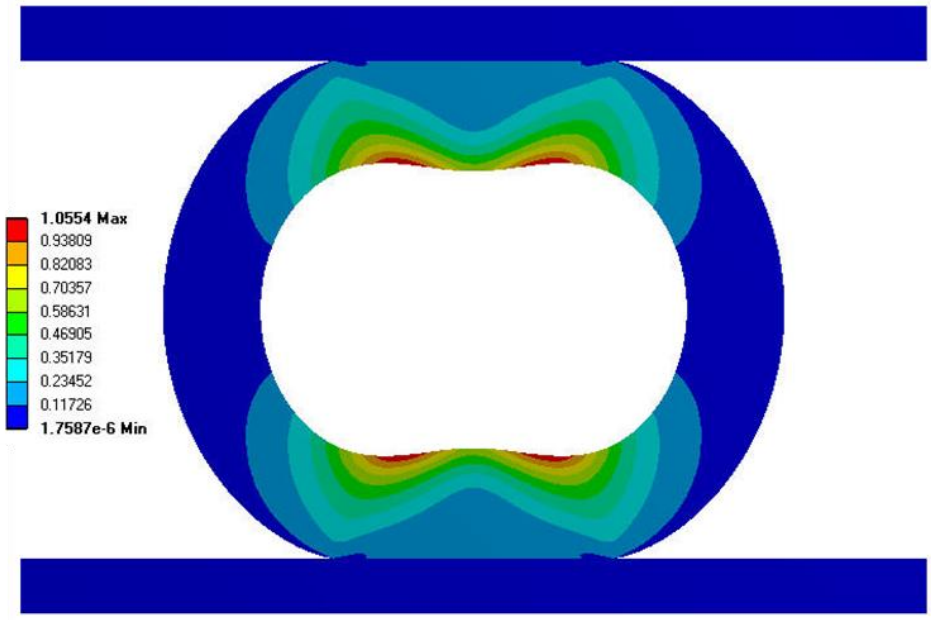


(d) t = 0.24 s

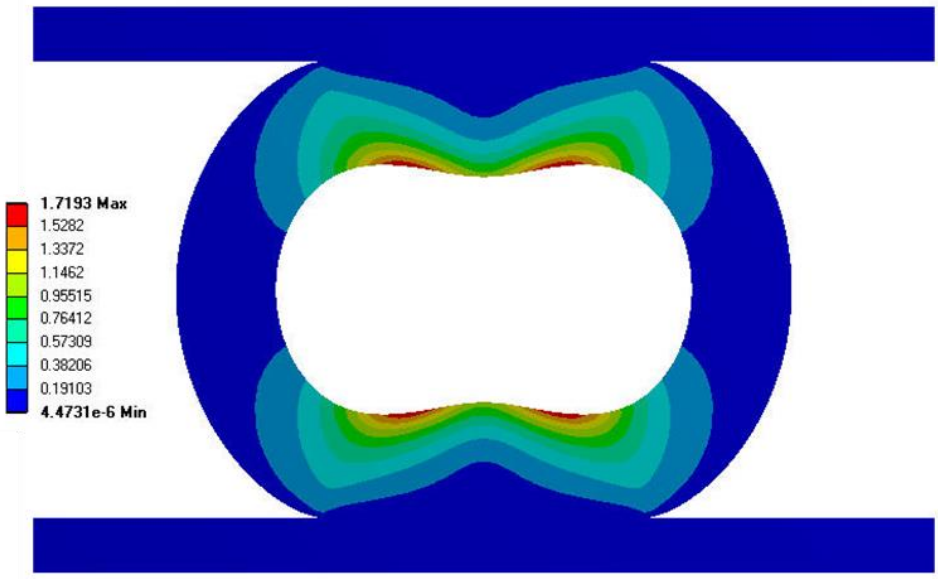


(e) t = 0.30 s

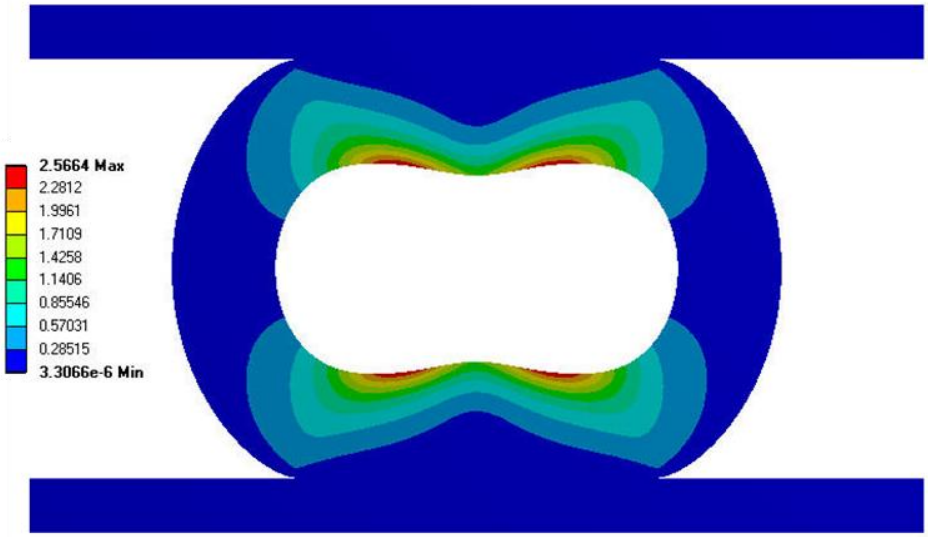


(f) t = 0.36 s

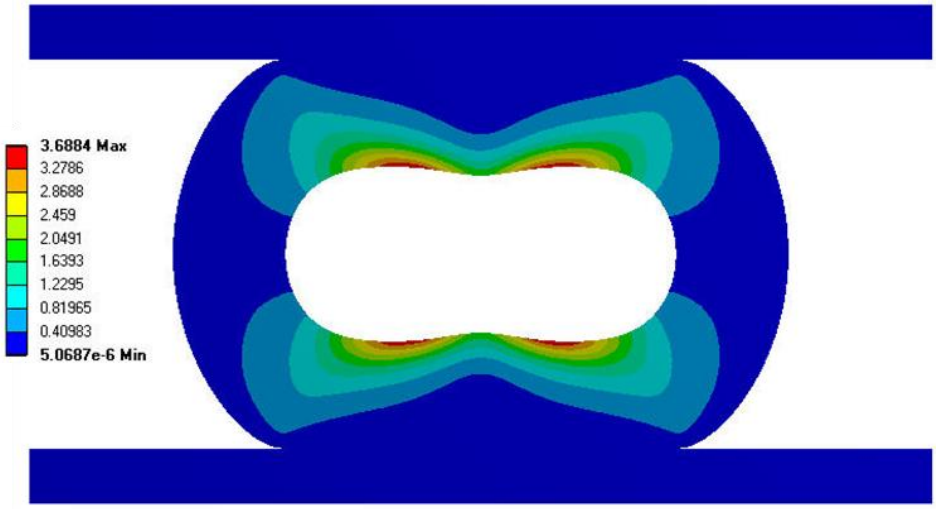


(g) t = 0.42 s

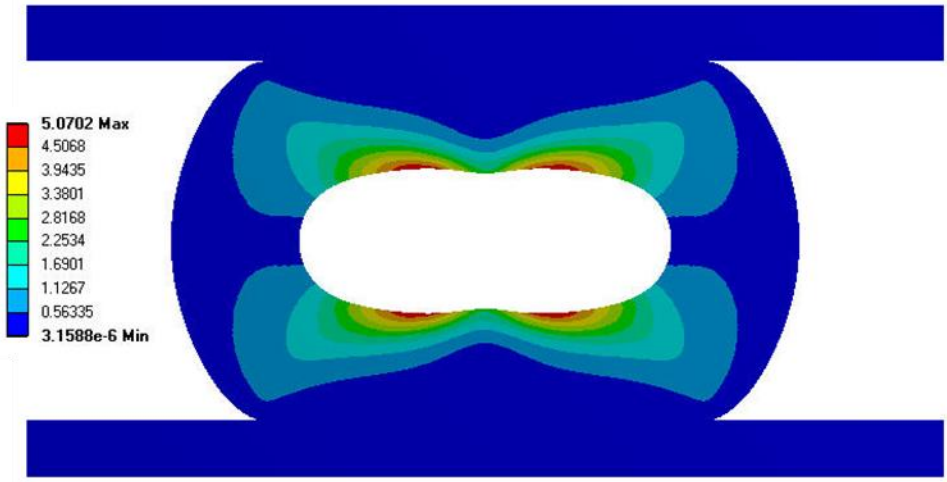


(h) t = 0.48 s

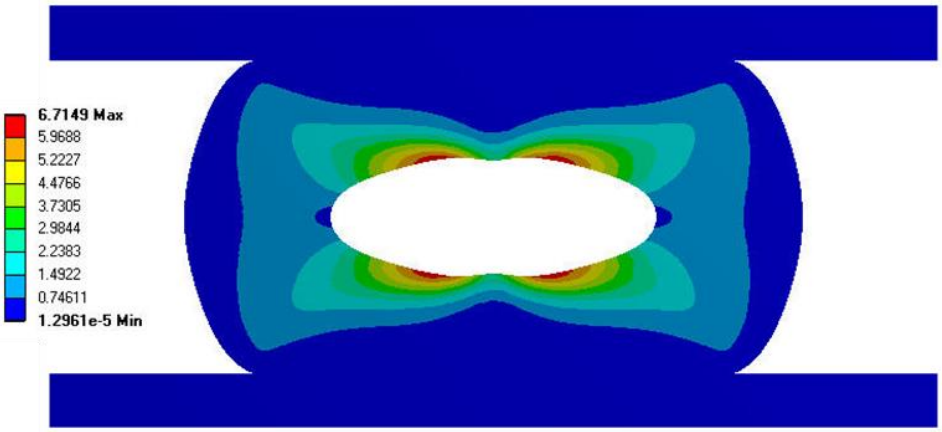


(i) t = 0.54 s

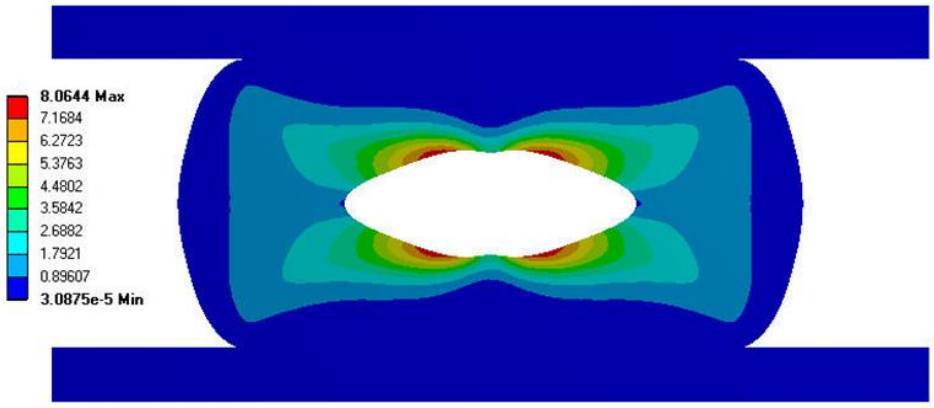


(j) t = 0.59 s

Fig. 3.12 Distributions of the effective (von Mises) stress at 0.06 second intervals throughout the peristaltic compression cycle. The stresses are in units of MPa.

As a complement to the foregoing presentation of stress results, a corresponding set of deflection results will now be presented. The information will be conveyed in Fig. 3.13, parts (a) through (j), for times ranging from 0.06 to 0.59 s. Over this range, the maximum deflections increase from 0.16 to 1.5 mm. For all of the deflection results, the units are mm.

Inspection of Fig. 3.13 shows that the deflections are symmetric with respect to the vertical axis of the tube. At any of the early times, the deflections are concentrated in the near neighborhood of the vertical axis and at the tube bore. With the passing of time, the deflections spread laterally, but the highest deflections continue to be confined to the aforementioned neighborhood. Only near the termination of the compression cycle, at t = 0.54 s, does the high deflection region include the outer wall as well as the bore -facing wall of the tube. Even at the conclusion of the compression cycle, a pocket of small deflections persists at the outboard ends of the flattened tube.

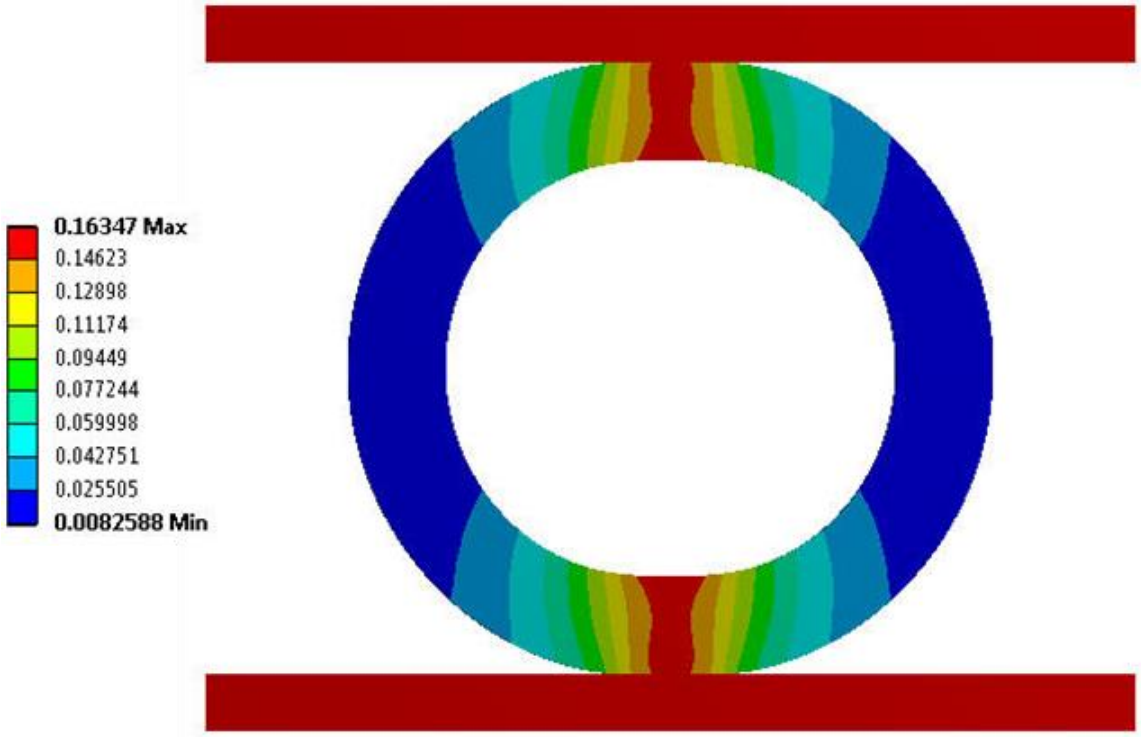


(a) t = 0.06 s

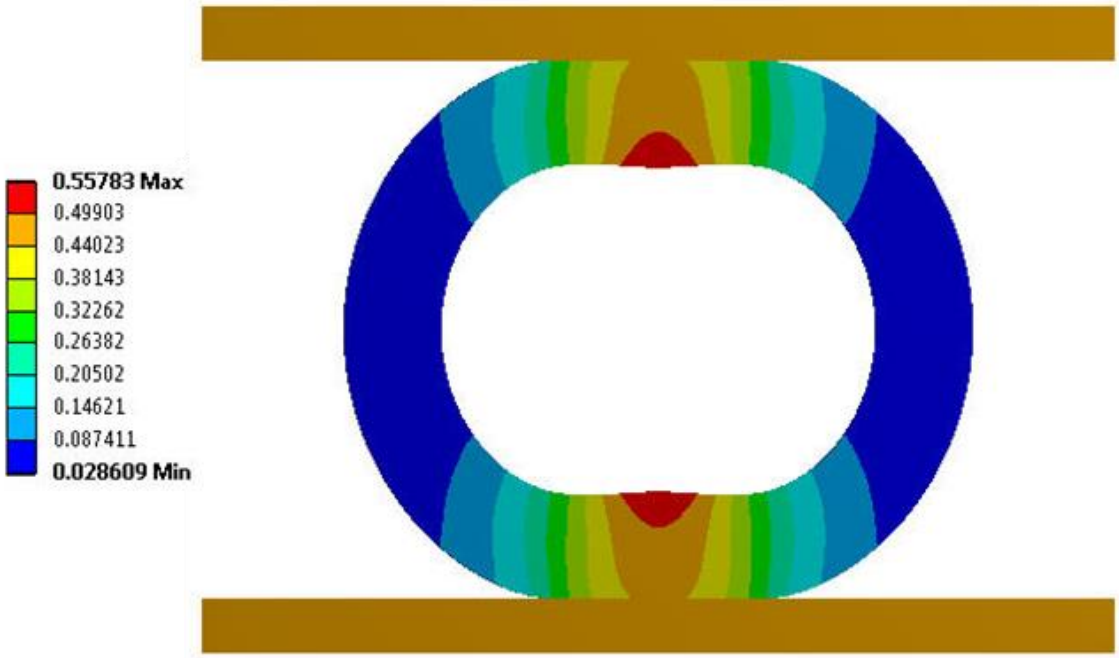


(b) t = 0.12 s

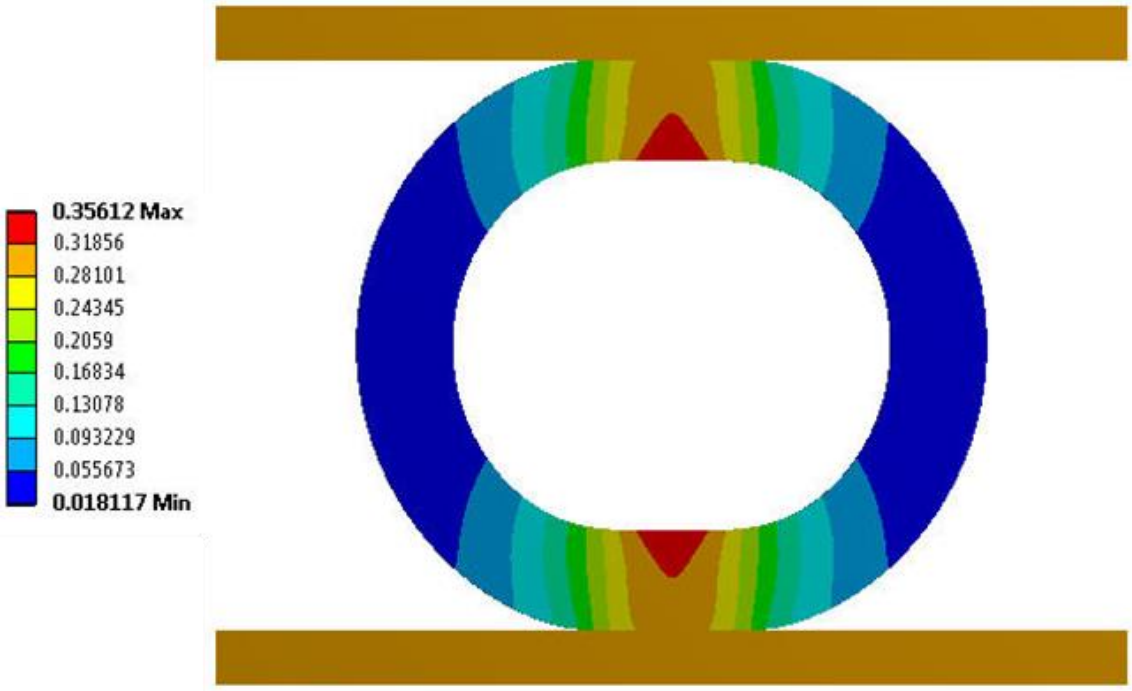


(c) t = 0.18 s

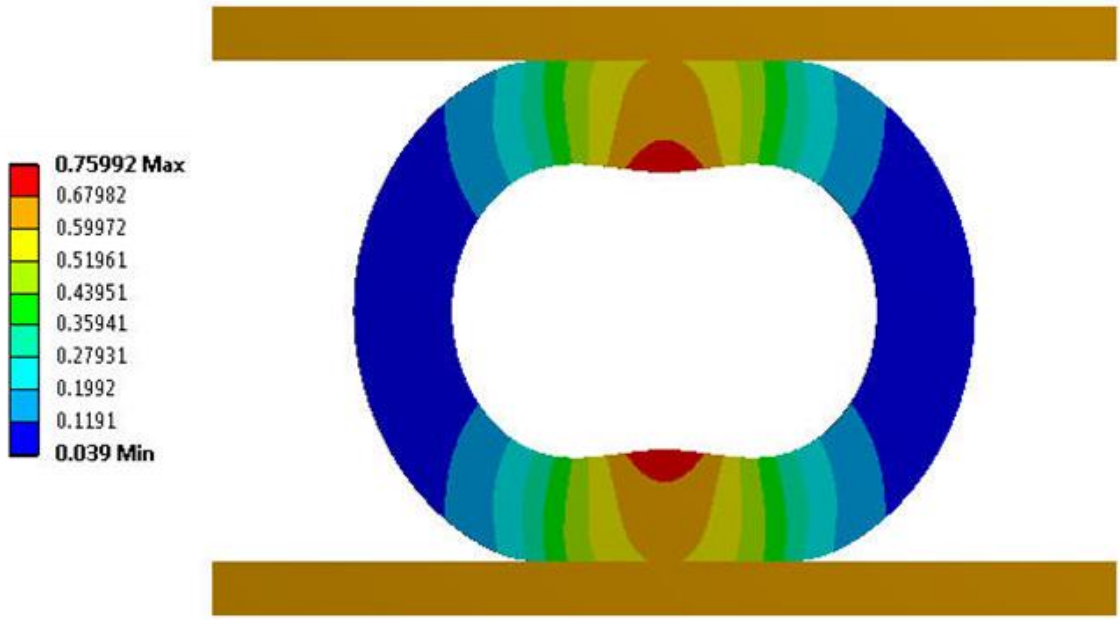


(d) t = 0.24 s

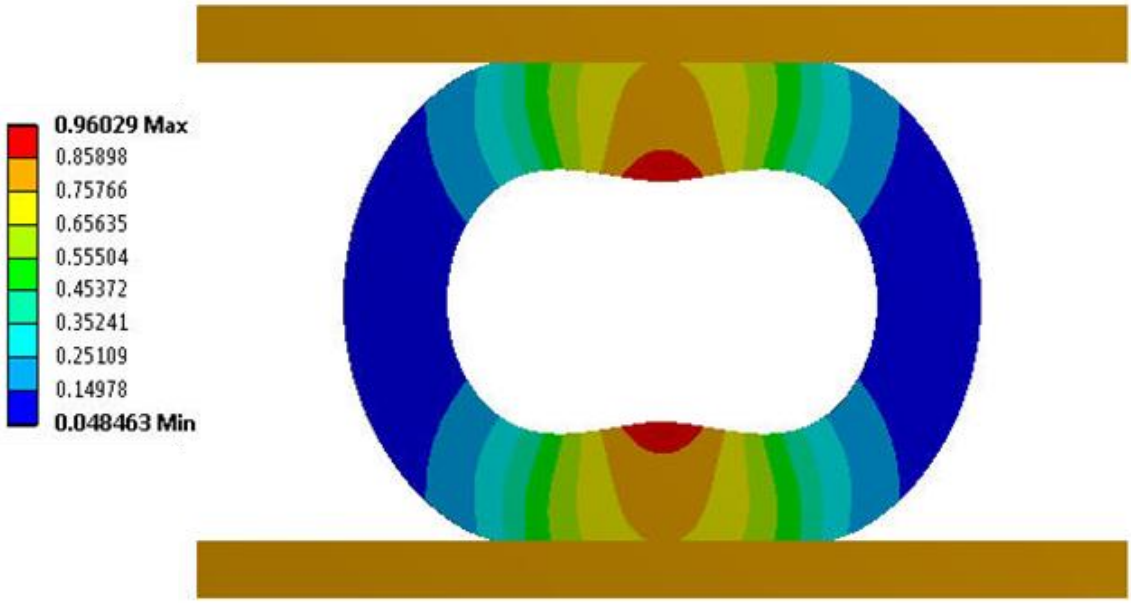


(e) t = 0.30 s

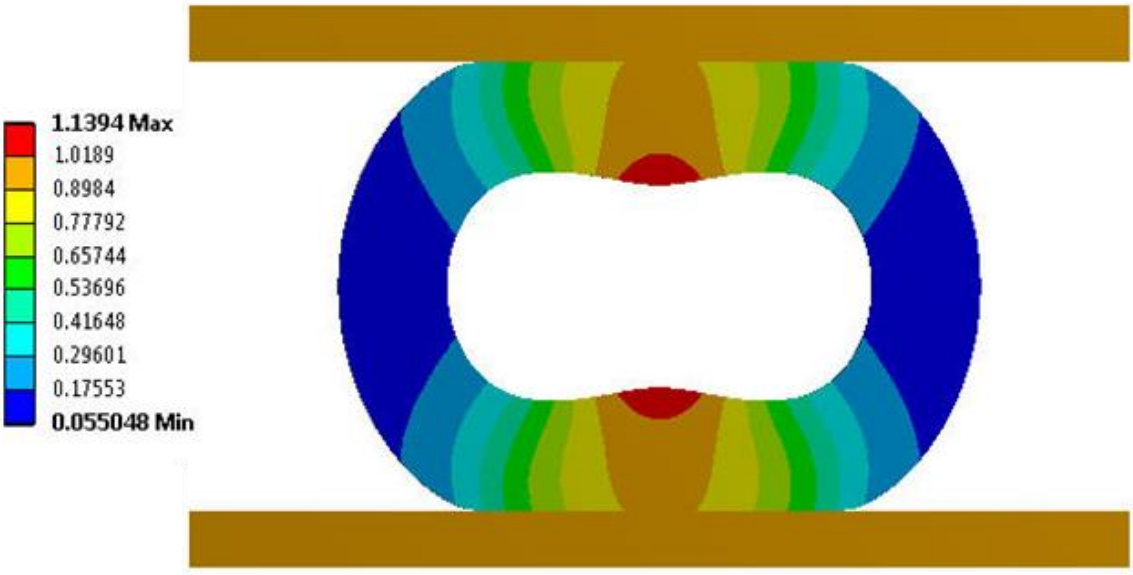


(f) t = 0.36 s

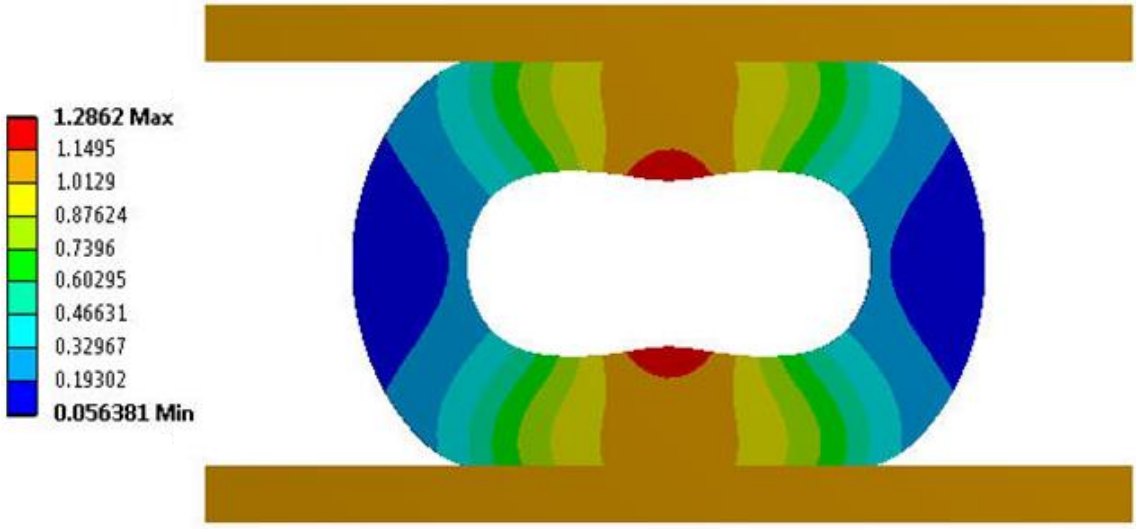


(g) t = 0.42 s

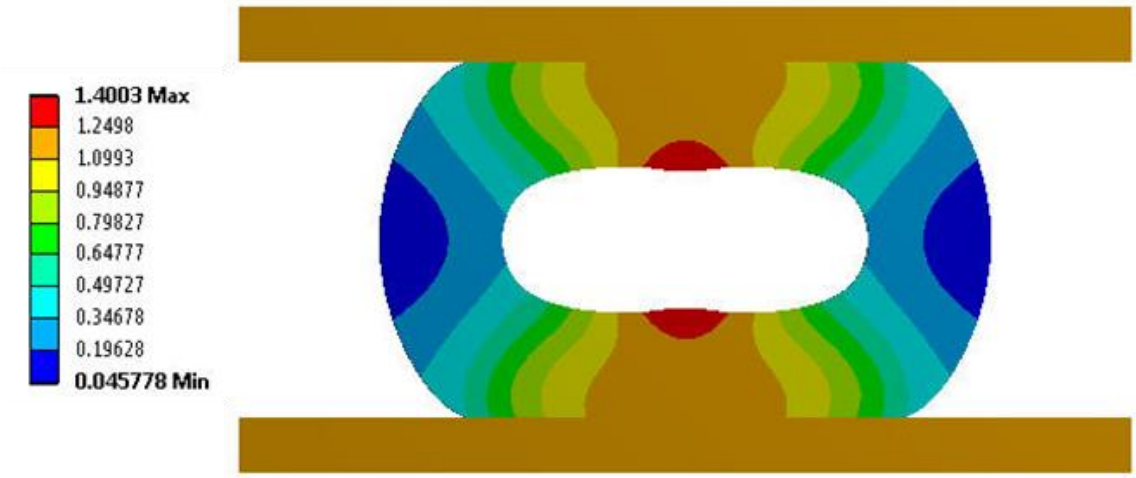


(h) t = 0.48 s

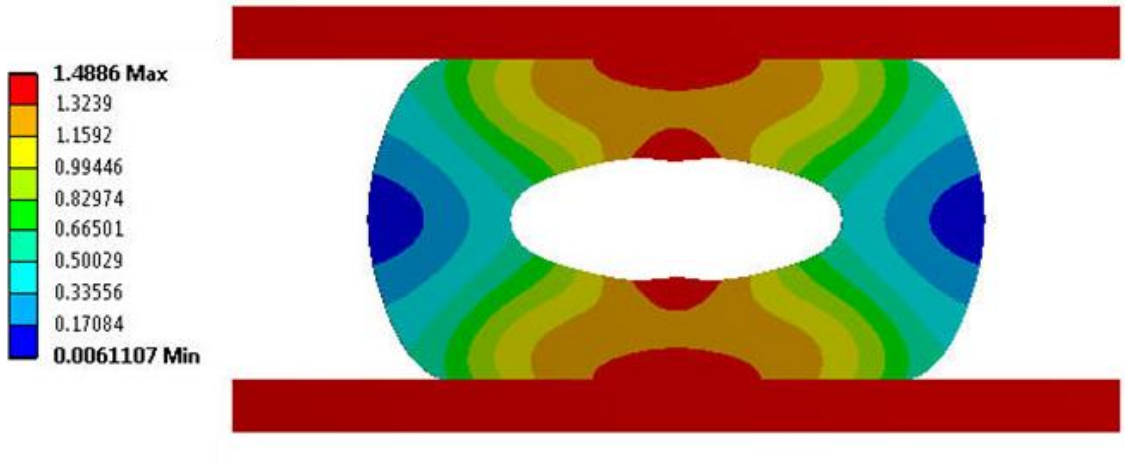


(i) t = 0.54 s

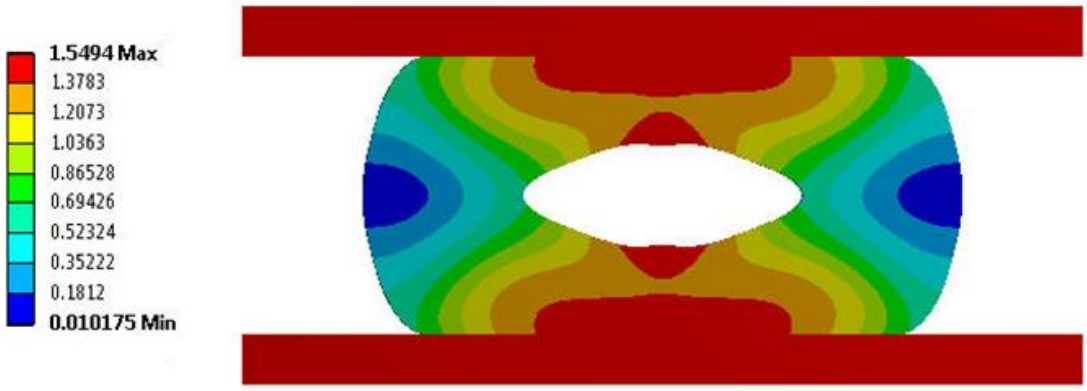


(j) t = 0. 59 s

Fig. 3.13 Distributions of the deflections at 0.06-second intervals throughout the peristaltic compression cycle. The deflections are in units of mm.

Another mode of presentation of deflection which is more quantitative than that of Fig. 3.13 is conveyed in Fig. 3.14. To illustrate the difference in the information conveyed by these figures, comparisons of the (a) and (j) parts of Fig. 3.13 suggests an overall broadening of the compressed tube whereas a comparison between parts (a) and (k) of the latter figure reveals that the actual broadening is slight and that the judgment based on

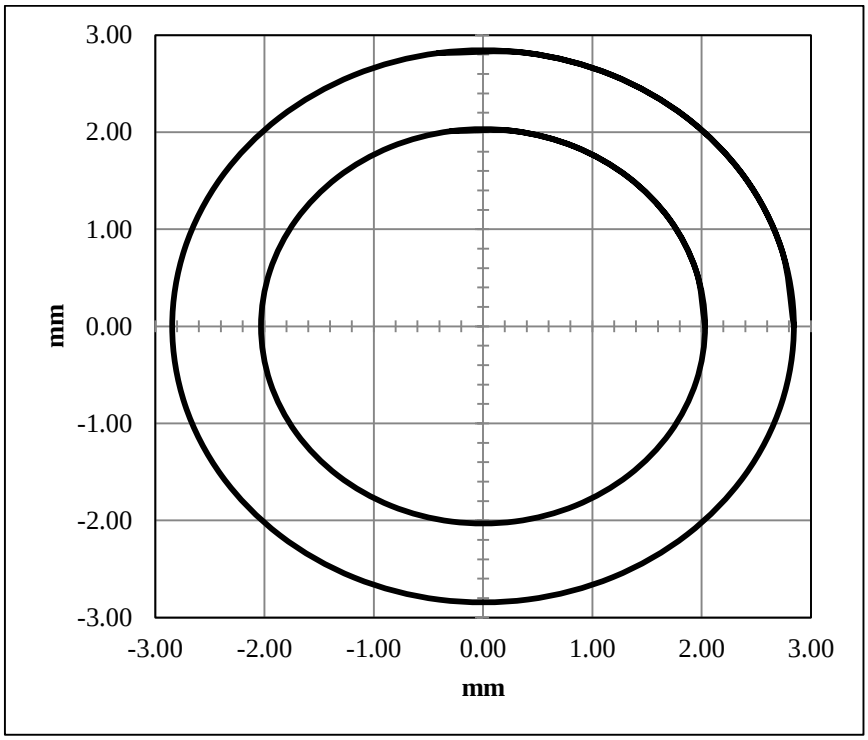
3.00
2.00
1.00
0.00
-1.00
-2.00
-3.00
mm
-3.00
-2.00
-1.00
0.00
1.00
2.00
3.00
mm

(a) t = 0 s

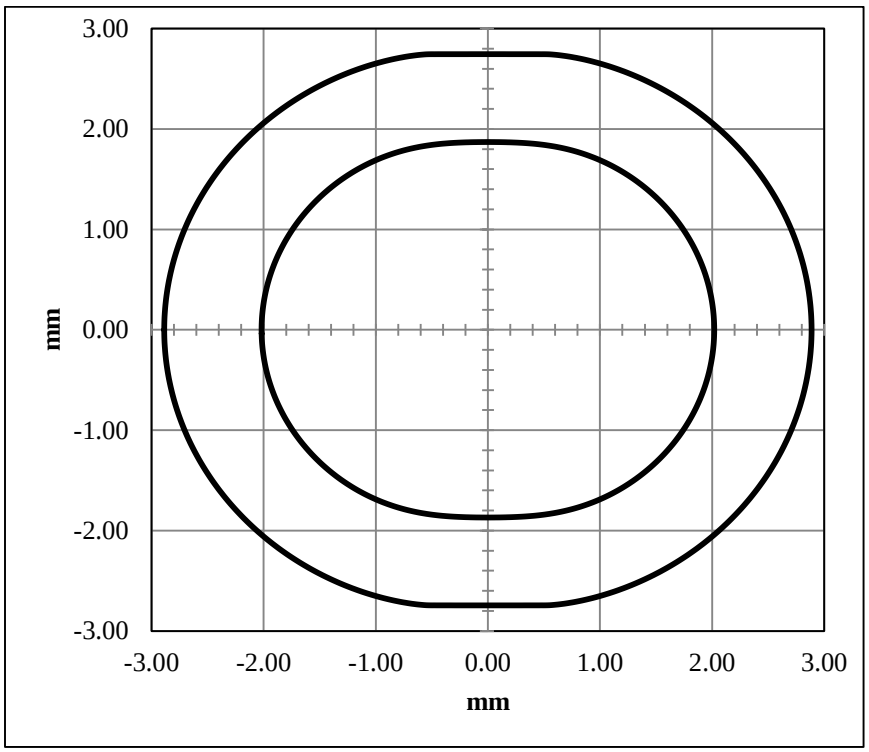
3.00
2.00
1.00
0.00
-1.00
-2.00
-3.00
mm
-3.00
-2.00
-1.00
0.00
1.00
2.00
3.00
mm

(b) t = 0.06 s

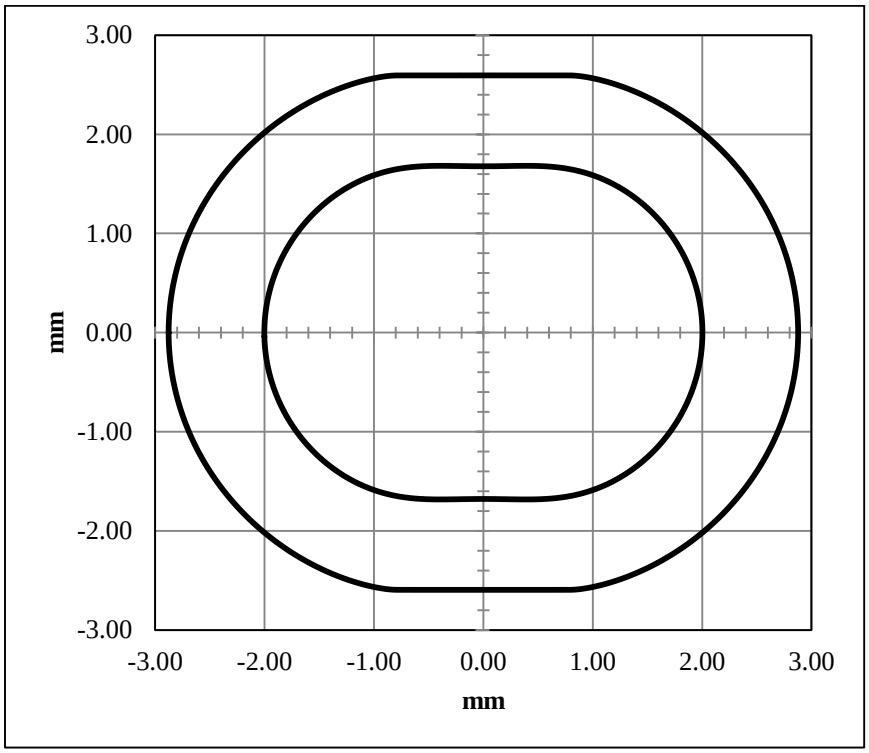


(c) t = 0.12 s

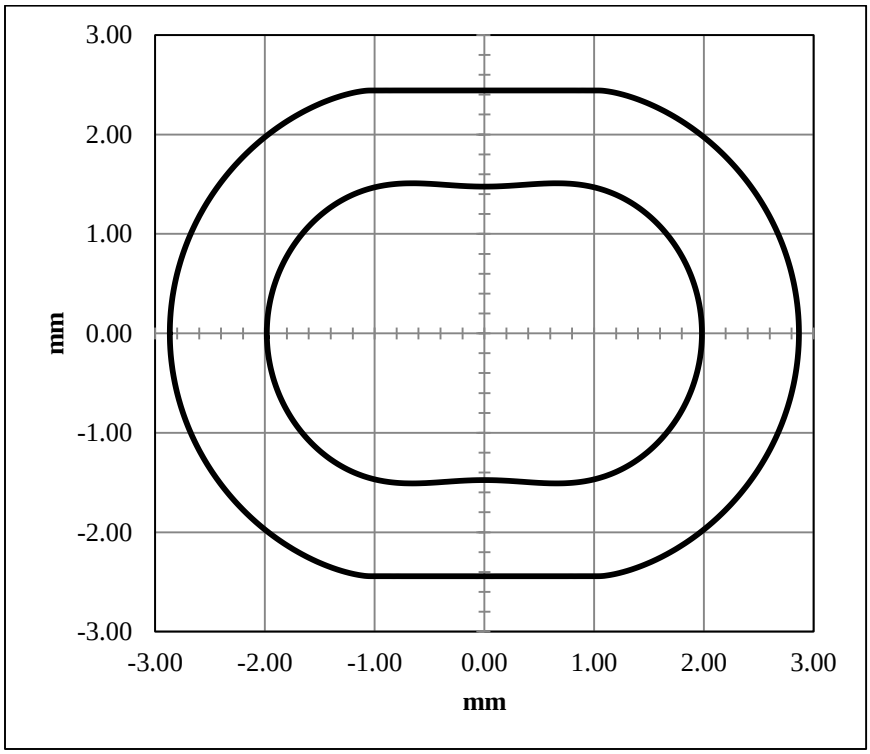


(d) t = 0.18 s

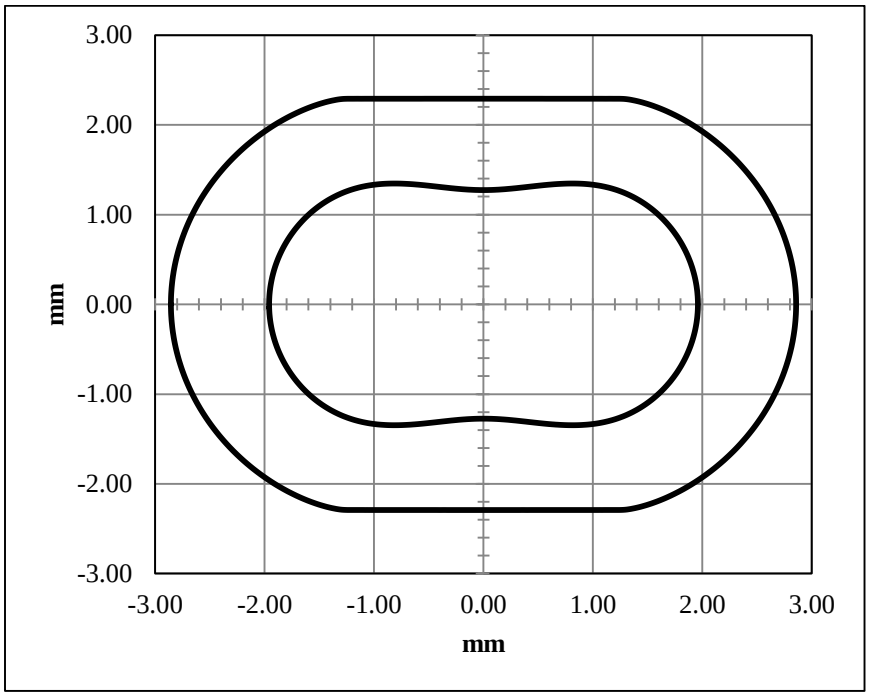


(e) t = 0.24 s

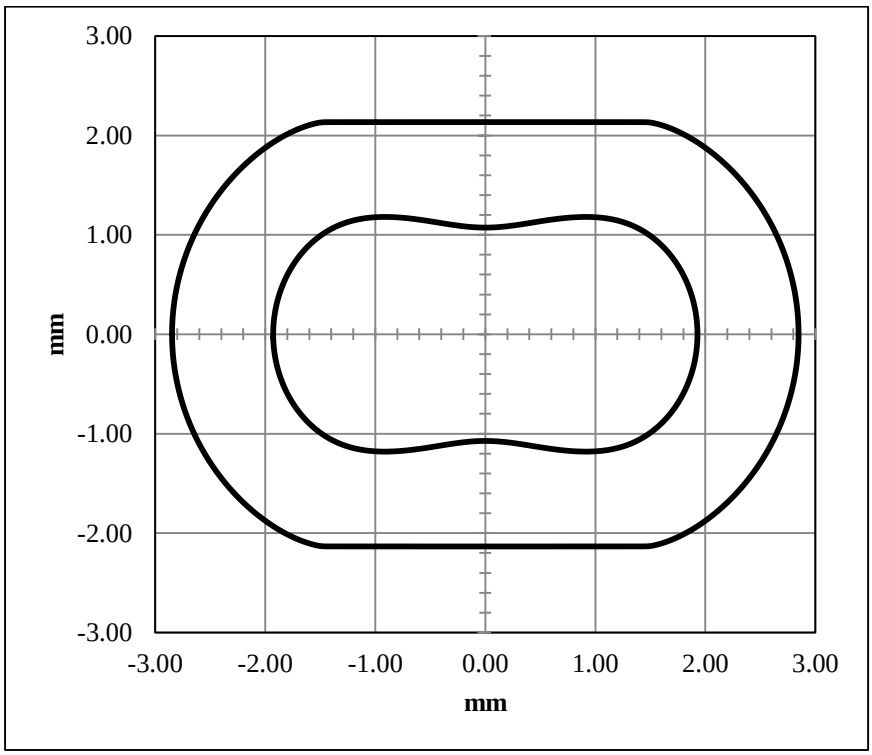


(f) t = 0.30 s

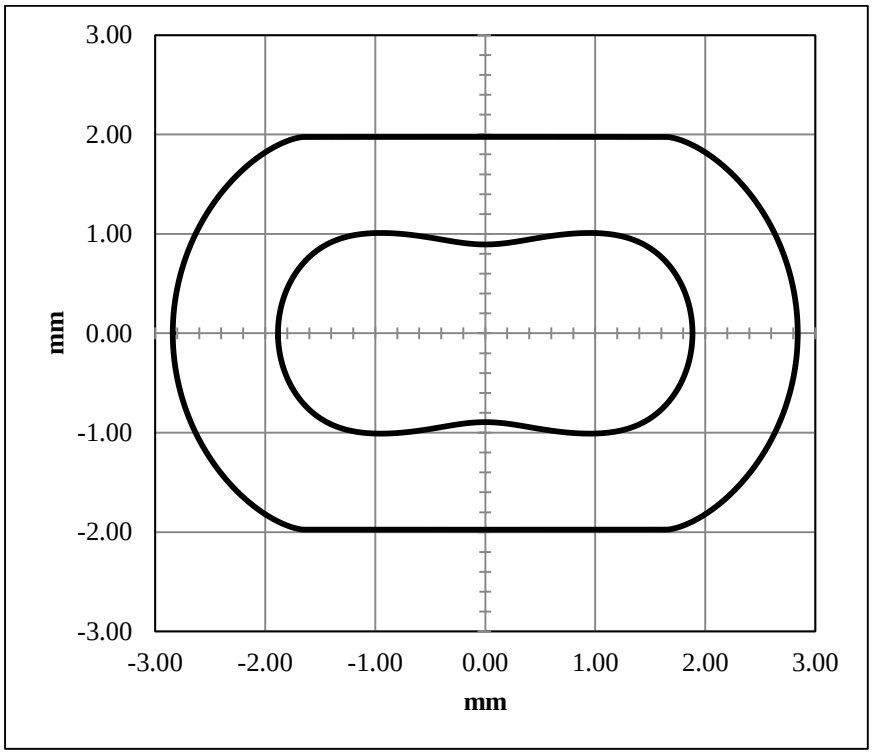


(g) t = 0.36 s

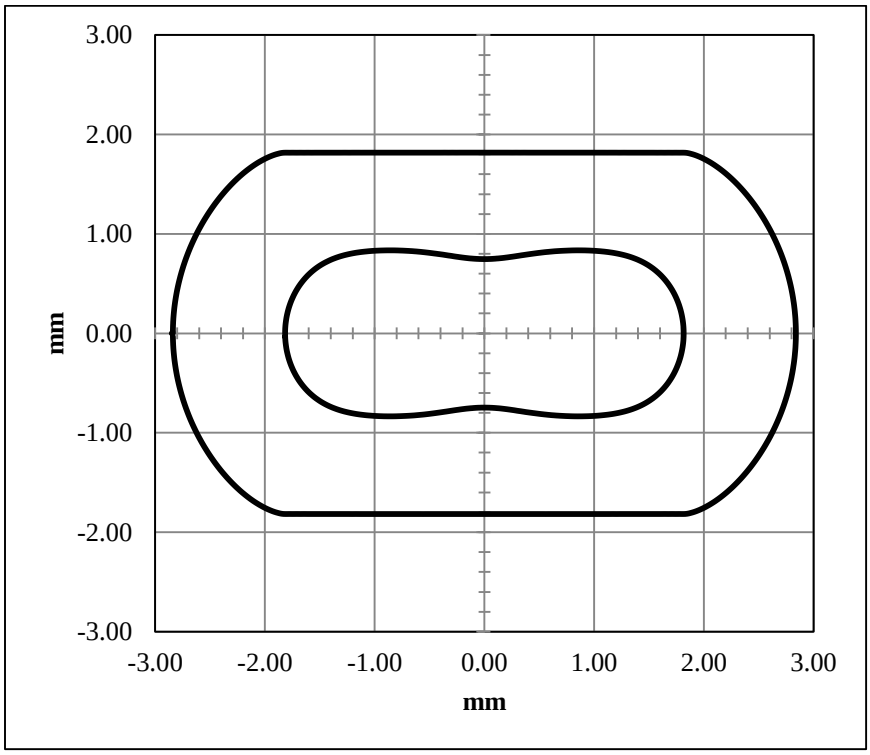


(h) t = 0.42 s

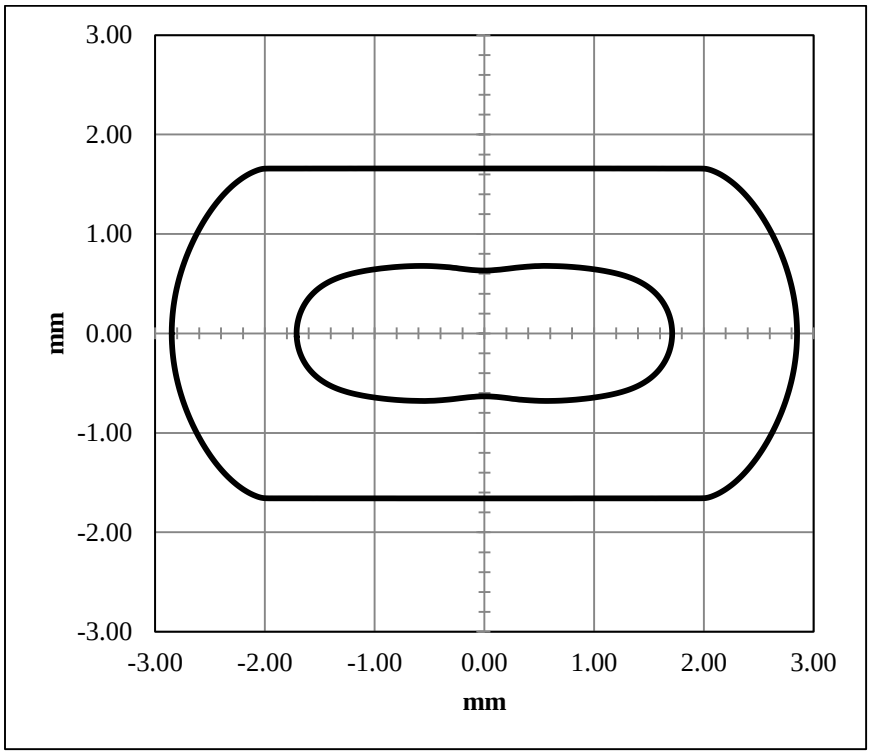


(i) t = 0.48 s

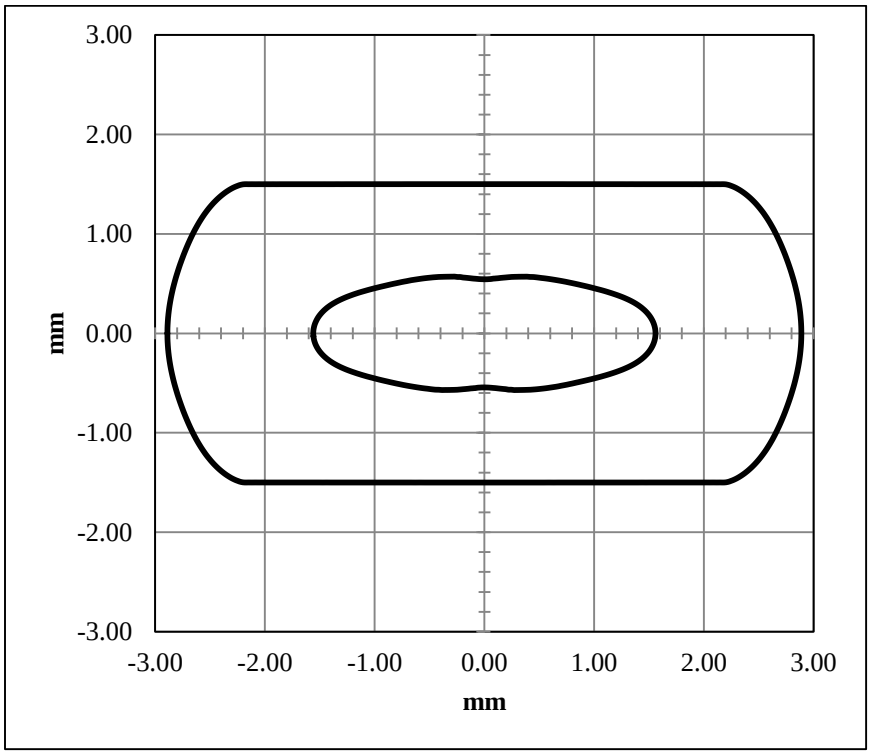


(j) t = 0.54 s

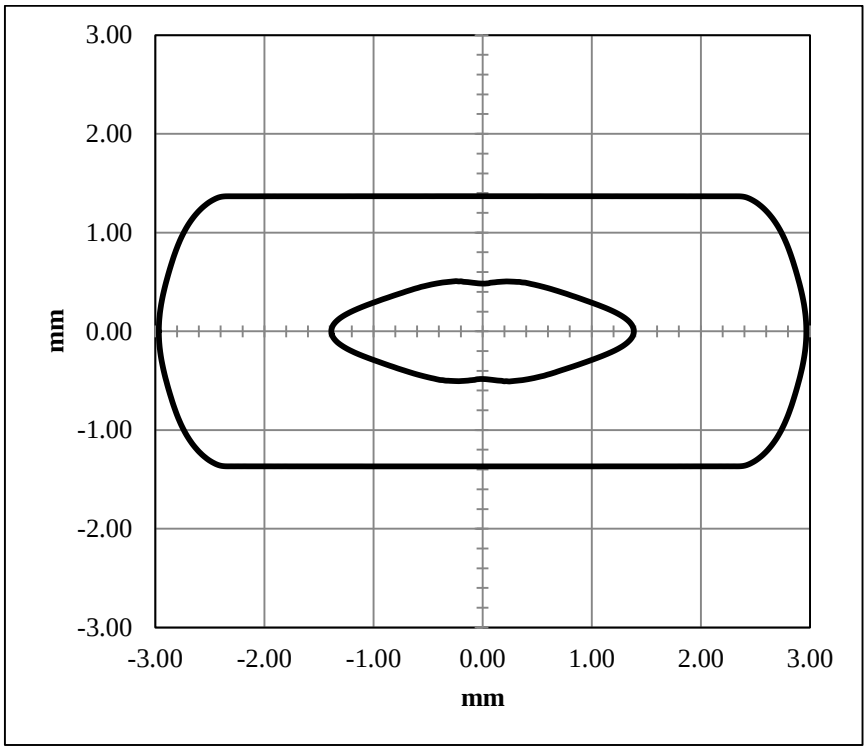


(k) t = 0.59 s

Fig. 3.14 Quantitative characterization of the deflections at 0.06-second intervals throughout the peristaltic compression cycle

Fig. 3.13 is an optical illusion. The flattening of the height of the tube as compression proceeds is absorbed by the diminution of the vertical height of the tube bore. This change in bore shape is reflected in the information already conveyed in Fig. 7 where the original cross sectional area of the bore is shown to be 15% of its original value.

Furthermore, from Fig. 3.14, part (a), it is seen that both the vertical and horizontal dimensions of the exterior of the undeformed tube are 5.70 mm. In contrast, for the final shape of the deformed tube, Fig. 3.14, part (k), the external horizontal dimension has increased very slightly to 5.94 (from 5.70 mm), while the external vertical dimension has diminished drastically to 2.74 mm (from 5.70 mm). This analysis demonstrates the type of quantitative information that is readily extracted from Fig. 3.14.

### 3.4.3 Analytical Solution

The foregoing problem has also been using an industry accepted analytical method. This method utilizes several aforementioned simplifications to allow the equations to be solved. These simplifications lead to an appreciable difference in the amount of fluid delivered. A basic schematic of the analytical model in the undeformed and fully deformed states can be found in Fig. 3.15.

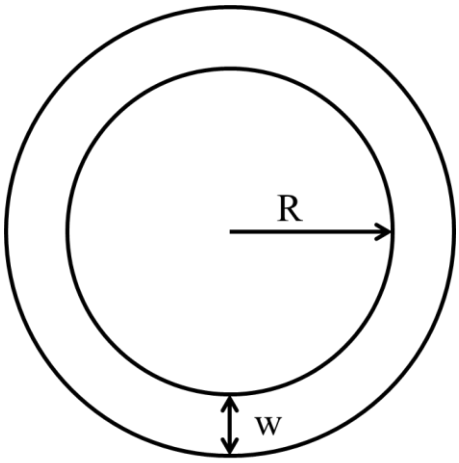


(a)

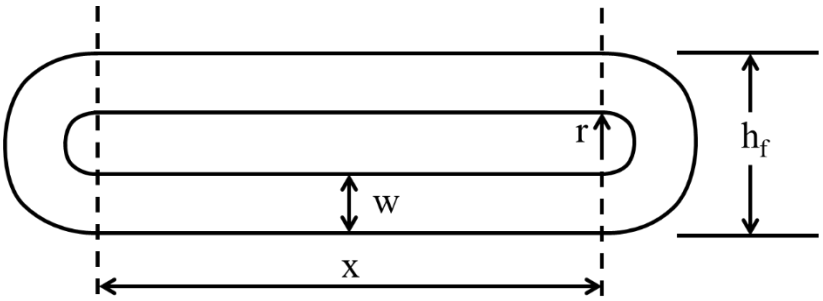


(b)

Fig. 3.15 (a) Schematic diagram of the undeformed model used in the analytical solution with inner radius, R, and wall thickness, w, shown. (b) Schematic diagram of the fully deformed model used in the analytical solution with inner radius, r, wall thickness, w, and inner length, x, shown.

As the fully deformed state shows, there are several simplifications within this analysis. The first and foremost is that wall thickness of the tube is constant at all locations in the fully deformed and undeformed states. This results in the simplification that the internal area in the fully deformed state, the area corresponding to fluid flow, consists of the area of a circle and of a rectangle which is represented by Eqs (3.7) and (3.8).

$$A_f = \pi r^2 + 2rx \tag{3.7}$$

$$r = \frac{h_f}{2} - w \tag{3.8}$$

The final simplification is assuming that the inner circumference of the undeformed state, C, is equal to the inner circumference of the fully deformed state, c. As Eqs (9)-(11) show, this assumption allows for the length of the inner rectangle, x, to be calculated.

$$C = 2\pi R \tag{3.9}$$

$$c = 2\pi r + 2x \tag{3.10}$$

$$x = \frac{C - 2\pi r}{2} \tag{3.11}$$

When the values of R, w, and $h_f$ used in the numerical simulation (2.032, 0.864, and 2.736 mms respectively) are applied to the equations above the volume of the bore ratio is found to be 0.129. This compares to a ratio of 0.158 from the fully deformed state in the numerical simulation. A comparison of this analysis method demonstrates that the analytical approach would result in a -18% error to the numerical solution.

## 3.5 CONCLUDING REMARKS

The primary focus of the research reported here is to place the design of mechanically-based peristaltic pumps on a firm fundamentals basis. A secondary goal is to demonstrate that therapeutic biomedical devices involving mechanical features can, in general, be designed to a very high standard of efficacy. The methodology set forth here is the use of

first principles implemented by numerical simulation. Provided that the computational resources are of sufficient capability, this methodology is able to avoid the oversimplifications that too often lead to erroneous results.

Primary attention must be given to the nature of the structural properties of the participating medium. Here, hyperelastic properties were deemed appropriate for the compressible tubular material that is commonly used for externally situated peristaltic pumping. The theory of hyperelastic stress and strain was used to underpin the analysis.

The software based on this theory yielded stresses and mechanical deflections. In particular, the applied force need to sustain the prescribed rate of compression was determined. From the numerical information about the change of the volume of the bore of the tube, the rate of fluid flow provided by the peristaltic pumping action was calculated.

Other results of practical utility include the spatial distributions of effective stress (von Mises) at a succession of times during the compression cycle. To complement the latter results, similar information was presented for the spatial and temporal evolution of the displacements.

Overall, the outcome of the work provides a complete complement of information for the efficacious design of a mechanically-driven peristaltic pump.

# Chapter Four

# THERMAL AND FLUID FLOW DESIGN OF A FLUID/BLOOD WARMER FOR CRITICAL TRAUMA APPLICATIONS

## 4.1 BACKGROUND

Heat exchangers are components of many biomedical devices. In particular, fluid warming is a necessary part of the total complement of therapeutic patient care activities. This recognition has motivated the present chapter in which a complex heat exchanger is analyzed from first principles in order to create a highly effective design methodology. The specific exchanger that motivated this investigation is a fluid warmer which is responsible for heating a fluid initially at 4$^{o}$C to a temperature of approximately 37$^{o}$C at a rate sufficiently high to make it available in a trauma situation.

The device in question is, in essence, a geometrically unique double-pipe heat exchanger. Double-pipe heat exchangers are, perhaps, the most common type of exchanger encountered in practice. In their simplest manifestation, they are the first convective heat transfer device encountered in basic heat transfer courses. In essence, a double-pipe exchanger consists of two pipes, one inside the other, that share a common axis. One of the participating fluids flows through the inner pipe while the other fluid flows in the annular space between the pipes. In most applications, both of the participating pipes are smooth surfaced. The typical analysis of double-pipe heat exchangers is based on a number of unrealistic assumptions. For example, it is commonly assumed that the coefficients of heat transfer, which govern the rate of heat transfer between the two fluids, are independent of spatial location. Another common assumption is to ignore the fact that one of the participating fluids must execute right-angle turns before entering and exiting the heat exchanger.

A schematic diagram of the primary physical situation to be investigated here is shown in Figs. 4.1(a), (b), and (c). Categorically, the heat transfer device displayed in these figures is an *enhanced* double-pipe heat exchanger, with the enhancement being due to a periodically helically corrugated internal pipe. The helical structure, seen in the external surface of the inner pipe, actually persists through the tube wall thickness and also appears in an internal view of the pipe. The (a) part of the figure is an overall schematic of the heat exchanger exposing the helically periodic corrugated pipe surface by means of a cutaway. The delivery and extraction means for the respective fluids are also illustrated. To the best knowledge of the author, the right-angle turns at the inlet and exit of the annulus flow have not been considered in any prior analysis of double-pipe heat exchangers. The (b) part of the figure is a close up of the helical corrugation pattern.

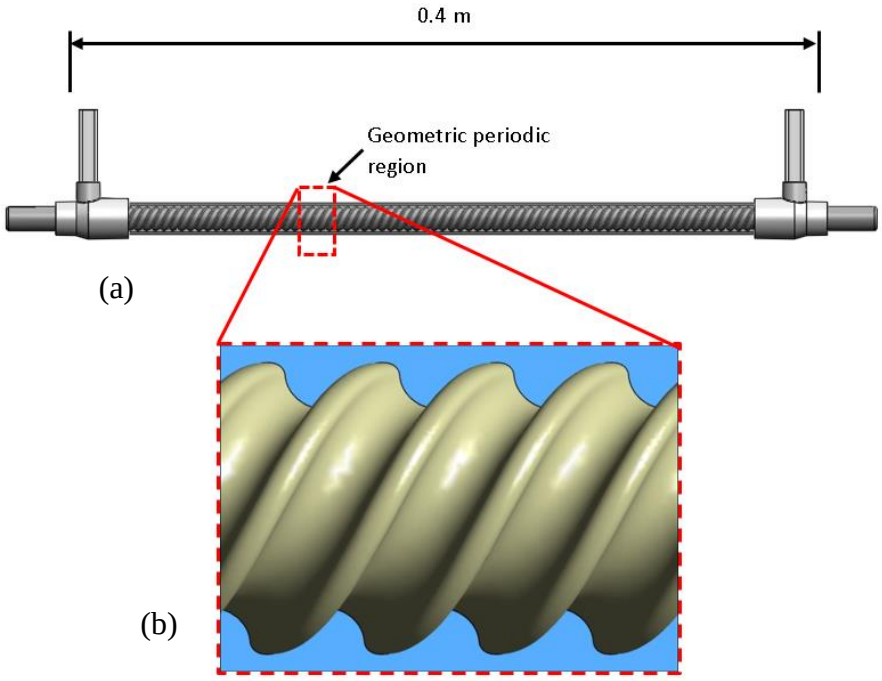

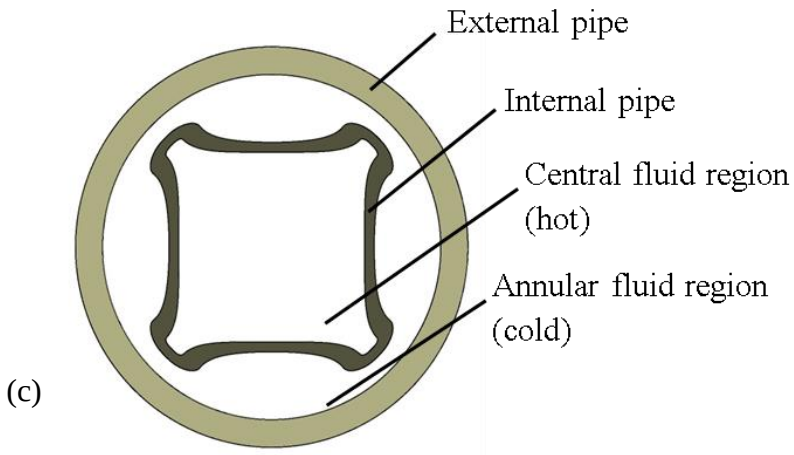


Fig. 4.1. Schematic views of the enhanced double-pipe heat exchanger: (a) Overall view, (b) close up of the helical surface of the inner tube of the double-pipe heat exchanger, (c) detailed cross-sectional view of the geometry of the double-pipe heat exchanger.

Clarification of the heat exchanger geometry is provided in the cross-sectional view shown in Fig. 4.1(c). It is seen that the external pipe, made of plastic, is circular whereas the internal pipe has a unique shape. That shape is readily produced by twisting a round aluminum pipe. The spacing between the two pipes that form the heat exchanger is maintained by supports at the ends of the assembly as can be seen in Fig. 4.1(a). Water is the chosen working fluid for both the pipe flow and the annulus flow. The hotter fluid passes through the central tube and the cooler fluid flows through the annulus.

The expected heat transfer enhancement due to the helical periodic geometry is based on two factors: (a) the increase in surface area associated with the tube geometry and (b) the swirl and consequent fluid mixing created by the helical twist. Since the helical corrugation exists at both the inner and outer surfaces of the central pipe, both the pipe flow and the annulus flow both experience swirl.

The fluid flow and heat transfer characteristics of the heat exchanger displayed in Fig. 4.1 were determined by numerical simulation. The present investigation includes:

(a) Detailed end-to-end studies of the flow and heat transfer processes for both parallel flow and counterflow
(b) Temperature-dependent thermophysical properties and constant thermophysical properties
(c) Spatially periodic solutions based on the periodicity of the helical geometry
(d) Smooth-surface pipe studies to compare with the results for the heat exchanger with the helically corrugated pipe surface

In addition to the detailed investigation of the enhanced heat exchanger displayed in the Fig.4.1, a complementary numerical simulation study was made of a corresponding double-pipe heat exchanger incorporating a smooth-surfaced pipe instead of the corrugated pipe. For the complementary simulations, the heat exchanger had the same overall dimensions and operating conditions as the enhanced exchanger. The results for the unenhanced exchanger are to be compared with those for the enhanced device.

The literature search was focused on enhanced double-pipe heat exchangers. In such heat exchangers, two fluids of different temperatures are brought together in intimate thermal contact without mixing. The temperature difference between the fluids results in one of them being heated while the other is cooled. A description of representative physical situations that appear in the literature now follows. A number of studies of double-pipe heat exchangers involving porous media are reported in [62] (porous substrates), [63] (porous structures), [64] (porous fins), [65] (porous baffles in the presence of pulsation), and [66] (metal foam). The investigation of wire and other inserts incorporated into double-pipe heat exchangers was performed in [67-70] (circular wires), and [71] (twisted tapes). In [72], the actual pipes are deployed in a helical coil pattern. Other enhanced double-pipe heat exchangers involved features such as [73,74] (fins), [75] (louvered strips), [76] (ring protuberances), [77] (twisted inner square tube in an outer circular tube), and [78] (bulbous protrusions in the inner tube wall). The literature involving corrugated double pipe heat exchangers is virtually exclusively concerned with experimentation. Representative among these are [79,80]. The foregoing references convey research

advances. There is in parallel a number of publications that are concerned with applications. Typical of this group are [81-83], which relate to food and chemical processing in general.

## 4.2. PHYSICAL SITUATION

The general description of the physical situation set forth in the previous section of the paper will now be expanded in detail. The overall thermal and fluid flow configuration of the exchanger is presented in Fig. 4.2 (a) and (b) along with relevant thermal nomenclature. The flow directions of the participating fluids are shown in Part (a) for parallel flow and in Part (b) in counter flow. Note that the cooler fluid, which corresponds to that which flows in the annulus, is always introduced at the upper left. The hotter fluid, which flows in the twisted pipe, enters at the left for parallel flow and at the right for counter flow.

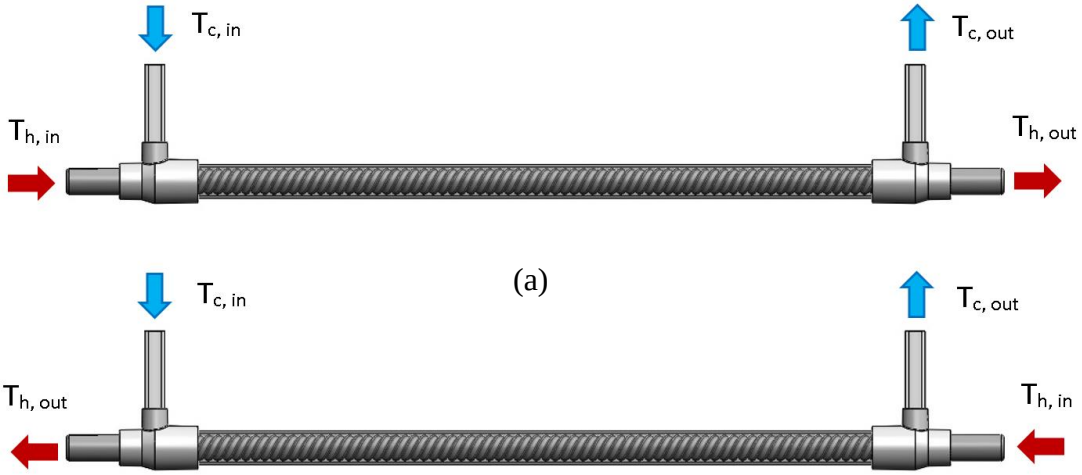


Fig. 4.2 Overall diagram of the thermal and fluid flow setup of the heat exchanger. As shown, the length of the heat exchanger section is 40 cm with a pitch of 1/2 turn per cm.

Dimensional details relevant to the heat exchanger are provided by Fig. 4.3. The complexity of the wall of the inner pipe defies a simple listing of dimensions, and the scheme used in Fig. 4.3 is believed to be the most effective way to convey the dimensional

information. To complete the information conveyed by the figure, it may be noted that the actual inside diameter D of the external pipe is 14.22 mm.

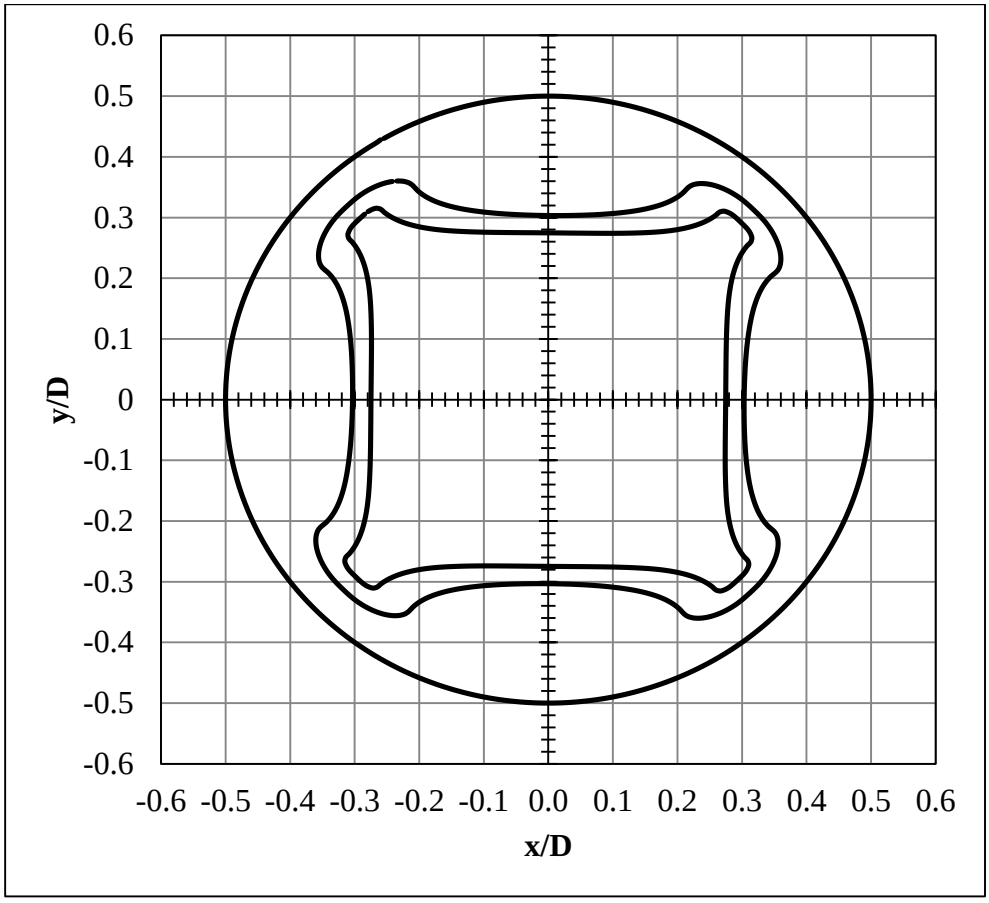


Fig. 4.3 Cross-sectional dimensions of the double-pipe heat exchanger.

The degree of twist is one of the parameters of the study. Three different twists were investigated: (a) 1/6 turn per cm of length, (b) 1/3 turn per cm, and (c) 1/2 turn per cm.

With regard to the materials of fabrication of the heat exchanger, the internal pipe is modeled as either aluminum or plastic whereas the outer pipe is of plastic. The hotter of the two participating fluids flowed through the central pipe, and the cooler fluid flowed through the annulus. This is the pattern used in most fluid-warming applications. The material properties used in the subsequent numerical solutions are listed in Table 4.1.

Table 4.1 Relevant Material Properties

| Material | k (W/m-$^{o}$C) | μ (kg/m-s) |
|---|---|---|
| Variable-property water | IAPWS IF97 library data [84] | |
| Constant-property water | 0.607 | 0.0008899 |
| Aluminum | 237 | |
| Plastic | 0.2 | |

## 4.3 FLUID FLOW NUMERICAL SIMULATION

### 4.3.1 Governing Equations

Initially, both laminar and turbulent flows were investigated. However, for the selected Reynolds numbers of the participating flows, which were chosen in accordance with current practice, it was found that the flow regime was definitely laminar. This conclusion was based on supplementary numerical simulations, as follows. It was documented in [85] that the SST turbulence model reduces to laminar flow when it is applied to a fluid flow situation where the flow regime is actually laminar. When numerical simulations for the present situation were run using the SST turbulence model, results were obtained that were identical to those given by the laminar model. In addition, the SST model was used to evaluate the turbulence viscosity $\mu_{turb}$, with the outcome $\mu_{turb} = 0$. This demonstration ensures that laminar flow is the correct model for this investigation. When a laminar situation is modeled with high fidelity and convergence of the numerical simulation is achieved, it is widely assumed that the solution is valid.

The relevant physical principles that govern the flow and convective heat transfer are: momentum conservation (Navier-Stokes equations), mass conservation, and the First Law of Thermodynamics. These equations are written for steady three-dimensional flows and conjugate heat transfer with temperature-dependent thermophysical properties.

The Navier-Stokes equations in the compact Cartesian-tensor form are

$$\frac{\partial(\rho u_j u_i)}{\partial x_i} = -\frac{\partial p}{\partial x_j} + \frac{\partial}{\partial x_i}\left(\mu \frac{\partial u_j}{\partial x_i}\right) \qquad i = 1,2,3 \quad j = 1,2,3 \tag{4.1}$$

and the mass conservation equation is

$$\frac{\partial(\rho u_i)}{\partial x_i} = 0 \tag{4.2}$$

The $u_i$ are the velocity components, $x_i$ the coordinates, $p$ the pressure, and $\rho$ and $\mu$ the density and viscosity, respectively.

The heat transfer problem is governed by the First Law of Thermodynamics in conjunction with the Fourier heat conduction law. For the flowing fluid, the energy equation is,

$$\frac{\partial(\rho u_i h)}{\partial x_i} = \frac{\partial}{\partial x_i}\left[k_{fluid} \frac{\partial T}{\partial x_i}\right] \tag{4.3}$$

in which $T$ is the fluid temperature, $h$ is the specific enthalpy, and $k_{fluid}$ is the thermal conductivity of the fluid. The convective heat transfer in the fluid is intimately connected with heat conduction in the wall of the inner pipe. The governing equation for the wall heat conduction is,

$$\frac{\partial}{\partial x_i}\left[k_{wall} \frac{\partial T}{\partial x_i}\right] = 0 \tag{4.4}$$

Equations (4.1)-(4.3) are applied to separately to each of the participating fluids, and Eq. (4.4) provides coupling. For fluids with assumed constant properties, the velocity problems for the annulus and the pipe fluids are independent of each other, but the temperatures of the two fluids are tightly interrelated. When temperature-dependent properties are taken into account, the velocity problems for the two fluids are coupled as are the heat transfer problems.

**4.3.2 Boundary Conditions**

It remains to specify the boundary conditions and the coupling conditions which relate the participating flows. Both parallel flow and counter flow were considered. At the respective *inlet* cross sections, the entering velocities were assumed to have uniform profiles, and similarly for the entering temperature profiles. Downstream of the respective inlets, the velocity and temperature fields experience development with increasing downstream distance. In the case of constant-property fluids, the values of the entering temperatures can be arbitrarily specified without affecting the dimensionless heat transfer results. On the other hand, in the case of temperature-dependent fluid properties, the inlet temperatures, based on practice, were specified to be 4 and 50$^{o}$C, respectively for the cooler and hotter fluids. Heat conduction in the wall of the inner pipe was taken into account, and this created the thermal bridge between the participating fluids. In accordance with accepted heat exchanger practice, the outer surface of the outside pipe was specified to be adiabatic.

The foregoing discussion was primarily focused on the implementation of the model in which the entire heat exchanger was simulated from end-to-end. As was mentioned earlier, another model was formulated and implemented in which each full turn of the helical geometry was postulated to be a fundamental geometrical module into which the entire length of the heat exchanger could be subdivided. That model envisions the heat exchanger as being geometrically spatially periodic.

For the three helical winding patterns were chosen for study: (a) 1/6 turn per cm, (b) 1/3 turn per cm, and (c) 1/2 turn per cm. An alternative mode of description of these patterns is: (a) one turn in 6 cm, (b) one turn in 3 cm, and (c) one turn in 2 cm. If the overall length of the exchanger is approximately 40 cm, these three situations would respectively correspond to approximately 6.6, 13.3, and 20 modules distributed along the length.

The periodicity concept is based on the velocity field in each and every module being the same. Consequently, the velocity distribution at the inlet cross section of a module must be identical to the velocity distribution at the exit cross section, but neither is cross-sectionally

uniform. Another consequence is that the per-module pressure drop is the same for all modules. Once a periodic velocity solution possessing the aforementioned attributes had been obtained, the resulting velocity field is used as input for the solution of the per-module heat transfer problem.

One of the drawbacks of the periodic-module model is that it is restricted to constant-property fluids. With regard to heat transfer, the temperature at the inlets of the respective fluids were assigned values whose difference was $10^{o}$C, both for parallel or counter flow. However, because of the constant-property model and the linearity of the energy equations, the computed values of the thermal resistance are not affected by the assumed difference in the temperatures.

### 4.3.3 Mesh Configuration

The geometric complexity of the problem gave rise to an equally complex pattern of fluid flow which required a highly refined numerical discretization of the solution domain in order to achieve solutions of sufficient accuracy. The issue of accuracy is closely connected with the need to prove that the solution is independent of the mesh that is created by the discretization. In this connection, exploratory solutions were obtained for meshes ranging from 17,580,000 to 36,225,000 nodes for the full end-to-end model (40 cm in the flow direction). Over this nodal range, the overall heat transfer rate varied by 3%. The periodic model required many fewer nodes for its accurate implementation, specifically ranging from 3 to 3.3 million, depending on the pitch, to establish accuracy. For all cases, a solution was regarded as converged when the residuals for all of the participating equations were less than $10^{-6}$. All of the completed solutions had a perfect balance of mass entering and leaving the solution domain. The simulations were run on a cluster of Linux machines operating with openSUSE 13.1. The CPU time ranged from 20 to 70 days depending on the number of nodes and number of partitions (processors) used.

A display exhibiting a typical section of the mesh is presented in Fig. 4.4(a)-(c). The respective parts of the figure are: (a) three-dimensional pictorial view, (b) cross-sectional view, and (c) magnified segment of the mesh cross section. As seen in the figure, great refinement was needed to treat the geometrical complexities.

Both the discretization and the numerical solutions were performed by means of ANSYS CFX 16.1 software.

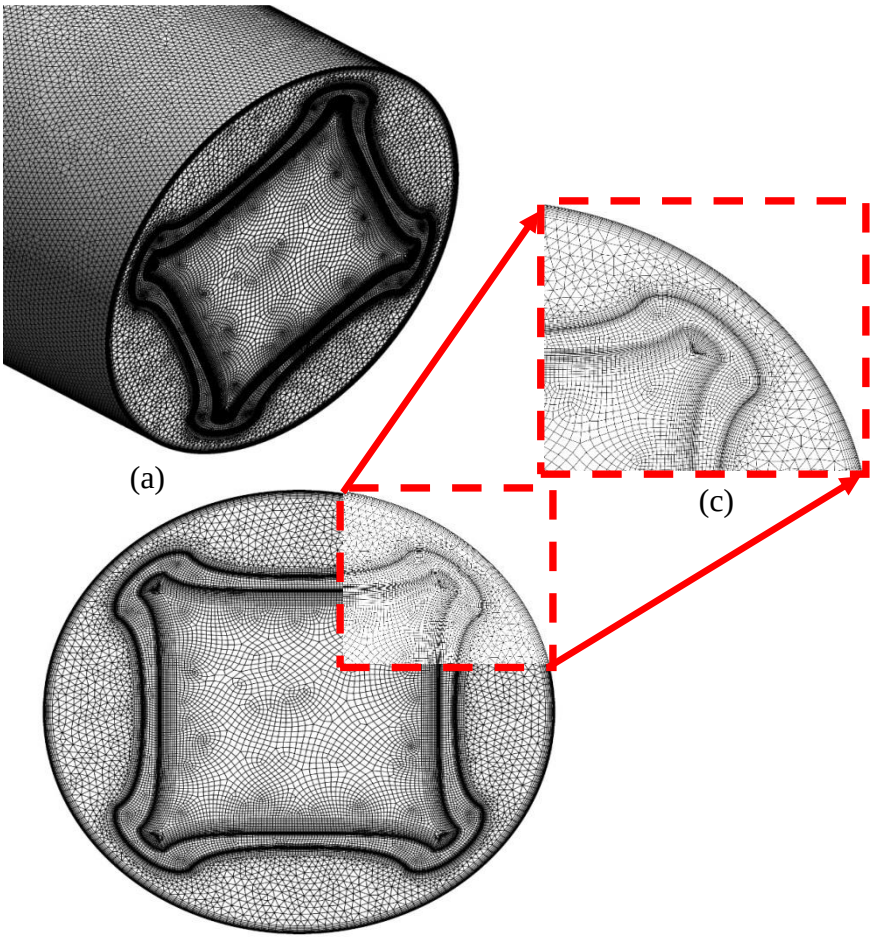


Fig. 4.4 Typical section of mesh used for the numerical simulation of the end-to-end model

## 4.4. RESULTS AND DISCUSSION

### 4.4.1 Heat Transfer Results

Heat transfer results will be conveyed in several forms in order to enable their convenient use in design. The first form to be presented is module-based for both parallel- and counter-flow configurations for constant-property fluids. This information is parameterized by the geometry of the helix which defines the pipe wall and by the Reynolds numbers of the pipe and annular flows. Next, end-to-end overall rates of heat transfer for both parallel and counter flow and both constant- and variable-property fluids are conveyed. These results will be compared with separately determined results for smooth surfaced pipes in order to identify the degree of enhancement that is attributable to the corrugations. The last set of heat transfer results are local fluxes and local wall temperatures. For all of the considered situations, both the pipe and annulus flows are water. Also, the outer wall of the annulus is assumed to be adiabatic.

The results are parameterized by the Reynolds numbers of the pipe and the annular flows, $Re_{pipe}$ and $Re_{annulus}$ respectively. These quantities are defined as

$$Re_{pipe} = \frac{4\dot{m}_{pipe}}{\mu P_{pipe}} \tag{4.5}$$

$$Re_{annulus} = \frac{4\dot{m}_{annulus}}{\mu P_{annulus}} \tag{4.6}$$

In these equations, $\dot{m}$ is the mass flow rate and $P$ is the perimeter which bounds the flow cross section. Perimeter values relevant to the investigated heat exchanger are 3.51 cm and 8.36 cm, relevant to the pipe flow and the annulus flow.

#### *4.4.1.1 Module-based heat transfer results*

The most applicable type of heat transfer result because of its superpositional nature is presented in the following for the modular representation of the heat exchanger. As will be demonstrated shortly, these results enable design calculations to be made with relative ease.

The module-based heat transfer results are conveyed in Figs. 4.5 and 4.6, respectively for counter flow and for parallel flow. In each figure, the thermal resistance per unit axial length is plotted as a function of the Reynolds number of the pipe flow. The curves are parameterized by the geometry of the helical winding expressed as the number of turns per centimeter and by the material of the wall of the inner pipe, either aluminum or plastic. There are two sets of curves in each figure, one of which correspond to an aluminum pipe and the other to a plastic pipe. There are two sets of curves in each figure, one of which correspond to an aluminum pipe and the other to a plastic pipe. Note that the results of Figs. 4.5 and 4.6 are for a Reynolds number of the annular flow of 420.

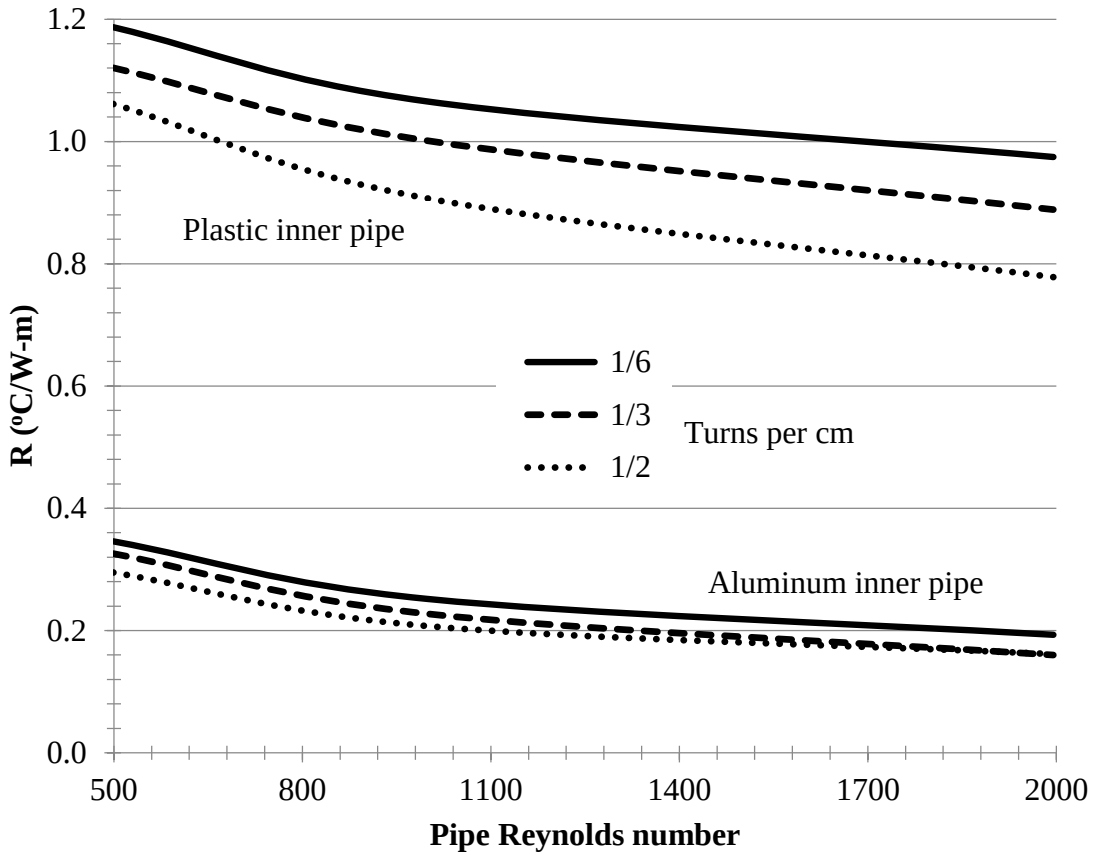


Fig. 4.5 Thermal resistance per unit axial length for a counter-flow heat exchanger and a constant-property, modular model. The Reynolds number of the annular flow is 420

Inspection of Figs. 4.5 and 4.6 reveals a strong dependence of the thermal resistance on the material of the pipe. There is an approximate ratio of four to five in the resistance value when the pipe is a plastic compared to that for an aluminum pipe. The importance of the conductive resistance of the wall of the inner pipe can be attributed to the moderate thermal resistances of the water flows in the respective flow passages. The average conductive resistance of the plastic wall was approximately 0.23ºC/W whereas the average value for the aluminum pipe was around 1.9 x $10^{-4}$ºC/W. Other trends that can be seen in these figures is a monotonic decrease of the resistance with an increasing number of turns per cm and a monotonic decrease of the resistance with increasing values of the pipe Reynolds

number. The latter trend is a result of the increasing heat transfer coefficient for the pipe flow that occurs with higher values of the pipe Reynolds number.

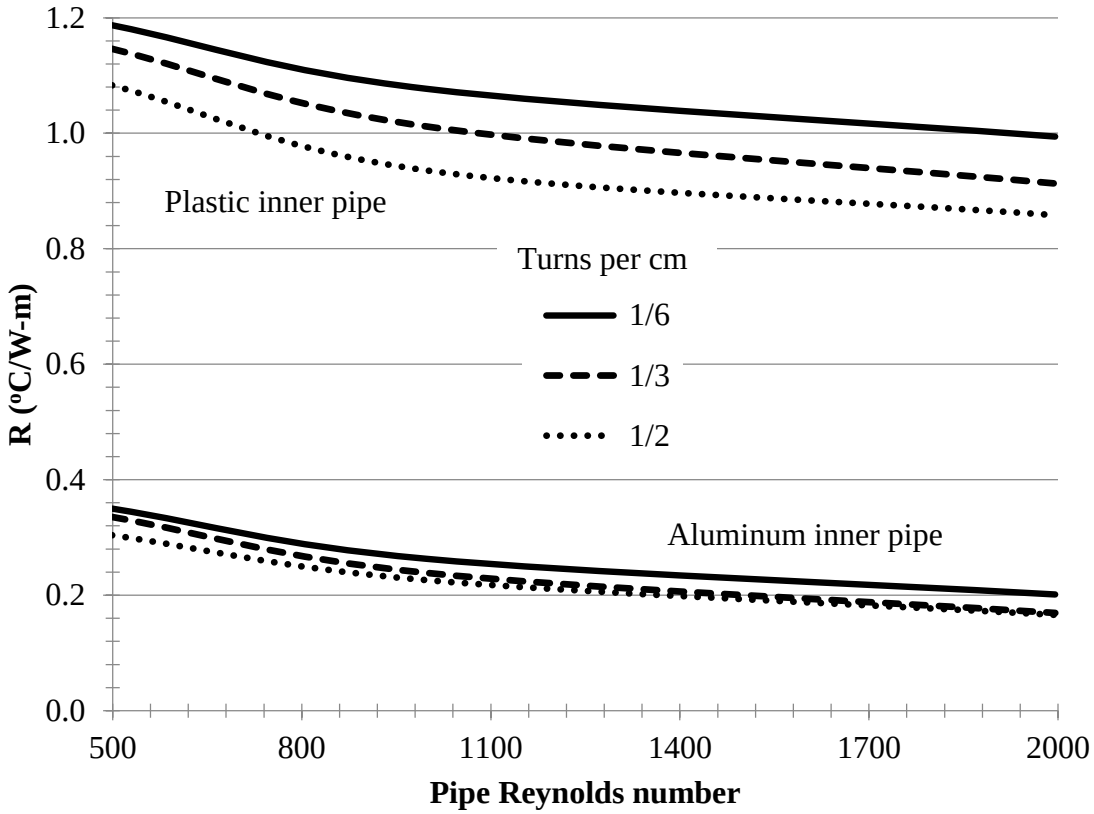


Fig. 4.6 Thermal resistance per unit axial length for a parallel-flow heat exchanger and a constant-property, modular model. The Reynolds number of the annular flow is 420

It is relevant to show how the information conveyed in Figs. 4.5 and 4.6 can be used for design. As is common in heat exchanger design situations, the temperatures at the respective inlets of the warmer and cooler fluids are specified. Also specified are the flow rates of the two fluids. This information enables the application of the First Law Thermodynamics to the respective fluids, so that

$$Q = \left[\dot{m}c_p(T_{in} - T_{out})\right]_{hotter} = \left[\dot{m}c_p(T_{out} - T_{in})\right]_{cooler} \tag{4.7}$$

In addition, if the resistance taken from the figures is multiplied by the overall length *L*, the rate equation is as follows

$$Q = \frac{LMTD}{R \times L} \tag{4.8}$$

where, for parallel flow,

$$LMTD = \frac{(T_{h,in} - T_{c,in}) - (T_{h,out} - T_{c,out})}{ln\left(\frac{(T_{h,in} - T_{c,in})}{(T_{h,out} - T_{c,out})}\right)} \tag{4.9}$$

and, for counter flow,

$$LMTD = \frac{(T_{h,in} - T_{c,out}) - (T_{h,out} - T_{c,in})}{ln\left(\frac{(T_{h,in} - T_{c,out})}{(T_{h,out} - T_{c,in})}\right)} \tag{4.10}$$

These equations can be readily solved for the rate of heat transfer Q and the exit temperatures of the participating fluids. As an alternative to the foregoing approach, the ε-NTU method can be used, where NTU = $[(R \times L)(\dot{m}c_p)_{min}]^{-1}$.

The approximations inherent in the use of the modular approach are: (a) constant thermophysical properties and (b) neglect of the velocity and thermal development lengths for the participating fluids. On the other hand, as a means of preliminary design, the simplicity of this approach is highly attractive.

*4.4.1.2 Overall heat transfer results*

The next focus of the presentation of the heat transfer results are comparisons between parallel flow and counter flow and between constant-property and variable- property models. These results are for the entire end-to-end heat exchanger (40 cm long in the flow direction) and not per module. For these comparisons, the pipe is of aluminum. Table 4.2 conveys these heat transfer results for both the *corrugated-pipe* heat exchanger and the

*smooth-walled* heat exchanger. The operating conditions listed in the title of the table are intended to be as close as possible to those of engineering practice.

Attention is first turned to the comparison of the counter flow and parallel flow results for the corrugated heat exchanger. It is noteworthy that a significant difference between the two operating modes (counter flow vs parallel flow) occurs for the variable property situation but the difference between the modes is moderate for the constant property case. In particular, for the variable property case, the counter flow heat transfer is 1.5 times that for parallel flow, while constant properties, that ratio is 1.1. The heat transfer difference between the two flow directions is far greater for the variable-property model reflecting the importance of the temperature dependence of the fluid viscosity.

Of particular relevance is the comparison between the heat transfer performance of the corrugated-walled and simple smooth-walled heat exchangers. It can be seen from Table 4.2 that the corrugations give rise to significant increases in the rate of heat transfer. Specifically, the ratio of the corrugated- and smoothed-walled heat transfer rates is on the order of a factor of three. In this regard, it is worthy of note that the heat transfer surface area for the pipe flow is increased by 98.3% due to the corrugations; the corresponding increase for the annulus flow is 77.7 %.

Table 4.2 Heat transfer for the full end-to-end heat exchanger with the twisted pipe of aluminum and a pitch of ½-turn per cm. Also shown are the heat transfer results for a smooth wall heat exchanger. Operating conditions at the inlets are: pipe Re = 2000, annulus Re = 420, $T_{c,in} = 4^oC$, and $T_{h,in} = 50^oC$.

| | Fluid properties | Heat transfer Q (W) for corrugated HX | Heat transfer Q (W) for smooth-surface HX |
|---|---|---|---|
| Counter flow | Variable | 809.8 | 252.2 |
| | Constant | 692.8 | 215.3 |
| Parallel flow | Variable | 528.8 | 197.7 |
| | Constant | 638.0 | 202.0 |

The heat transfer results presented in the foregoing were based on a Reynolds number of 420 for the flow in the annulus. Now, in Fig. 4.7, the annulus Reynolds number will be the independent variable over the range from 420 to 2000. The heat transfer rates displayed in the figure are an end-to-end result and correspond to the variable-property model. The other operating conditions for the figure are $T_{c,in}$ = 4°C, $T_{h,in}$ = 50°C, and a twisted pipe of aluminum with a ½-turn per cm pitch.

Inspection of the figure shows that when the pipe Reynolds number is 1000, the rate of heat transfer is more or less independent of the value of the annulus Reynolds number. It may also be inferred from the displayed results for the two pipe Reynolds numbers that for pipe Reynolds numbers less than 1000, the heat transfer does not depend on the annulus Reynolds number. Only for pipe Reynolds numbers between 1000 and 2000 does it appear that there is moderately sensitivity to the value of the annulus Reynolds number but only for values less than 1000.

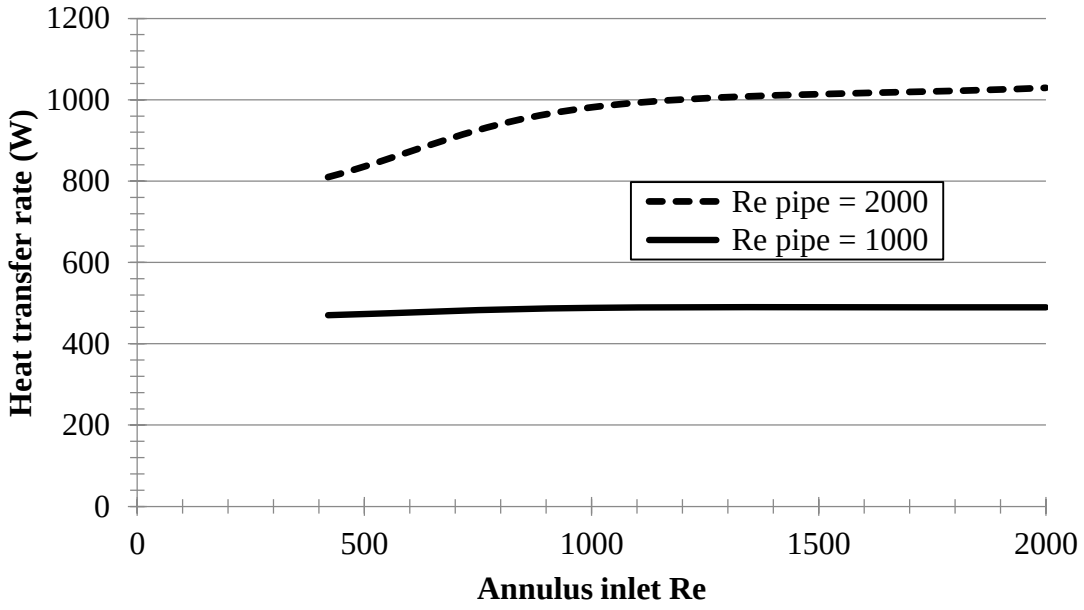


Fig. 4.7 Variable-property end-to-end heat transfer results as a function of $Re_{pipe}$ and $Re_{annulus}$ for $T_{c,in}$ = 4°C, $T_{h,in}$ = 50°C, and a twisted pipe of aluminum with a ½-turn per cm pitch

The next heat transfer emphasis is on the local heat flux, and graytone shading has been used to convey this information. To facilitate the presentation of results, the overall length of the heat exchanger was subdivided into four equal lengths (10 cm) designated consecutively as (a), (b), (c), and (d) from left to right. Fig. 4.8 conveys the local heat flux results for parallel flow, variable properties, $Re_{pipe}$ = 2000, $Re_{annulus}$ = 420, $T_{c,\,in}$ = 4°C, and $T_{h,\,in}$ = 50°C. The (hotter) pipe fluid and the (cooler) annulus fluid both enter at the left of Part (a). The color strip situated below the figure relates graytone shades to heat fluxes in W/m$^2$. Dark colors correspond to the highest values of heat flux.

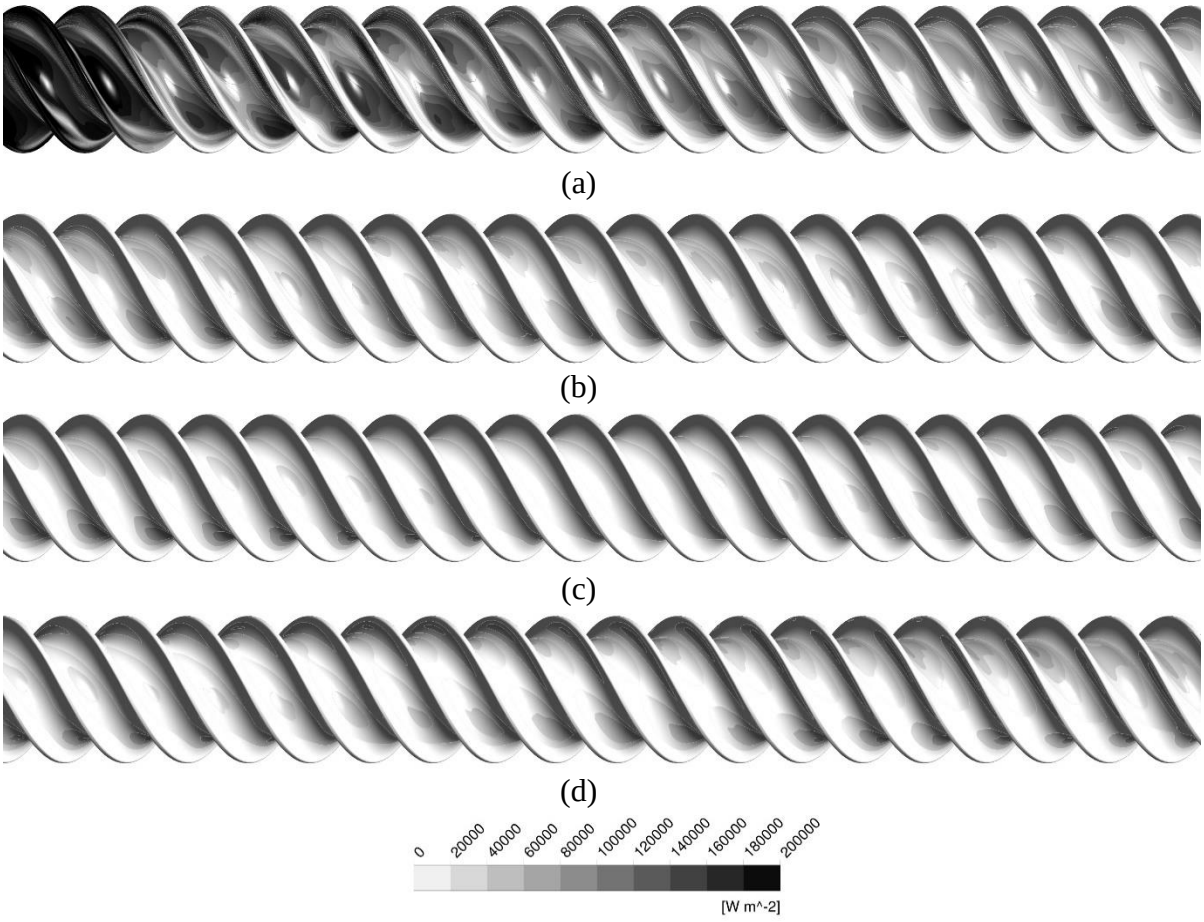


Fig. 4.8 Parallel-flow heat flux displayed by graytone contours for variable fluid properties, pipe *Re* = 2000, annulus *Re* = 420, $T_{c,in}$ = 4°C, and $T_{h,in}$ = 50°C. Both the pipe fluid (hotter fluid) and the annulus fluid (cooler fluid) enter at the left of Part (a) and exit at the right of Part (d). The pipe wall is made of aluminum.

It is expected that the highest penetration of each turn into the annulus flow experiences the highest rate of heat transfer for that turn and is, therefore, portrayed in a darker shade. In assessing the results of Fig. 4.8, it is appropriate to note that the annulus fluid is flowing over the successive turns from left to right so that the observed shading of each turn does support the aforementioned expectation. Inspection of the successive parts of the figure starting from (a) to (d) shows a monotonic change in color. At the inlets at the top left, the temperature difference between the two fluids is greatest, so that the highest rates of heat transfer are expected there. This expectation is verified by the deepest black color in that neighborhood. With increasing downstream distance from the inlet, a monotonic lightening is seen, indicating a reduction in the rate of heat transfer.

A second presentation of heat flux variations using the grayscale technique is shown in Fig. 4.9. This figure differs from the foregoing Fig. 4.8 in that it pertains to counter flow rather than to parallel flow. In the counter flow case, the pipe fluid (hotter fluid) enters at the right of Part (d) whereas the annulus fluid (cooler fluid) enters at the left of Part (a). In apprising the observed color patterns, it is relevant to note that the heat flux values depend both on the temperature differences between the participating fluids and on the respective heat transfer coefficients. It is well established that the magnitudes of the heat transfer coefficient are highest in regions of thermal development. For the case of Fig. 4.9, the thermal development regions occur in different parts of the pipe, in contrast to the parallel flow situation where the two thermal development regions are in the same neighborhood. In view of the different locations of the respective thermal development regions, it is not surprising that high rates of heat transfer are observed at the two extreme ends of the pipe. The highest rates of heat transfer are seen to occur in the thermal development region corresponding to the inlet of the hot pipe fluid (lower right).

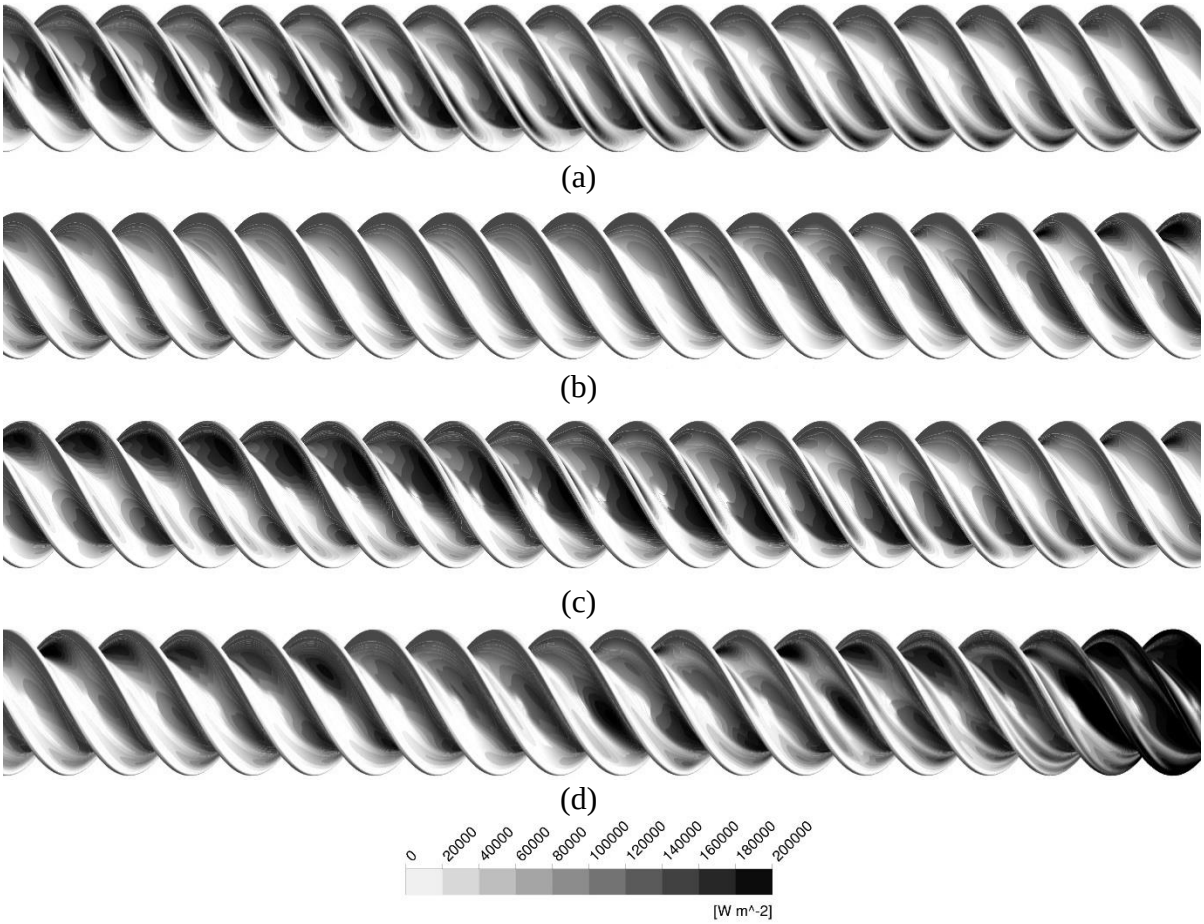


Fig. 4.9 Counter-flow heat flux displayed by graytone contours for variable fluid properties, pipe $Re$ = 2000, annulus $Re$ = 420, $T_{c,in}$ = 4°C, and $T_{h,in}$ = 50°C. Pipe fluid (hotter fluid) enters at the right of Part (d), and annulus fluid (cooler fluid) enters at the left of Part (a). The pipe wall is made of aluminum.

The next local thermal result is the temperature distribution on the external surface of the twisted tube. This information is conveyed in Figs. 4.10 and 4.11, respectively for the parallel flow and counter flow cases. In the parallel flow situation, both the hotter and cooler fluids enter at the left of Part (a) of Fig. 4.10. It can be seen from the figure that, in that neighborhood, the darkest color is manifested, indicating a temperature near 50°C. This outcome is worthy of some discussion, since the temperature of the annulus fluid in that neighborhood is 4°C. The fact that an approximate 50°C temperature is observed can be attributed to the fact that the heat transfer coefficient internal to the pipe is much greater

than the heat transfer coefficient external to the pipe. Further observation of the figure reveals a monotonic temperature decrease along the first segment of the pipe (part (a)) and a subsequent more or less constant temperature thereafter.

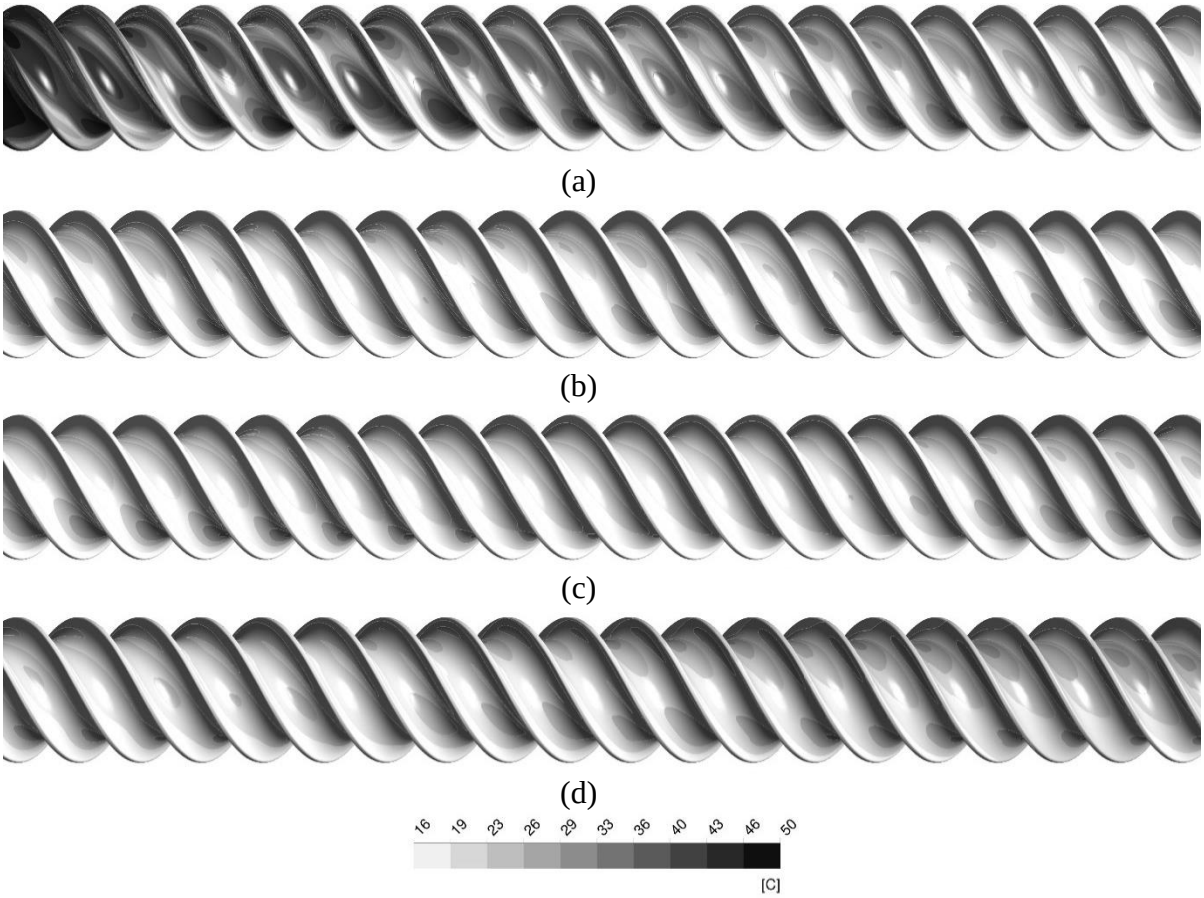


Fig. 4.10 Parallel-flow wall temperature distribution displayed by graytone contours for variable fluid properties, pipe *Re* = 2000, annulus *Re* = 420, $T_{c,in}$ = 4°C, and $T_{h,in}$ = 50°C. Both the pipe fluid (hotter fluid) and the annulus fluid (cooler fluid) enter at the left of Part (a). The pipe wall is made of aluminum.

The last figure in this set, Fig. 4.11, shows the temperature distribution along the aluminum twisted tube for the counter flow situation. The participating flows enter at opposite ends of the exchanger, with the cooler annulus fluid entering at the left of Part (a) in Fig. 4.11

and the hotter pipe fluid entering at the right of Part (d). In the counter flow case, the highest temperature of both fluids is expected to occur at the right-hand end of the exchanger and the lowest temperature to occur at the left-hand end. Examination of Fig. 4.11 validates this expectation.

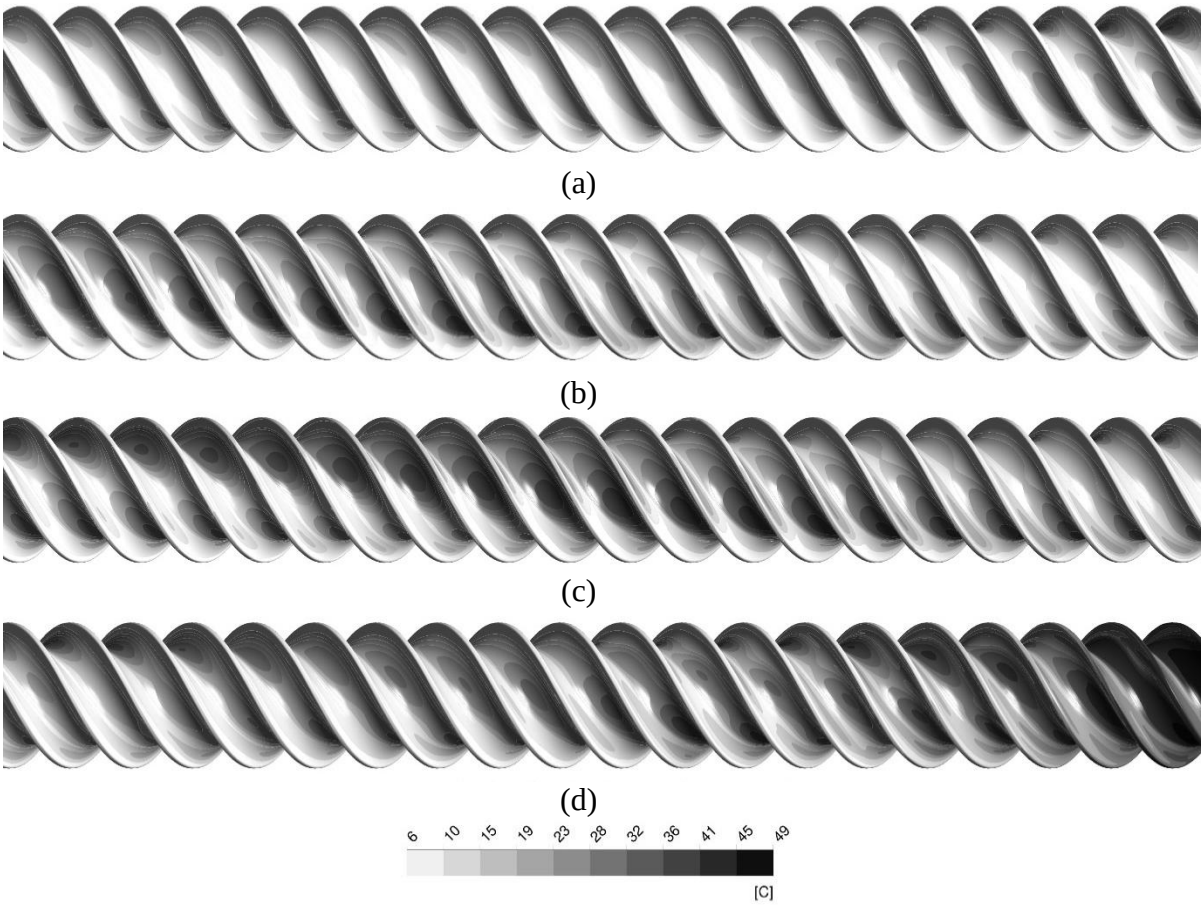


Fig. 4.11 Counter-flow wall temperature distribution displayed by graytone contours for variable fluid properties, pipe $Re$ = 2000, annulus $Re$ = 420, $T_{c,in}$ = 4°C, and $T_{h,in}$ = 50°C. The pipe fluid (hotter fluid) enters at the right of Part (d) and the annulus fluid (cooler fluid) enters at the left of Part (a). The pipe wall is made of aluminum.

### 4.4.2. Results and discussion for Fluid Flow

The results relating to fluid flow to be presented include pressure drops, patterns of fluid flow, and wall shear stress.

The pressure drop results will be conveyed both in tabular and graphical forms. Attention will first be focused on Table 4.3. This table summarizes, for both the corrugated- and smooth-walled heat exchangers, results for the end-to-end pressure drop for counter- and parallel-flow and for constant- and variable-property models. For perspective in the comparison of the effect of flow configuration (parallel versus counter), it is useful to recall that the annulus flow enters the system at the top left (Fig. 4.2) for both of the flow configurations, while the pipe flow enters at the top left for the parallel flow configuration and at the lower right for the cross flow configuration. For the constant-property case, the pressure drop for the annulus flow should be independent of the flow configuration as witnessed by the results of the table. On the other hand, for the pipe flow for constant properties, the reversal of the inlet location with the change in flow configuration requires a change in the pressure drop since the tilt of the helix differs depending on the direction of flow. However, the extent of the change is small as seen in the table. For flow in the annulus, the variable-property pressure drop is larger for the parallel flow case regardless of the flow configuration. The tabulated information will enlarged upon in succeeding figures. An overall generalization of the corrugated heat exchanger pressure drop results is that the variation among the pipe values is about 10% with a similar variation among the annulus values.

Table 4.3 Pressure drop for the full end-to-end heat exchanger with the twisted pipe of aluminum and a ½-turn per cm pitch. Also shown are the pressure drop results for a smooth wall heat exchanger. Operating conditions at the inlets are: pipe Re = 2000, annulus Re = 420, $T_{c,in}$ = 4°C, and $T_{h,in}$ = 50°C.

| | Fluid properties | Δp for corrugated HX (Pa) | | Δp for smooth-surface HX (Pa) | |
|---|---|---|---|---|---|
| | | Pipe | Annulus | Pipe | Annulus |
| Counter flow | Variable | 182.8 | 1025 | 74.4 | 288.7 |
| | Constant | 167.5 | 920.5 | 85.9 | 225.9 |
| Parallel flow | Variable | 143.2 | 1075 | 75.03 | 294.2 |
| | Constant | 162.5 | 920.5 | 85.9 | 225.9 |

Table 4.3 enables a comparison between the pressure drops for the corrugated- and smooth-walled heat exchanger. It can be seen from the table that the presence of the corrugations exacts a considerable pressure drop toll. In particular, for the pipe flow, the pressure drop for the corrugated-walled heat exchanger exceeds that for the smoothed-walled heat exchanger by approximately a factor of two. In contrast, for the annulus flow, the corrugated-walled heat exchanger pressure drop exceeds the smoothed-walled heat exchanger values by an approximate value of four. In this regard, it has been observed earlier that the use of the corrugated surface gave rise to a factor of three increase in the rate of heat transfer.

The graphical display pressure drop information begins with Figs. 4.12 and 4.13, which correspond to the constant-property and modular models. The first of these figures is for the pipe flow. The figure conveys the pressure drop per unit axial length. Parameters are the pipe Reynolds number ranging from 500 to 2000 on the abscissa and the turns per cm as the curve identification. Not unexpectedly, the pressure drop increases with increasing values of the Reynolds number and with a slope that also increases with Reynolds number. The latter trend may be attributed to the Reynolds numbers. The pressure drop also is seen to increase with the tighter helix.

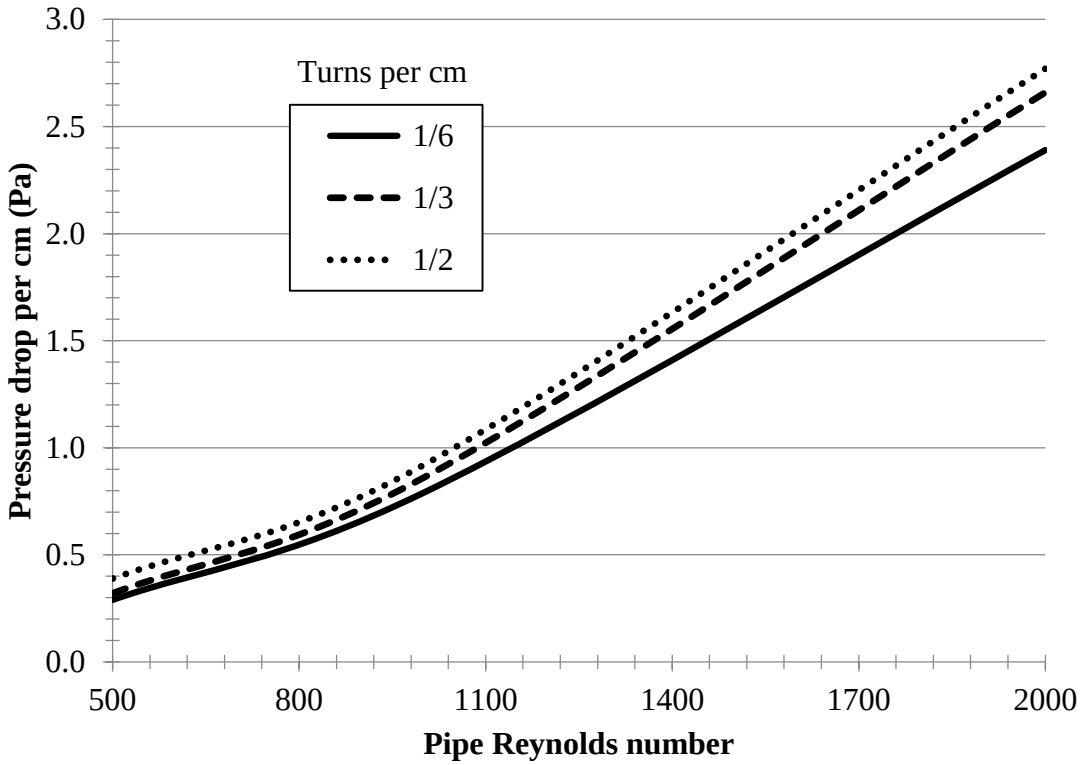


Fig. 4.12 Pressure drop in the pipe for constant-property flow. These results correspond to the modular model. The curves are parameterized by the number turns per cm of length.

Figure 4.13 is the counterpart of Fig. 4.12 but for the pressure drop in the annulus. The results shown in the figure correspond to $Re_{annulus}$ = 420. The helix-geometry parameter serves as the abscissa over the range from 0.15 to 0.5 turns per cm, corresponding to the least-tight helix to most-tight helix. As expected, the pressure drop increases with increasing helix tightness.

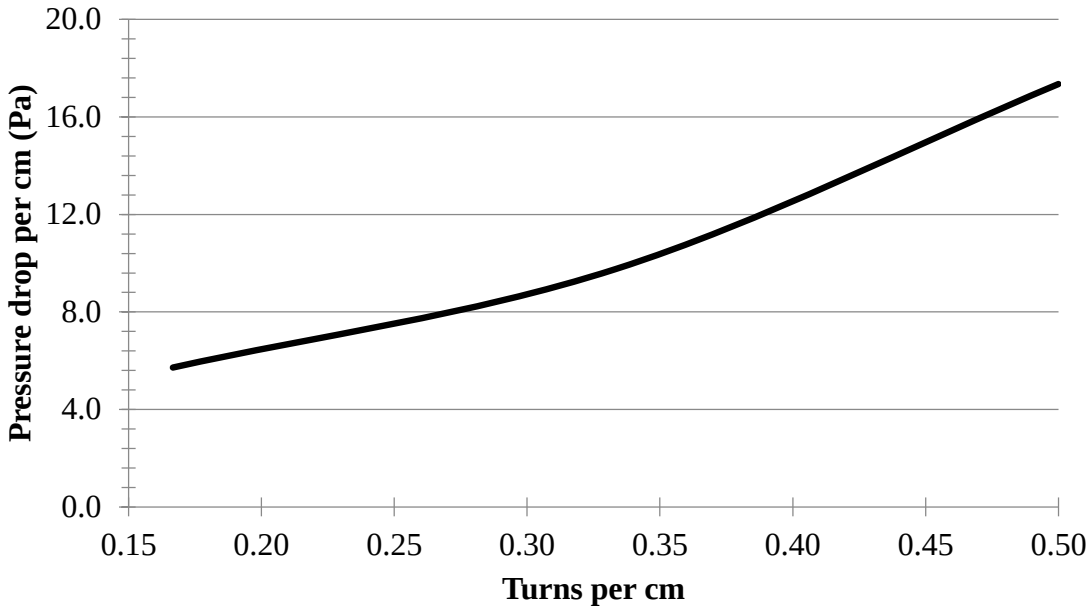


Fig. 4.13 Pressure drop in the annulus for constant-property flow for an annulus Reynolds number of 420. These results correspond to the modular model.

Attention will now be shifted from the constant-property focus of Figs. 4.12 and 4.13 to the variable-property focus of Figs. 4.14 and 4.15. The first of these figures is for end-to-end pressure drop in the pipe flow which is plotted as a function of $Re_{pipe}$ for parametric values of $Re_{annulus}$. The results correspond to a helix geometry of ½ turn per cm.

Of particular note in Fig. 4.14 is the absence of a significant effect of the annulus Reynolds number on the pipe-flow pressure drop. Any such effect should depend on the property variations in the pipe flow due to heat transfer between the annulus and pipe flows. The absence of dependence indicates that the heat transfer is not a major process. Another insight into the relevance of property variations is to compare the variable-property pipe flow pressure drop with its constant property counterpart. This comparison can be made for $Re_{pipe}$ = 2000, for which the pressure drops are 167.5 and 182.8 Pa, respectively for constant and variable properties, a difference of only 8.5%.

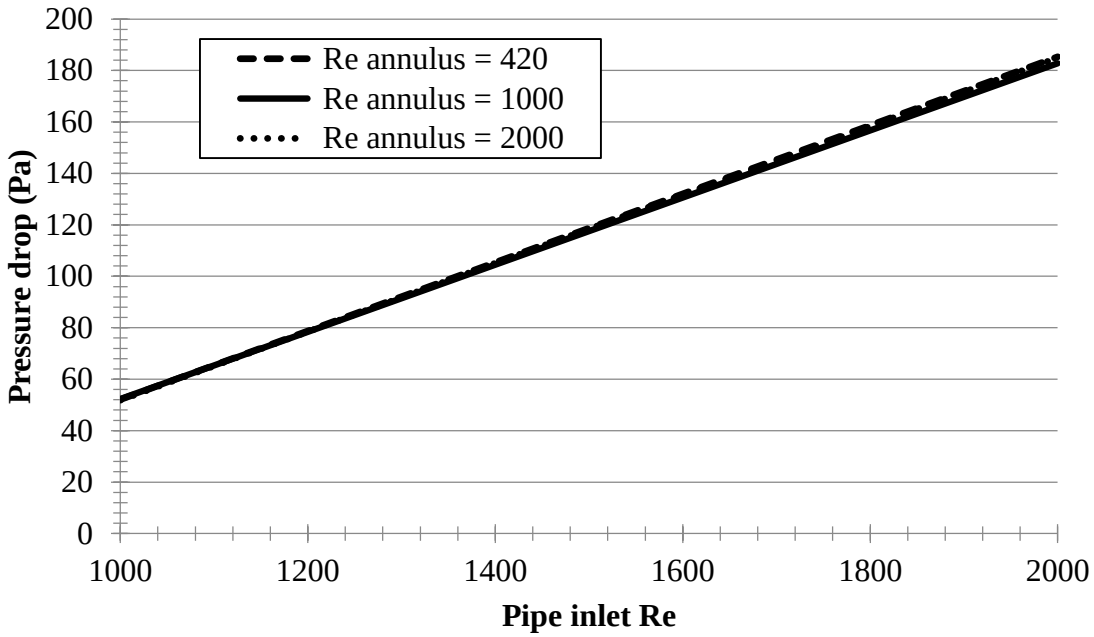


Fig. 4.14 Variable-property, end-to-end pipe pressure drop for the counter-flow configuration and for the helix geometry of ½ turn per cm.

Figure 4.15 is the annulus-flow counterpart of Fig. 4.14. The two figures display the common feature that the Reynolds number of the flow in the passages different from that for which the pressure drop is being displayed is irrelevant. It is also possible to compare the variable property impact as was done in the foregoing for the pipe-flow pressure drop. For $Re_{annulus}$ = 2000, the respective values of the constant-property and variable-property pressure drops are 920.5 and 1024.8 Pa, which is a difference of 10%.

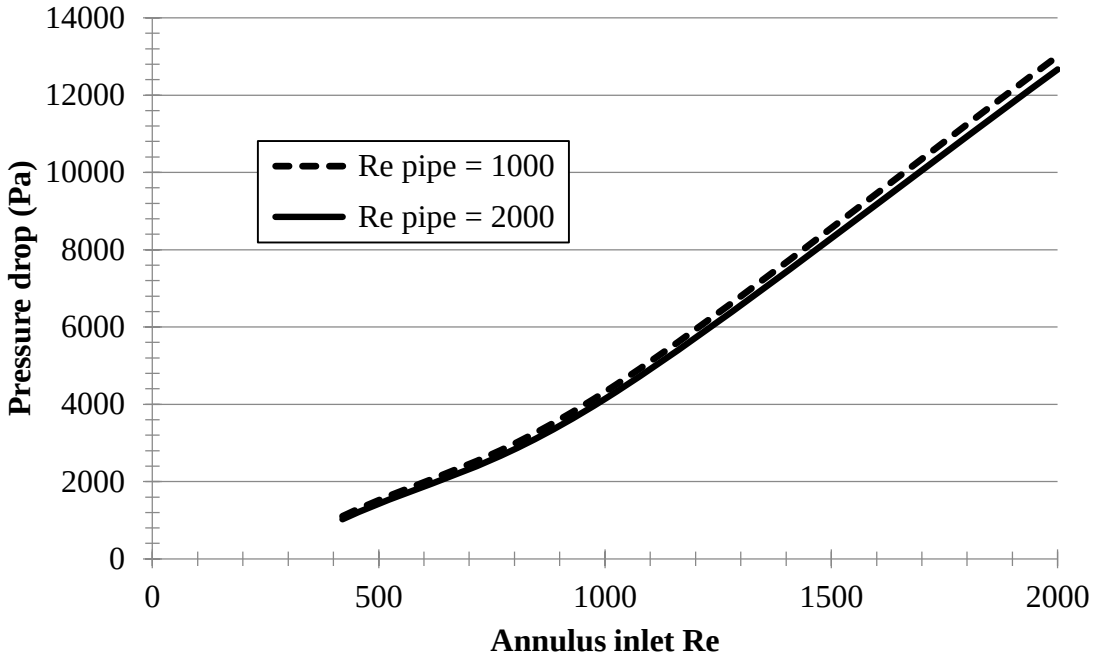


Fig. 4.15 Variable-property, end-to-end annulus pressure drop for the counter-flow configuration and for the helix geometry of ½ turn per cm.

Typical patterns of fluid flow will be conveyed by vector diagrams displayed in Fig. 4.16 (a) and (b), respectively for the counter-flow and parallel-flow situations. Each figure includes both of the participating fluids, and because fluid properties are constant for these results, the pipe flow and the annulus flow are independent of each other.

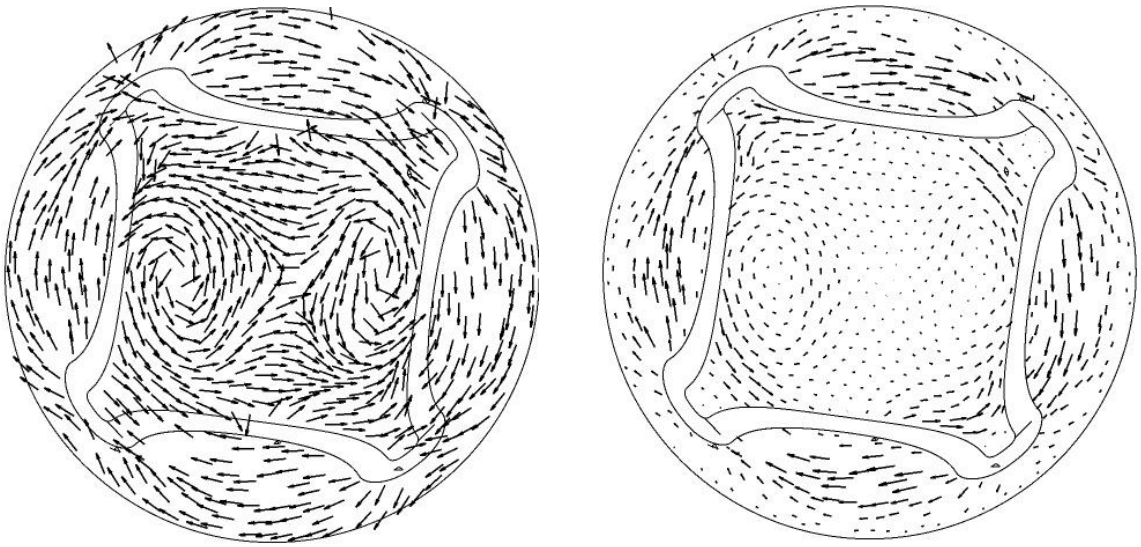


**(a) Counter flow**

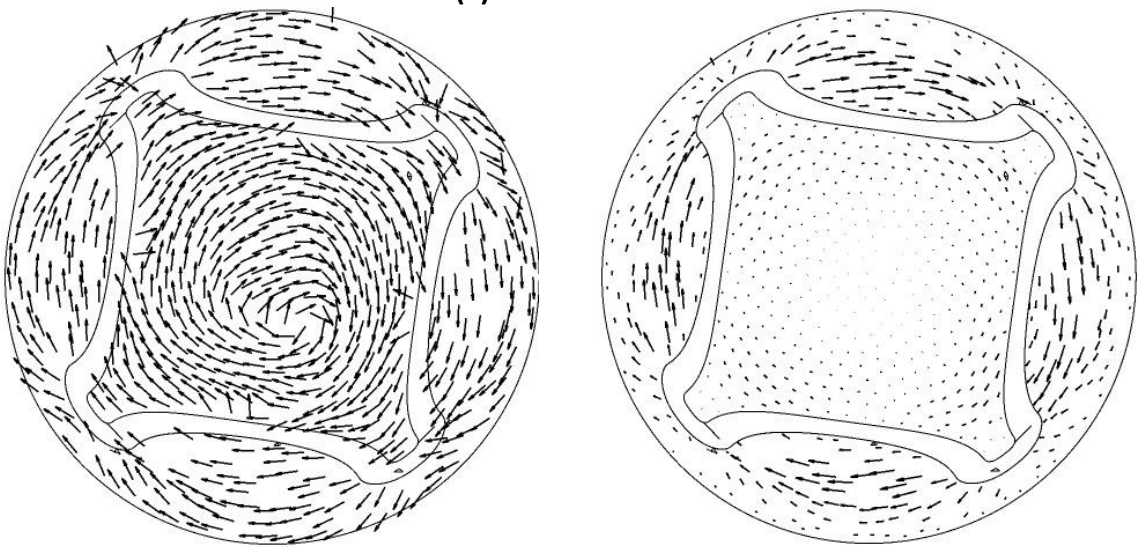


**(b) Parallel flow**

Fig. 4.16 Typical patterns of fluid flow conveyed by vector diagrams in cross-sectional planes that are experiencing fully developed flow. (a) counter flow, (b) parallel flow. Left-hand diagrams display normalized vectors showing flow directions, and right-hand diagrams present un-normalized vectors which show velocity magnitudes.

For the left-hand diagram in both the (a) and (b) parts of the figure, the annulus flow is seen to be rotating in the same clockwise direction due to the helical twist of the pipe

surface. In the pipe flows displayed in these figures, there is a general rotation, but with a different direction depending on whether the situation is either parallel flow or counter flow. For the counter-flow, pipe-flow case (Part (a)), the rotation is counter clockwise in which two counter clockwise rotating eddies are embedded. In contrast, for the parallel-flow, pipe-flow case (Part (b)), the rotation is clockwise without distinct eddies. These outcomes can be attributed to the fact that the annulus flow enters at the same location for both the parallel- and counter-flow configurations, whereas the pipe flow enters at different locations depending on the flow configuration. Additional simulations were performed to study the sensitivity of the fluid entering one side versus the other, and it was found that the heat transfer results differed by less than one percent.

Next, attention is directed to the right-hand diagrams of Parts (a) and (b). These diagrams provide definitive information about the velocity magnitude. It can be seen that the velocities in the pipe flow are generally quite small, while in the annulus flow, the largest velocities are confined to the widest parts of the flow space. The vector trends are similar for each pitch investigated.

The last result to be displayed is the wall shear stress in the annular space. This quantity would be of direct practical interest if the annulus fluid had been blood. Excessive shear is known to hemolysis (cell death in blood). Table 4 displays the separate values of the shear stress on the two bounding walls of the annular space for $Re_{annulus} = 420$ and helix pitches of 1/6, 1/3, and ½ turns per cm. The listed results were obtained for the constant-property and modular models. As expected, the shear on the smooth bounding wall of the annulus is substantially less than that on the helical wall. Also seen in the table is that the shear stress increases monotonically as the tightness of the helix increases. The values of the shear stress that are listed in the table are far too small to cause hemolysis [86].

Table 4.4 Wall shear stress on the bounding walls of the annular space for $Re_{annulus}$ = 420 based on the constant-property and modular models.

| **Annulus Re = 420** | **Wall shear (Pa)** | | |
|---|---|---|---|
| **Pitch (turns per cm)** | **1/6** | **1/3** | **1/2** |
| Twisted pipe inner wall | 0.56 | 0.75 | 1.52 |
| Smooth pipe outer wall | 0.40 | 0.54 | 0.79 |

## 4.5 CONCLUDING REMARKS

The simulation model was capable of high-fidelity descriptions of the complex geometries of both the pipe-flow passage and the annulus-flow passage. The design scope included both parallel and countercurrent flows, constant and variable fluid properties, overall end-to-end treatment of the heat exchanger as a single entity, and treatment of the exchanger as a succession of geometrically-identical modules. Other accounted-for independent variables included the number of helical turns per unit length and the Reynolds numbers of the pipe and annulus flows.

The heat transfer results included modular-based thermal resistances per unit length and overall heat transfer rates parameterized by flow configuration (counter or parallel flow), property constancy or variability, pitch of the helix, and the pipe and annulus Reynolds numbers. Local heat fluxes and temperature variations were conveyed by graytone-scaled portraits of the helical pipe wall. Although the counter flow configuration gave rise to higher rates of heat transfer (as expected), the degree of enhancement of counter flow over parallel flow depended strongly on the nature of the fluid property treatment. The extent of the enhancement was found to be much greater when variable fluid properties were accounted. For comparison, simple smooth-walled double-pipe heat exchanger results were presented as well.

Fluid flow results encompassed pressure drop in both the pipe and the annulus, patterns of fluid flow conveyed by vector diagrams, and wall shear stress. The pressure drop was seen to increase as the tightness of the helical winding increased. The expected lesser pressure

drop for parallel flow versus counter flow was validated for the pipe flow, but the annulus flow showed a reversal in the relationship. Vector-displayed flow patterns provided strong evidenced of the strong swirl imparted by the helical twist.

# Chapter Five

## CONCLUDING REMARKS

This thesis is focused on three biomedical therapeutic devices whose functions are clearly significant for promoting human health care. Medical device design and implementation is a mechanical engineering function which frequently span several sub-specialties. Based on the author's personal industrial experience, it is typical for companies to rely solely on past experience and a trial and error style of device design. That reliance on past experience can often lead to significant deviations from reality, and by not understanding the fundamental principles of a device, a company is significantly hamstrung in their efforts to develop optimized products. Moreover, the time needed to perform highly efficacious designs is rarely allocated, even though those techniques can often enable a company to innovate quicker and avoid potential issues over the full course of product development. This state-of-affairs has given rise to well-known and frequent recalls of commercial medical devices. Thirty-five individual medical devices were recalled in 2015. In particular, 100,000 Medtronic pacemakers model InSync IIIs were recalled in late September, 2015.

These realities clearly call for higher standards in the design of medical therapeutic devices. The attainment of such standards requires new and more fundamental approaches than are currently typical. Stricter accounting of the interacting fundamental disciplines is required along with the application of more powerful computational tools. Proper application of these foundational concepts has the potential to revolutionize the medical device industry, and the industry is still only beginning to see the benefits of this approach.

The goal of this thesis research is to set a new intellectual standard for the design of therapeutic medical devices. In this regard, three unique categories of devices were selected for study in order to expose a rich variety of interacting disciplines requiring very different

models for their successful solution. The three categories are respectively represented by: (a) long-term management of cystic fibrosis, (b) peristaltic pumping of drugs and other therapeutic fluids, and (c) heating and supply of blood and other fluids at suitable temperatures and flow rates for trauma relief. Category (a) involves fluid mechanics and the theory of sound, (b) is based on structural analysis of hyperelastic media and fluid mechanics, and (c) involves fluid mechanics, heat transfer, and thermodynamics. Different and specific approaches are required for these problems because they are so diverse. These differences add significantly to the generality and usefulness of the work described here.

In the first study, the fluid mechanics of a lung-clearance device were analyzed for optimal functional performance and sound generation. The key design tools used were computational fluid dynamics (CFD) and the theory of sound generated by turbulence. Results provided by the fluid mechanic study included the rates of air flow between the device and the inflatable vest, the rates of air supplied to and extracted from the entire device, the fluid velocity magnitudes and directions that result from the geometry of the device, and the magnitude of the turbulence generated by the fluid motion and the rotating component of the device. Both the velocity magnitudes and the strength of the turbulence contribute to the sound generation. A marked advantage of the numerical approach is that it enables cause and effect to be readily identified. Also, it enables changes and modifications in the geometry of the device to easily correct flaws in the original design.

The second study focused on the design of mechanically-based peristaltic pumps. The methodology set forth here is first principles implemented by numerical simulation. Provided that the computational resources are of sufficient capability, this methodology is able to avoid the oversimplifications that too often lead to erroneous results. Hyperelastic properties were deemed appropriate for the compressible tubular material that is commonly used for externally (out-of-body) situated peristaltic pumping. The theory of hyperelastic stress and strain was used to underpin the analysis.

Software based on this theory yielded stresses and mechanical deflections. In particular, the applied force need to sustain the prescribed rate of compression was determined. From the computed numerical information about the change of the volume of the bore of the tube, the rate of fluid flow provided by the peristaltic pumping action was calculated. Other results of practical utility include the spatial distributions of effective stress (von Mises) at a succession of times during the compression cycle. To complement the latter results, similar information was presented for the spatial and temporal evolution of the displacements. Overall, the outcome of the work provides a complete complement of information for the efficacious design of a mechanically-driven peristaltic pump.

The final study demonstrated that enhanced double pipe heat exchanger devices can be effectively designed by means of numerical simulation. The simulation model was capable of high-fidelity descriptions of the complex geometries of both the pipe-flow passage and the annulus-flow passage. The design scope included both parallel and countercurrent flows, constant and variable fluid properties, overall end-to-end treatment of the heat exchanger as a single entity, and treatment of the exchanger as a periodic succession of geometrically-identical modules. A simplified, smooth-walled double pipe heat exchanger was also simulated for comparison. Other accounted-for independent variables included the number of helical turns per unit length and the Reynolds numbers of the pipe and annulus flows. The heat transfer results included modular-based thermal resistances per unit length and overall heat transfer rates parameterized by flow configuration (counter or parallel flow), property constancy or variability, pitch of the helix, and the pipe and annulus Reynolds numbers. Local heat fluxes and temperature variations were conveyed by graytone-scaled portraits of the helical pipe wall.

Although the counter flow configuration gave rise to higher rates of heat transfer (as expected), the degree of enhancement of counter flow over parallel flow depended strongly on the nature of the fluid property treatment. The extent of the enhancement was found to be much greater when variable fluid properties were accounted. Fluid flow results included pressure drops in both the pipe and the annulus, patterns of fluid flow conveyed by vector

diagrams, and wall shear stress. The pressure drop was seen to increase as the tightness of the helical winding increased. The expected lesser pressure drop for parallel flow versus counter flow was validated for the pipe flow, but the annulus flow showed a reversal in the relationship. Vector-displayed flow patterns provided strong evidenced of the strong swirl imparted by the helical twist.

All three projects have several characteristic in common: the formulation of logic-tight physical models and subsequent implementation of the respective models by suitable numerical simulation tools. The simulation tools utilized in all three problems was ANSYS 15 and ANSYS 16.1, both the mechanical module as well as the CFX module.

During the period of execution of this thesis, experimental work was precluded because the normally available laboratories were totally unavailable due to the reconstruction of the building. Normally, it would be standard practice to validate the outcomes of numerical simulation by suitable experimentation. Since this practice was not possible in the present instance, extreme efforts were made to find alternative means of validation. Primary among these efforts was the use of the SST model which has been extensively verified in similar geometries.

# References


1. Sparrow, Eph, John Gorman, and John Abraham. "Quantitative assessment of the overall heat transfer coefficient U." Journal of heat transfer 135.6 (2013): 061102.
2. Bayazit, Yilmaz, Eph M. Sparrow, and Daniel D. Joseph. "Perforated plates for fluid management: Plate geometry effects and flow regimes." International Journal of Thermal Sciences 85 (2014): 104-111.
3. Li, A., X. Chen, and L. Chen. "Numerical investigations on effects of seven drag reduction components in elbow and T-junction close-coupled pipes." Building Services Engineering Research and Technology (2014): 0143624414541453.
4. Engdar, Ulf, and Jens Klingmann. "Investigation of two-equation turbulence models applied to a confined axis-symmetric swirling flow." ASME 2002 Pressure Vessels and Piping Conference. American Society of Mechanical Engineers, 2002.
5. Clausen, P. D., S. G. Koh, and D. H. Wood. "Measurements of a swirling turbulent boundary layer developing in a conical diffuser." Experimental Thermal and Fluid Science 6.1 (1993): 39-48.
6. Chatburn, Robert L. "High-frequency assisted airway clearance." Respiratory care 52.9 (2007): 1224-1237.
7. Button, Brenda M., and Brian Button. "Structure and function of the mucus clearance system of the lung." Cold Spring Harbor perspectives in medicine 3.8 (2013): a009720.
8. Diong, Bill, et al. "Modeling human respiratory impedance." Engineering in Medicine and Biology Magazine, IEEE 26.1 (2007): 48-55.
9. Dosman, Cara F., and Richard L. Jones. "High-frequency chest compression: a summary of the literature." Canadian respiratory journal: journal of the Canadian Thoracic Society 12.1 (2004): 37-41.
10. Elad, D., A. Shochat, and R. J. Shiner. "Computational model of oscillatory airflow in a bronchial bifurcation." Respiration physiology 112.1 (1998): 95-111.
11. Fink, James B., and Michael J. Mahlmeister. "High-frequency oscillation of the airway and chest wall." Respiratory care 47.7 (2002): 797-807.

12. Hansen, L. G., and W. J. Warwick. "High-frequency chest compression system to aid in clearance of mucus from the lung." Biomedical instrumentation & technology/Association for the Advancement of Medical Instrumentation 24.4 (1989): 289-294.
13. Kendrick, A. "Airway clearance techniques in cystic fibrosis. Physiology, devices and the future." Journal of the Royal Society of Medicine-Supplements Only 47 (2007): 3-23.
14. Khirani, S., et al. "Positive end expiratory pressure and expiratory flow limitation: a model study." Acta biotheoretica 49.4 (2001): 277-290.
15. Lambert, RODNEY K., et al. "A computational model for expiratory flow." Journal of Applied Physiology 52.1 (1982): 44-56.
16. Lee, Jongwon, Yong Wan Lee, and Warren J. Warwick. "High frequency chest compression effects heart rate variability." Engineering in Medicine and Biology Society, 2007. EMBS 2007. 29th Annual International Conference of the IEEE. IEEE, 2007.
17. Main, Eleanor, Lizzie Grillo, and Sarah Rand. "Airway clearance strategies in cystic fibrosis and non-cystic fibrosis bronchiectasis." Seminars in respiratory and critical care medicine. Vol. 36. No. 2. 2015.
18. McCarren, Bredge, Jennifer A. Alison, and Robert D. Herbert. "Vibration and its effect on the respiratory system." Australian Journal of Physiotherapy 52.1 (2006): 39-43.
19. Morrison, Lisa, and Jennifer Agnew. "Oscillating devices for airway clearance in people with cystic fibrosis." Cochrane Database Syst Rev 7 (2014).
20. Myers, Timothy R. "Positive expiratory pressure and oscillatory positive expiratory pressure therapies." Respiratory care 52.10 (2007): 1308-1327.
21. O'Clock, George D., et al. "A simulation tool to study high-frequency chest compression energy transfer mechanisms and waveforms for pulmonary disease applications." Biomedical Engineering, IEEE Transactions on 57.7 (2010): 1539-1546.

22. Phillips, Gillian E., et al. "Comparison of active cycle of breathing and high-frequency oscillation jacket in children with cystic fibrosis." Pediatric pulmonology 37.1 (2004): 71-75.
23. Sohn, Kiwon, et al. "Modeled velocity of airflow in the airways during various respiratory patterns." Engineering in Medicine and Biology Society, 2004. IEMBS'04. 26th Annual International Conference of the IEEE. Vol. 2. IEEE, 2004.
24. Sohn, Kiwon, et al. "Investigation of non-uniform airflow signal oscillation during high frequency chest compression." Biomedical engineering online 4.1 (2005): 34.
25. Volsko, Teresa A., Juliann M. DiFiore, and Robert L. Chatburn. "Performance comparison of two oscillating positive expiratory pressure devices: Acapella versus Flutter." Respiratory care 48.2 (2003): 124-130.
26. Menter, Florian R. "Two-equation eddy-viscosity turbulence models for engineering applications." AIAA journal 32.8 (1994): 1598-1605.
27. Proudman, I. "The generation of noise by isotropic turbulence." Proceedings of the Royal Society of London A: Mathematical, Physical and Engineering Sciences. Vol. 214. No. 1116. The Royal Society, 1952.
28. Latham, Thomas Walker. Fluid motions in a peristaltic pump. Diss. Massachusetts Institute of Technology, 1966.
29. Neto, A. G. S. B., et al. "Linear peristaltic pump driven by three magnetic actuators: Simulation and experimental results." Instrumentation and Measurement Technology Conference (I2MTC), 2011 IEEE. IEEE, 2011.
30. Coe, G. H. "Peristaltic pump." World Pumps (1987): 106-9.
31. Jaffrin, M. Y., and A. H. Shapiro. "Peristaltic pumping." Annual Review of Fluid Mechanics 3.1 (1971): 13-37.
32. Sreenadh, S., and P. Devaki. "Mathematical Model for the Peristaltic Pumping of a Viscous Fluid in an Elastic Tube." Atti Della Fondazione Giorgio Ronchi Anno LXVII N. 2: 163.
33. Wang, Yongqi, Tasawar Hayat, and Kolumban Hutter. "Peristaltic flow of a Johnson-Segalman fluid through a deformable tube." Theoretical and Computational Fluid Dynamics 21.5 (2007): 369-380.

34. Muthu, P., B. V. Rathish Kumar, and Peeyush Chandra. "On the influence of wall properties in the peristaltic motion of micropolar fluid." The ANZIAM Journal 45.02 (2003): 245-260.
35. Mittra, Tridib K., and Shyam N. Prasad. "On the influence of wall properties and Poiseuille flow in peristalsis." Journal of biomechanics 6.6 (1973): 681-693.
36. Khan, Ambreen Afsar, R. Ellahi, and Muhammad Usman. "The effects of variable viscosity on the peristaltic flow of non-Newtonian fluid through a porous medium in an inclined channel with slip boundary conditions." Journal of Porous Media 16.1 (2013).
37. Reddy, MV Subba, A. Ramachandra Rao, and S. Sreenadh. "Peristaltic motion of a power-law fluid in an asymmetric channel." International Journal of Non-Linear Mechanics 42.10 (2007): 1153-1161.
38. Jeffrey, Brian, Holavanahalli S. Udaykumar, and Konrad S. Schulze. "Flow fields generated by peristaltic reflex in isolated guinea pig ileum: impact of contraction depth and shoulders." American Journal of Physiology-Gastrointestinal and Liver Physiology 285.5 (2003): G907-G918.
39. Shapiro, Ascher H., Michel Y. Jaffrin, and Steven L. Weinberg. "Peristaltic pumping with long wavelengths at low Reynolds number." Journal of Fluid Mechanics 37.04 (1969): 799-825.
40. El-Shehawy, E. F., N. T. El-Dabe, and I. M. El-Desoky. "Slip effects on the peristaltic flow of a non-Newtonian Maxwellian fluid." Acta Mechanica 186.1-4 (2006): 141-159.
41. Gao, Feng, et al. "Fluid-structure interaction within a layered aortic arch model." Journal of biological physics 32.5 (2006): 435-454.
42. Jyothi, N. Naga, P. Devaki, and S. Sreenadh. "EFFECT OF POROUS LINING ON THE PERISTALTIC TRANSPORT OF A CASSON FLUID IN AN INCLINED CHANNEL." International Journal of Mathematical Archive (IJMA) ISSN 2229-5046 4.4 (2013).
43. Maeda, Shingo, et al. "Peristaltic gel pump driven by chemical energy. "Robotics and Biomimetics (ROBIO), 2011 IEEE International Conference on. IEEE, 2011.

44. Orchard, Bryan. "Laboratories and industry provide opportunities for peristaltic pumps." World Pumps 2004.448 (2004): 24-26.
45. Dash, AlekhaK, and GreggreyC Cudworth. "Therapeutic applications of implantable drug delivery systems." Journal of pharmacological and toxicological methods 40.1 (1998): 1-12.
46. Albisser, A. M., et al. "A portable precision pumping system for chronic, programmed insulin infusion." Medical progress through technology 5.4 (1978): 187-193.
47. Greer, Frank R., Ann McCormick, and Jeffrey Loker. "Changes in fat concentration of human milk during delivery by intermittent bolus and continuous mechanical pump infusion." The Journal of pediatrics 105.5 (1984): 745-749.
48. Singh, Parminder, and Howard I. Maibach. "Iontophoresis: an alternative to the use of carriers in cutaneous drug delivery." Advanced drug delivery reviews 18.3 (1996): 379-394.
49. Streubel, Alexander, Juergen Siepmann, and Roland Bodmeier. "Drug delivery to the upper small intestine window using gastroretentive technologies." Current opinion in pharmacology 6.5 (2006): 501-508.
50. Sastry, Srikonda Venkateswara, Janaki Ram Nyshadham, and Joseph A. Fix. "Recent technological advances in oral drug delivery–a review." Pharmaceutical science & technology today 3.4 (2000): 138-145.
51. Nguyen, Nam-Trung, and Xiaoyang Huang. "Development of a peristaltic pump in printed circuit boards." Journal of Micromechatronics 3.1 (2005): 1-13.
52. Husband, B., et al. "Novel actuation of an integrated peristaltic micropump." Microelectronic Engineering 73 (2004): 858-863.
53. Tatsumi, Kazuya, et al. "Numerical study on fluid-flow characteristics of peristaltic pump." Progress in Computational Fluid Dynamics, an International Journal 9.3-5 (2009): 176-182.
54. Wu, Yanzhe, et al. "TITAN: a conducting polymer based microfluidic pump." Smart materials and structures 14.6 (2005): 1511.
55. Lotz, Peter, Marc Matysek, and Helmut F. Schlaak. "Peristaltic pump made of dielectric elastomer actuators." SPIE Smart Structures and Materials+ Nondestructive

Evaluation and Health Monitoring. International Society for Optics and Photonics, 2009.

56. Oh, J. H., et al. "A Valveless Piezoelectric Micro-Pump Using Peristaltic Motion of Two Sided Disk Type Vibrator." Ferroelectrics 409.1 (2010): 128-138.
57. Voskerician, Gabriela, et al. "Biocompatibility and biofouling of MEMS drug delivery devices." Biomaterials 24.11 (2003): 1959-1967.
58. Tao, Sarah L., and Tejal A. Desai. "Microfabricated drug delivery systems: from particles to pores." Advanced drug delivery reviews 55.3 (2003): 315-328.
59. Hilt, J. Zachary, and Nicholas A. Peppas. "Microfabricated drug delivery devices." International Journal of Pharmaceutics 306.1 (2005): 15-23.
60. de Souza Neto, Eduardo A., Djordje Peric, and David Roger Jones Owen. Computational methods for plasticity: theory and applications. John Wiley & Sons, 2011.
61. ANSYS Element Reference (2009), Section 2.5.2.4
62. Alkam, M. K., and M. A. Al-Nimr. "Improving the performance of double-pipe heat exchangers by using porous substrates." International Journal of Heat and Mass Transfer 42.19 (1999): 3609-3618.
63. Targui, N., and H. Kahalerras. "Analysis of fluid flow and heat transfer in a double pipe heat exchanger with porous structures." Energy Conversion and Management 49.11 (2008): 3217-3229.
64. Kahalerras, H., and N. Targui. "Numerical analysis of heat transfer enhancement in a double pipe heat exchanger with porous fins." International Journal of Numerical Methods for Heat & Fluid Flow 18.5 (2008): 593-617.
65. Targui, N., and H. Kahalerras. "Analysis of a double pipe heat exchanger performance by use of porous baffles and pulsating flow." Energy Conversion and Management 76 (2013): 43-54.
66. Du, Y. P., et al. "Numerical study of conjugated heat transfer in metal foam filled double-pipe." International journal of heat and mass transfer 53.21 (2010): 4899-4907.

67. Akpinar, Ebru Kavak. "Evaluation of heat transfer and exergy loss in a concentric double pipe exchanger equipped with helical wires." Energy Conversion and Management 47.18 (2006): 3473-3486.
68. Zohir, A. E., M. A. Habib, and M. A. Nemitallah. "Heat transfer characteristics in a double-pipe heat exchanger equipped with coiled circular wires." Experimental heat transfer 28.6 (2015): 531-545.
69. Sheikholeslami, Mohsen, et al. "Investigation of turbulent flow and heat transfer in an air to water double-pipe heat exchanger." Neural Computing and Applications 26.4 (2015): 941-947..
70. Zohir, A. E., Ali A. Abdel Aziz, and M. A. Habib. "Heat transfer characteristics and pressure drop of the concentric tube equipped with coiled wires for pulsating turbulent flow." Experimental Thermal and Fluid Science 65 (2015): 41-51.
71. Eiamsa-ard, Smith, Chinaruk Thianpong, and Pongjet Promvonge. "Experimental investigation of heat transfer and flow friction in a circular tube fitted with regularly spaced twisted tape elements." International Communications in Heat and Mass Transfer 33.10 (2006): 1225-1233.
72. Jayakumar, J. S., et al. "Experimental and CFD estimation of heat transfer in helically coiled heat exchangers." chemical engineering research and design 86.3 (2008): 221-232.
73. Syed, K. S., Mazhar Iqbal, and N. A. Mir. "Convective heat transfer in the thermal entrance region of finned double-pipe." Heat and mass transfer 43.5 (2007): 449-457.
74. Syed, Khalid S., Muhammad Ishaq, and Muhammad Bakhsh. "Laminar convection in the annulus of a double-pipe with triangular fins." Computers & Fluids 44.1 (2011): 43-55.
75. Mohammed, H. A., Husam A. Hasan, and M. A. Wahid. "Heat transfer enhancement of nanofluids in a double pipe heat exchanger with louvered strip inserts." International Communications in Heat and Mass Transfer 40 (2013): 36-46.

76. Sheikholeslami, M., M. Gorji-Bandpy, and D. D. Ganji. "Experimental study of the influence of perforated circular-ring on pressure loss and heat transfer enhancement using sensitivity analysis." Applied Thermal Engineering 91 (2015): 739-748.
77. Bhadouriya, Rambir, Amit Agrawal, and S. V. Prabhu. "Experimental and numerical study of fluid flow and heat transfer in an annulus of inner twisted square duct and outer circular pipe." International Journal of Thermal Sciences 94 (2015): 96-109.
78. Agrawal, Ajay K., and Subrata Sengupta. "Laminar fluid flow and heat transfer in an annulus with an externally enhanced inner tube." International journal of heat and fluid flow 14.1 (1993): 54-63.
79. Pethkool, S., et al. "Turbulent heat transfer enhancement in a heat exchanger using helically corrugated tube." International Communications in Heat and Mass Transfer 38.3 (2011): 340-347.
80. Dizaji, Hamed Sadighi, Samad Jafarmadar, and Farokh Mobadersani. "Experimental studies on heat transfer and pressure drop characteristics for new arrangements of corrugated tubes in a double pipe heat exchanger." International Journal of Thermal Sciences 96 (2015): 211-220.
81. Uzzan, M., K. M. Leinen, and T. P. Labuza. "Temperature Profiles within a Double-pipe Heat Exchanger with Countercurrent Turbulent Flow of Newtonian Fluids: Derivation, Validation, and Application to Food Processing." Journal of food science 69.9 (2004): E433-E440.
82. Rennie, Timothy J., and Vijaya GS Raghavan. "Numerical analysis of the lethality and processing uniformity in a double-pipe helical heat exchanger." Chemical Engineering and Processing: Process Intensification 49.7 (2010): 672-679.
83. Agarwal, P. A. D. M. A. K. S. H. I., and Shanthi V. Adhirathsik. "Application of heat exchangers in bioprocess industry: a review." International Journal of Pharmacy and Pharmaceutical Sciences 6.1 (2014): 24-28.
84. Wagner, Wolfgang, and Hans-Joachim Kretzschmar. International Steam Tables-Properties of Water and Steam based on the Industrial Formulation IAPWS-IF97 Springer Science & Business Media, 2007.

85. Sparrow, Ephraim M., Jimmy CK Tong, and John P. Abraham. "Fluid flow in a system with separate laminar and turbulent zones." Numerical Heat Transfer, Part A: Applications 53.4 (2008): 341-353.
86. Grigioni, M., et al. "A discussion on the threshold limit for hemolysis related to Reynolds shear stress." Journal of biomechanics 32.10 (1999): 1107-1112.